Dust Dynamics in Protoplanetary Disks: Fables of the Sun and the Wind in the Pre- and Post-Planet-Formation Eras

by

Jiaqing Bi
M.Sc., University of Victoria, Canada, 2020
B.Sc., Xi'an Jiaotong University, China, 2018

A Dissertation Submitted in Partial Fulfillment of the
Requirements for the Degree of

DOCTOR OF PHILOSOPHY

in the Department of Physics and Astronomy

Dust Dynamics in Protoplanetary Disks: Fables of the Sun and the Wind in the Pre- and Post-Planet-Formation Eras

by

Jiaqing Bi
M.Sc., University of Victoria, Canada, 2020
B.Sc., Xi’an Jiaotong University, China, 2018

Supervisory Committee

Dr. Ruobing Dong, Supervisor
(Department of Physics and Astronomy)

Dr. Brenda C. Matthews, Departmental Member
(Department of Physics and Astronomy)

Dr. Jeffrey Fung, Outside Member
(Department of Physics and Astronomy, Clemson University)

ABSTRACT

Dust grains in protoplanetary disks are the most fundamental building blocks of planetary embryos. Therefore, they play a crucial role in the planet formation process. In this dissertation, we focus on the topic of dust dynamics, aiming at exploring the origin of the observed dust substructures in protoplanetary disks and the correlation between the substructures and planets. Dust dynamics in two main periods of time are studied in this dissertation: before and after the formation of the planet. In the first part, we focus on the micron-sized dust grains that are susceptible to the radiation pressure from the star. We present a newly found irradiation instability that leads to the clumping effects of dust grains. We also found that the dust clumps make the disk more transparent, promoting disk edge recession due to radiation pressure, and shedding light on the formation of large dust cavities in transitional disks. In the second part, we focus on the sub-mm-sized dust grains trapped at the planet-induced pressure bump. We show that planet-disk interactions tend to widen dust rings. We also model the planet's effect on the dust via diffusion and quantify the enhanced dust ring width with analytical tools. Our findings bridge the correlations between the confirmed planets and the accompanying wide dust rings.

Contents

List of Tables

List of Figures

Acknowledgements

Foremost, I would like to express my sincere gratitude to my advisor Ruobing Dong, for the continuous support of my research and career development. It is unfortunate that a large fraction of my doctoral program was during a hard time of the COVID-19 pandemic when people could not meet as they wanted. Meanwhile, I am fortunate to have Ruobing, who is always responsive whenever there is a need.

Besides, I am greatly indebted to Jeffrey Fung, who introduced me to this field and provided insightful advice at every single stage of my career. I am also grateful to Min-Kai Lin, who greatly inspired my enthusiasm for the research topics that I have been working on. I would also like to thank Akimasa Kataoka, Brenda Matthews, and Nienke van der Marel for their help.

My research was primarily supported by the Natural Sciences and Engineering Research Council of Canada. I would like to thank Xi'an Jiaotong University and the Academia Sinica Institute of Astronomy and Astrophysics for funding and career development opportunities. Meanwhile, I am grateful to the Boehm family, the Hesser family, the Lipson family, the de Goutiere family, and Albert Hung Chao Hong for their generous donations.

In the end, I would like to thank my family, who have unconditionally supported me throughout my life.

Chapter 1

Introduction

Protoplanetary disks are disk-shaped structures surrounding newly formed stars. They are the outcomes of the gravitational collapse of the molecular clouds that give birth to young stars, and end up in disk-shape due to the conservation of angular momentum (see Pineda et al. 2022 for a review). The disks are composed of gas and dust, with the state-of-the-art planet formation theory suggesting that they are the birthplaces of planets. Spurred by the first detection of an exoplanet (51 Peg b; Mayor and Queloz 1995) and facilitated by the development of theoretical, numerical, and observational methods, planet formation in protoplanetary disks has become one of the hottest topics in the field of astronomy.

Dust, though a minor part of the gas-rich protoplanetary disk, plays a critical role in planet formation because it is the fundamental building block of planets. Nowadays, rich information about micron-to-millimeter-sized dust grains has been provided by disk observations in infrared wavelengths (e.g., Andrews et al. 2018, also see Benisty et al. 2022 for a review). One of the most important findings is the existence of non-trivial dust distributions in the disk (e.g., dust gaps and rings in the HL Tau disk; ALMA Partnership et al. 2015). However, the correlation between those dust substructures and the planet formation process is still a piece of missing puzzle in the story.

For example, there is a “chicken and egg” problem for the planets and the gap-ring systems. On the one hand, because of their high concentration of dust, dust rings are believed to be the ideal locations for small dust grains to grow into larger ones via collisional growth (e.g., Birnstiel et al. 2012), streaming instability (e.g., Youdin and Goodman 2005, Johansen and Youdin 2007, Youdin and Johansen 2007, Jacquet et al. 2011), pebble accretion (e.g., Jiang and Ormel 2022, also Drążkowska et al. 2022 for a review), and so on, which are promising early steps of planet formation. On the other hand, the formation of the gap-ring system is often attributed to the presence of massive, gap-opening planets (e.g., Kanagawa et al. 2016, Zhang et al. 2018, also Paardekooper et al. 2022 for a review), under which circumstance planet formation itself becomes a prerequisite. Inspired by this conundrum, in this dissertation, we perform investigations on dust dynamics in the disk, which is critical to the formation of both planets and dust substructures, before and after the formation of planets. We aim at answering the questions of how to form a dust substructure without a planet and how to tell whether a dust substructure is formed by a planet, which helps to tackle this “chicken and egg” problem.

In Chapter 2, we first focus on dust dynamics in the so-called transitional disk before the formation of planets. Transitional disks are characterized by the depletion of dust in their central regions (see van der Marel 2022 for a review). However, the origin of those inner cavities is still uncertain. Recent surveys on transitional disks by the Atacama Large Millimeter/Submillimeter Array (ALMA) and Australia Telescope Compact Array (ATCA) suggest that the cavities are cleared by planets in the disk (e.g., van der Marel et al. 2018; Francis and van der Marel 2020; Norfolk et al. 2021). However, evidence shows that planets may not be the only explanation for these cavities:

1. There are only three planet-hosting transitional disks confirmed so far (PDS 70, Keppler et al. 2018; Haffert et al. 2019; AB Aur, Currie et al. 2022; and HD 169142, Hammond et al. 2023), even though the dust-depleted, optically thin cavities should provide a good chance to detect planets via high-contrast direct imaging.

2. A complete disk survey in the Lupus star-forming region shows that the fraction of disks with a large cavity ($\geq$20 au) is $\gtrsim$11% (van der Marel et al. 2018). This fraction is noticeably higher than the fraction of giant planets on such high orbits around main-sequence stars (<8% for all stars, <6.8% for FGK stars, and <4.2% for M stars; Bowler 2016).

3. The transitional disk fraction for Herbig Ae/Be stars ($\sim$28%; Guzmán-Díaz et al. 2021) is typically higher than that for T Tauri stars ($\lesssim$10%; Muzerolle et al. 2010; Furlan et al. 2011).

Therefore, we want to seek other possible mechanisms to clear the cavity in transitional disks. Since the cavities appear to be correlated with the spectral type of the central star, mechanisms related to the stellar luminosity such as photoevaporation and radiation pressure may be responsible for cavity clearing. However, the Herbig Ae/Be star survey cited above (Guzmán-Díaz et al. 2021) reveals that some transitional disks have an age less than 0.1 Myr. This is shorter than the estimated timescale for photoevaporation to open the gap ($\gtrsim$1 Myr; Gárate et al. 2021). Instead, we revisit an alternative explanation: dust migration due to radiation pressure.

Radiation pressure is a force of light on the illuminated object via exchanging momentum between the object and the electromagnetic field. In protoplanetary disks, radiation pressure from the central star pushes dust grains outward, but whether it can prevent dust from accreting onto the star is still under debate. Takeuchi and Artymowicz (2001) studied the dynamics of irradiated dust grains in an optically thin, non-accretion disk. They pointed out that the angular momentum of dust grains can be modified by radiation pressure, such that dust grains can migrate inward/outward when they move faster/slower than the gas azimuthally. Takeuchi and Lin (2003) then extended their study to optically thick accretion disks. They found that in a disk similar to the minimum mass solar nebula (MMSN), dust grains only migrate outward on the disk surface, and the outward flux is negligible compared with the inward accretion flow on the midplane. Chiang and Murray-Clay (2007) suggested that radiation pressure can blow out dust grains in a gaseous rim that is unstable to the magneto-rotational instability. Later, Dominik and Dullemond (2011) argued that it cannot. They showed that in a one-dimensional (1D), axisymmetric, vertically averaged picture, radiation pressure can be overcome by the combined effects of dust pileup and gas accretion. Then, Owen and Kollmeier (2019) added grain size evolution to the analysis, and generalized it to two-dimensional (2D; radial and vertical). They showed that at a pressure bump created by photoevaporation, small dust grains are lifted to higher altitudes, where they are removed by radiation pressure and then replenished by the fragmentation of larger grains, ultimately leading to the removal of all dust. In this picture, the transitional disk cavity would be cleared by photoevaporation instead of radiation pressure (e.g., Picogna et al. 2019; Ercolano et al. 2021). Krumholz et al. (2020) revisited the problem for smooth disks without pressure bumps, and showed that for low-mass disks ($\lesssim$1% of MMSN) with accretion rates lower than $\sim 10^{-11} M_\odot$ per year, radiation pressure can remove micron-sized grains from the inner disk even without the aid of a pressure bump. So it seems, when it comes to disks that are as gas-rich as MMSN, radiation pressure will no longer be a promising mechanism to open transitional disk cavities.

Here, we show that there is another level of complexity that previous studies have not considered, and it can open an avenue to cavity clearing even for gas-rich disks. In essence, a newly found instability at the disk edge can break the axisymmetry that was commonly assumed, generating a host of rich and new dust dynamics, including the formation of small, high-density dust features that we refer to as clumps. We demonstrate this directly using 2D, vertically averaged numerical models. The instability in this work is similar to the irradiation instability in Fung and Artymowicz (2014) as both of them are associated with radiation and extinction, and require a sharp radial transition between optically thin and thick. However, we show that they are different as the instability demonstrated in this dissertation does not require the participation of the gas component (except for the drag force on the dust).

While demonstrating our new mechanism of forming dust substructures via radiation pressure and instability, an immediate question that comes to our mind is how to distinguish similar dust substructures formed by different mechanisms. Particularly, we want to know whether those dust substructures are formed by planets or not, as it is the key to solving the "chicken and egg" puzzle. A good entry point to begin our investigation with would be the dust ring, one of the most commonly observed substructures in the disk (e.g., Huang et al. 2018b, Long et al. 2018, van der Marel et al. 2019). So far, several mechanisms that lead to the formation of dust rings have been reported, such as dust rings formed via magneto-hydrodynamic effects (e.g., Johansen et al. 2009), chemical-related dust evolution (e.g., Zhang et al. 2015), various dynamical instabilities (e.g., Youdin 2011), and self-maintenance due to dust back-reaction (e.g., Jiang and Ormel 2021). Apart from those, gap-opening planets have also become a popular explanation for the formation of dust rings. This is because pressure bumps naturally arise from the gap-opening process by massive planets (e.g., Lin and Papaloizou 1993), which then trap and concentrate dust grains via aerodynamic effects. However, given all of those mechanisms and numerous observations revealing dust rings in disks, a clear way to correlate a specific ring to a specific mechanism is still yet to be established.

In Chapter 3, we seek correlations between a gap-opening planet and the radial width of the dust ring that the planet forms. Dust rings have different radial widths, with the ratio between the deconvolved full width at half maximum (FWHM) and the radius ranging from $\lesssim$10% (e.g., AS 209, Huang et al. 2018b) to $\gtrsim$90% (e.g., EM* SR 24S, Cieza et al. 2021) (see Figure 1.1). This wide range of widths indicates different

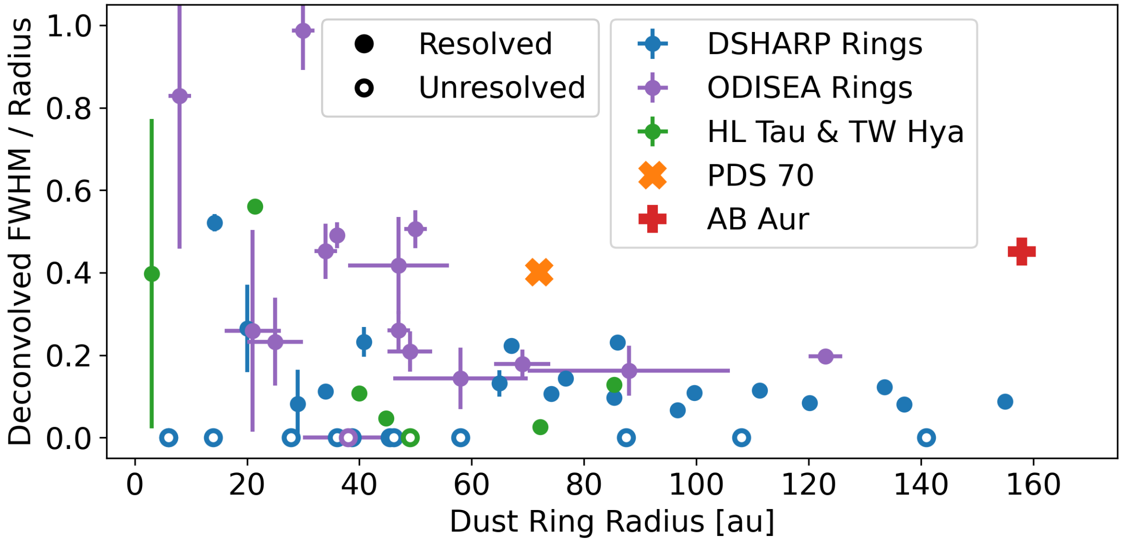

Figure 1.1: The ratio between the deconvolved full width at half maximum (FWHM) and the radius of observed dust rings. The deconvolution method can be found in Dullemond et al. (2018), with unresolved widths set to zero (open circles in the plot). Samples are selected from the DSHARP Program (Andrews et al. 2018; Huang et al. 2018b), the ODISEA Program (Cieza et al. 2021), HL Tau (ALMA Partnership et al. 2015), TW Hya (Huang et al. 2018a), PDS 70 (Benisty et al. 2021; Portilla-Revelo et al. 2022), and AB Aur (Tang et al. 2017). Rings without errorbars in the DSHARP Program are not sampled.

relative strengths of dust trapping (e.g., gas drag in the pressure bump, Takeuchi and Lin 2002; Paardekooper and Mellema 2004; or traffic jams in the radial drift, Okuzumi et al. 2016; Jiang and Ormel 2021) and dust diffusion (e.g., turbulence-induced diffusion, Youdin and Lithwick 2007). Meanwhile, we noticed that in PDS 70, where two planets have been detected in the gap next to a dust ring (Keppler et al. 2018; Haffert et al. 2019; Benisty et al. 2021), the dust ring is visibly wider compared with many other well-resolved rings from disk surveys (see Figure 1.1). Similar things happen to AB Aur, where a planet is also detected next to a wide dust ring (Tang et al. 2017; Currie et al. 2022). We, therefore, question whether this large ring width is associated with planets, and how much, if associated, the planet can widen the dust ring.

We perform three-dimensional (3D) grid-based hydrodynamic simulations of dusty protoplanetary disks with embedded gap-opening planets. We find that the planet can widen dust rings trapped at the pressure bump (see Figure 1.2). We also provide an analytical approach to estimate the dust ring width in such a scenario. Our results suggest that gap-opening planets could be a potential explanation for wide dust rings

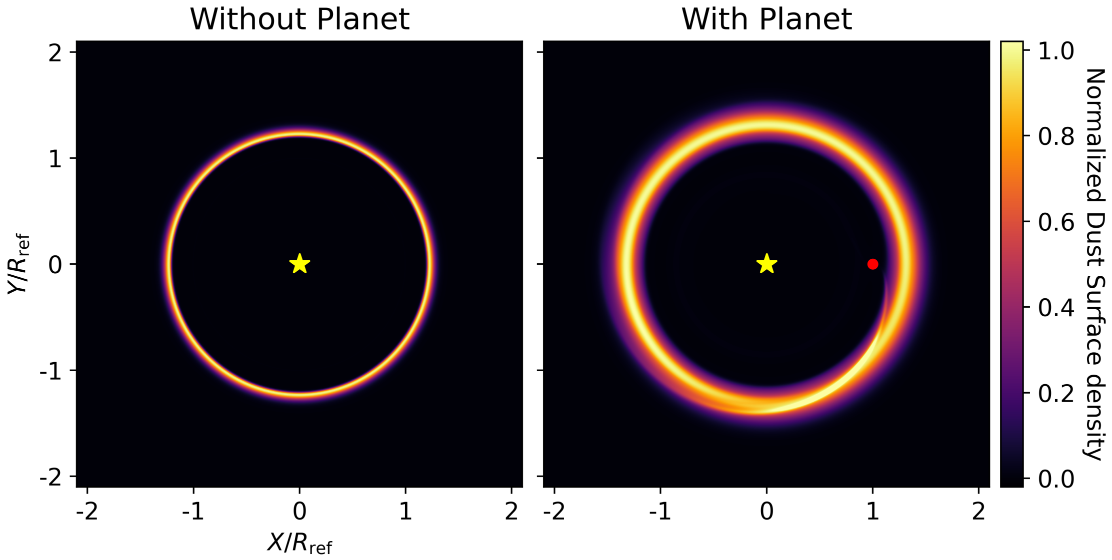

Figure 1.2: Comparison of dust rings showing the effect of the planet. The left panel shows a dust ring in a disk model with no planet (Model C1), and the right panel shows a dust ring in the disk with a Saturn-mass gap-opening planet (Model C5, see Section 3.1.2 and 3.2.1 for descriptions and applications). Both face-on view snapshots are taken at $t = 1000 P_{\rm K,ref}$ in each model, and are normalized individually by the radial peak in the azimuthally averaged profile. The radial profiles of dust surface density are shown in Figure 3.1. The yellow star indicates the location of the central star and the red dot indicates the location of the planet.

in the disks.

Chapter 2

In the Pre-Planet-Formation Era: Dust Dynamics under Irradiation Instability in Transitional Disks

The chapter is organized as follows: We first describe our methodology of simulating dust grains and the numerical modeling in Section 2.1. We present our results in Section 2.2, starting with the clumping effects of dust grains and followed by the recession of the disk edge. We discuss the possible effects of a few neglected mechanisms in Section 2.3. Finally, we conclude in Section 2.4.

2.1 Numerical Method

We develop a graphics processing unit (GPU) particle code to simulate dust grains in a gaseous disk. It employs the staggered semi-analytic method (SSA; Fung and Muley 2019), which is designed to achieve high accuracy when the equation of motion is *stiff*, i.e., when the stopping time of dust grains is much shorter than the integration time step, which is the case for our models, where the Stokes number can be as small as 10^{-5}.

Dust grains in our models interact with each other through shadowing. We compute the optical depth of the dust disk in 2D grids using the *cloud-in-cell* (CIC) prescription (e.g., Chapter 1.5.2, Hockney and Eastwood 1981). Each simulated particle, called a *super-particle*, represents a cloud of dust grains of the size of one grid cell. To compute the optical depth τ, we first evaluate the disk's dust surface density $\Sigma_{\rm d}$ by distributing the mass of each super-particle into its four closest neighboring grid cells through bilinear interpolation. The $\Sigma_{\rm d}$ grids are then converted into the τ

grids using the opacity of dust $\kappa_{\rm opa}$

$$\tau(r,\phi) = \int_0^r \kappa_{\rm opa} \frac{\Sigma_{\rm d}(r',\phi)}{h(r')} \,{\rm d}r' \,, \tag{2.1}$$

where h is the disk scale height, which we assume to be proportional to the radius r such that the disk aspect ratio $H_{\rm g}/r$ is a constant. The values of $\kappa_{\rm opa}$ and $H_{\rm g}/r$ will be discussed in the following section. Finally, the τ value at the position of a given super-particle is extracted from the τ grids again through bilinear interpolation.

The CIC method of computing τ estimates the averaged τ in the cloud of dust grains that a single super-particle represents. This implies that super-particles can self-shadow. In other words, even when there is no dust between the star and a super-particle, the τ value at its position will still not be zero because the front end of the cloud casts a shadow on its back end. The amount of self-shadowing is small, equaling about half of the optical thickness of the super-particle, and is generally not consequential, but it does have an effect when there is an optically thick concentration of dust on a scale smaller than a grid cell.

2.1.1 Model Description

We consider a 2D protoplanetary disk where dust grains and a steady gaseous disk orbit a central star of mass $M_\star$. We use $\{r,\ \phi\}$ to denote radius and azimuth in the 2D polar coordinates, respectively. The coordinate system is fixed and centered on the star. Hereafter, we use the subscript "ref" to denote any evaluations at the reference radius $r_{\rm ref}$.

We use 10^7 super-particles in our fiducial model to resolve our dust disk. Each of them represents a cloud of dust grains that share the same internal density $\rho_\bullet$ and grain size s. In our models, all super-particles have the same s. We will discuss the possible effects of the grain size distribution in Section 2.3.2.

To compute gas drag on the dust, we assume the grains are subjected to the subsonic Epstein drag, such that the stopping time is $t_{\rm s} = \rho_\bullet s/\rho_{\rm g} c_{\rm s}$ (Weidenschilling 1977a), where $\rho_{\rm g}$ and $c_{\rm s}$ are the volumetric density and sound speed of gas, respectively. The parameterized evaluation of $t_{\rm s}$ reads as

$$t_{\rm s} = \frac{\Sigma_{\rm g,ref}}{\Sigma_{\rm g}} \frac{c_{\rm s,ref}}{c_{\rm s}} \frac{{\rm St}_{\rm ref}}{\Omega_{\rm K,ref}}, \tag{2.2}$$

where $\Sigma_{\rm g}$ is the surface density of gas, St is the Stokes number of dust, and $\Omega_{\rm K}(r) =$

$\sqrt{GM_\star/r^3}$ is the Keplerian angular velocity[1]. Epstein drag applies when the grain size is insignificant compared with the mean free path of gas, which is typically satisfied for micron-sized grains in protoplanetary disks. In our parameter space, we also expect that gas drag can keep the dust-to-gas relative motion subsonic. Retrospectively, indeed we find in our models that the dust-to-gas speed is typically slower than 1% of the sound speed.

Given this drag force, we integrate the following equation of motion in our code

$$\boldsymbol{a} = \boldsymbol{f}(t, \boldsymbol{x}, \boldsymbol{W}) + \frac{\boldsymbol{V}(t, \boldsymbol{x}) - \boldsymbol{W}}{t_{\rm s}(t, \boldsymbol{x})}, \tag{2.3}$$

where $\boldsymbol{a}, \boldsymbol{x}, \boldsymbol{W}$ are the acceleration, position, and velocity of dust, $\boldsymbol{f}$ is the specific force acting on the dust except for gas drag, and $\boldsymbol{V}$ is the gas velocity. In this study, the radial and azimuthal components of $\boldsymbol{f}$ are

$$f_{\rm r} = -\frac{GM_\star}{r^2}(1 - \beta e^{-\tau}), \tag{2.4}$$

$$f_\phi = 0. \tag{2.5}$$

The absolute ratio between radiation pressure and gravity is

$$\beta = \frac{\kappa_{\rm abs} L}{4\pi c GM_\star}, \tag{2.6}$$

where $\kappa_{\rm abs}$ is the particle mass absorption coefficient, L is the stellar luminosity, and c is the speed of light. Micron-sized dust grains have typical β values of ∼0.2–4 for T Tauri stars and ∼4–4000 for Herbig Ae/Be stars (Garufi et al. 2020; Guzmán-Díaz et al. 2021). We note that $\kappa_{\rm abs}$ is different from $\kappa_{\rm opa}$ used in Equation 2.1, as the opacity $\kappa_{\rm opa}$ includes both extinction due to absorption ($\kappa_{\rm abs}$) and scattering. In our models, we do not explicitly set the value of all parameters on the right-hand side of Equation 2.6. Instead, we set values for β, which allows us to generalize our models to any combination of L, $M_\star$, and $\kappa_{\rm abs}$.

---

[1] Here, we note that $P_{\rm K,ref} = 2\pi\Omega_{\rm K,ref}^{-1}$ will be used as the reference orbital period in this chapter.

2.1.2 Initialization

We assign the initial radial position of super-particles using a probability distribution of the total dust mass M in the disk

$$\frac{\mathrm{d}M}{\mathrm{d}r}(r) = (2\pi r \Sigma_\mathrm{d}') * G = 2\pi \int_0^\infty r \Sigma_\mathrm{d}'(r')\, G(r - r')\, \mathrm{d}r', \tag{2.7}$$

where $*$ is the convolution operator,

$$\Sigma_\mathrm{d}'(r) = \begin{cases} \Sigma_\mathrm{d0}\left(r/r_\mathrm{ref}\right)^{-3/2}, & 1.0 \le r/r_\mathrm{ref} \le 1.5; \\ 0, & \text{else}, \end{cases} \tag{2.8}$$

$$G(r) = \frac{1}{\sqrt{2\pi} \times 0.02 r_\mathrm{ref}} \exp\left(-\frac{r^2}{2 \times (0.02 r_\mathrm{ref})^2}\right), \tag{2.9}$$

r_ref is a constant that equals one in code units, and Σ_d0 is a normalization factor of the initial profile that we adjust according to the total optical depth of the disk (see below). The initial dust surface density profile is therefore $\Sigma_\mathrm{d}(r) = (\mathrm{d}M/\mathrm{d}r)/(2\pi r)$, which gives a smoothed-edge dust ring between roughly $1.0 r_\mathrm{ref}$ and $1.5 r_\mathrm{ref}$. The initial azimuthal position of super-particles is assigned using a uniform probability distribution between 0 and 2π.

In this chapter, we use $\langle\,\rangle$ to denote azimuthal averaging, such that $\langle\tau\rangle$ is the azimuthally averaged τ. We also define

$$\langle\tau'\rangle = -\log\langle e^{-\tau}\rangle \tag{2.10}$$

as the *effective optical depth* that relates to the azimuthally averaged amount of extinction. We refer to the radius where $\langle\tau'\rangle = 1$ as the *optical edge* of the disk. Note that τ, $\langle\tau\rangle$, and $\langle\tau'\rangle$ are only equal when the dust distribution is axisymmetric; they are not the same when the disk develops asymmetric structures. Later in Section 2.2, we will be using their differences to quantify asymmetry in our disks.

The total amount of dust in our model is normalized according to τ of the disk. In our fiducial model, we set $\langle\tau\rangle$ at the peak of the Σ_d profile (at $\sim 1.05 r_\mathrm{ref}$) to 10. To apply this normalization to Σ_d, we assume that $r_\mathrm{ref} = 1$ au, $s = 1$ μm, $\rho_\bullet = 1.5$ g/cm^3, $H_\mathrm{g}/r = 0.05$, and κ_opa is given by the geometric opacity

$$\kappa_\mathrm{opa} = \frac{\pi s^2}{{}^4\!/\!_3\, \pi s^3 \rho_\bullet} = 0.5 \left(\frac{s}{1\,\mathrm{cm}}\right)^{-1} \mathrm{cm}^2\mathrm{g}^{-1}. \tag{2.11}$$

It gives $\Sigma_{\rm d0} = 7.7 \times 10^{-3}$ g/cm^2 for micron-sized dust grains in our fiducial model[2]. We emphasize that $\Sigma_{\rm d0}$ represents only the micron-sized grains — if we assume that the dust grains follow a grain size distribution $\mathrm{d}n_{\rm s} \propto s^{-3.5}\,\mathrm{d}s$ (Mathis et al. 1977) from 1 μm to 1 km, our model would produce a total dust density of about 2.4×10^2 g/cm^2, corresponding to a dust-to-gas ratio of about 0.14, assuming the gas follows the MMSN at 1 au (Weidenschilling 1977b; Hayashi 1981). We will study the effects of different levels of τ by varying the value of $\Sigma_{\rm d0}$.

For the purpose of computing gas drag, we assume a steady background gas surface density profile that follows $\Sigma_{\rm g} \propto (r/r_{\rm ref})^{-p}$ and a sound speed profile $c_{\rm s} \propto (r/r_{\rm ref})^{-q/2}$, where $p = 1.5$ and $q = 1$. The gas velocities assume hydrostatic equilibrium

$$V_r = 0, \tag{2.12}$$

$$V_\phi = v_{\rm K}\sqrt{1-\eta}, \tag{2.13}$$

where $v_{\rm K} = r\Omega_{\rm K}$ is the Keplerian velocity, and $\eta = (p+q)(H_{\rm g}/r)^2$ is the pressure-related term. The gas density is not explicitly normalized but rather incorporated into the value of the Stokes number $\mathrm{St}_{\rm ref}$.

When initializing our super-particles, we assign them Keplerian orbital velocities

$$W_r = 0, \tag{2.14}$$

$$W_\phi = v_{\rm K}. \tag{2.15}$$

As soon as the simulation begins, gas drag will cause a headwind on super-particles and lead to their radial drift. At the same time, radiation pressure will push super-particles outward if they lie on the optically thin disk edge. Although these motions are not captured in the initialization, the values of $\mathrm{St}_{\rm ref}$ we use are sufficiently small (i.e., the gas-dust coupling is sufficiently strong) such that super-particles can adjust to gas drag within a dynamical time $\Omega_{\rm K}^{-1}$. Subsequently, dust dynamics is not sensitive to the initial velocities.

Finally, for our parameter space study, we consider β values ranging from 0.01 to 20, $\mathrm{St}_{\rm ref}$ from 10^{-5} to 10^{-2}, and $\Sigma_{\rm d0}$ from 2.3×10^{-3} to 7.7×10^{-2} g/cm^2 (i.e., τ from 3 to 100 at the radius of the initial surface density peak). We refer to the $\{\beta,\, \mathrm{St}_{\rm ref},\, \Sigma_{\rm d0}\} = \{10,\, 10^{-4},\, 7.7 \times 10^{-3}\}$ setup as our fiducial model.

---

[2] Hereafter, the unit of $\Sigma_{\rm d0}$ is g/cm^2, if unspecified.

2.1.3 Domain and Resolution

Our Σ_d and τ grids are defined in a domain that extends radially from $0.95r_\mathrm{ref}$ to $1.55r_\mathrm{ref}$, and azimuthally around the full 2π. Σ_d is defined at the center of each grid cell, and set to zero outside the domain. τ is defined at the center of the outer radial boundary of each grid cell, set to zero within the inner domain boundary, and infinity beyond the outer domain boundary. In other words, the disk is always optically thin within $0.95r_\mathrm{ref}$ and optically thick outside $1.55r_\mathrm{ref}$. In most of our models, super-particles do not leave the domain.

The fiducial resolutions are $N_\mathrm{r} \times N_\phi = 1024 \times 1024$, with grid cells spaced logarithmically in the radial direction and uniformly in the azimuthal direction. We adopt a fixed time step $\delta t = 2\pi/(N_\phi \Omega_\mathrm{K,ref})$ that is sufficient to ensure particles do not skip grid cells during integration. In the following section, we examine the validity of these choices by running convergence tests.

2.1.4 Convergence Test of Numerical Parameters

We run convergence tests for particle resolution N_par, radial resolution N_r, azimuthal resolution N_ϕ, and time step δt. The aim is to obtain converged results on the movement of the optical edge (where $\langle \tau' \rangle = 1$). All tests are performed using our fiducial set of $\{\beta, \mathrm{St}_\mathrm{ref}, \Sigma_\mathrm{d0}\}$. The results are shown in Figure 2.1 and described below.

It is important to note that the instability that drives the evolution of these models grows from the random noise in the initialization of the super-particles. As we vary numerical parameters, that initial noise is changed and that leads to a slightly different simulation, even if all physical parameters remain unchanged. This means we do not expect to find precise convergence, but we do consider our simulations robust as long as there is convergence in the phenomenological behavior of the models and the quantitative measurements do not vary by more than ∼10–20%.

Particle Resolution We try super-particle numbers ranging from 10^6 to 10^8, and compare with the result of the fiducial value 10^7. We find good convergence in the edge location as long as the number is larger than 10^6, as seen in the top panel of Figure 2.1.

Radial Resolution We vary the radial grid resolution in this test. In the second panel of Figure 2.1, we identify good convergence when $N_{\rm r} \gtrsim 512$.

Azimuthal Resolution Similar to the previous test, here we vary the azimuthal grid resolution. In the third panel of Figure 2.1, we find good convergence in both the edge location and the recession speed within the time domain of the test simulations. Generally, the disks appear to recede faster with higher azimuthal resolutions. With higher azimuthal resolution, the size of each super-particle is effectively smaller (see Section 2.1), making it easier for radiation pressure to leak around opaque regions. So given the same initial distribution of super-particles, the true recession speed may be higher than what we measure, but unlikely to be lower.

Time Step In our last test, we vary the time step. The last panel of Figure 2.1 shows that the edge location is well converged.

2.2 Results

2.2.1 The Asymmetric Disk Edge

Our simulations typically evolve as follows. In the initial phase, dust grains that are in the optically thin region are pushed outward by radiation pressure. This migration of dust leads to the formation of a sharp dust wall. Slight variations in density along this wall are amplified over time. The lower-density segments are pushed back at higher speeds, and they become radially separated from the denser segments. The Keplerian shear then takes these lower-density segments to the back of the denser segments. Due to shadowing, the front of the wall always recedes faster than the back. This simulates a radial compression that adds to the density of the already dense segments, which we refer to as *clumps*. This process is broken down in Figure 2.2.

To create these asymmetric features, a sufficiently sharp dust wall must form first, in other words, $(\mathrm{d}\tau/\mathrm{d}r)e^{-\tau}$ must be large. Otherwise, the Keplerian shear will smear local density differences before the high- and low-density segments can separate radially. This is analogous to the instability described in Fung and Artymowicz (2014), which also relies on radial compression due to shadowing and requires a sharp transition from optically thin to thick.

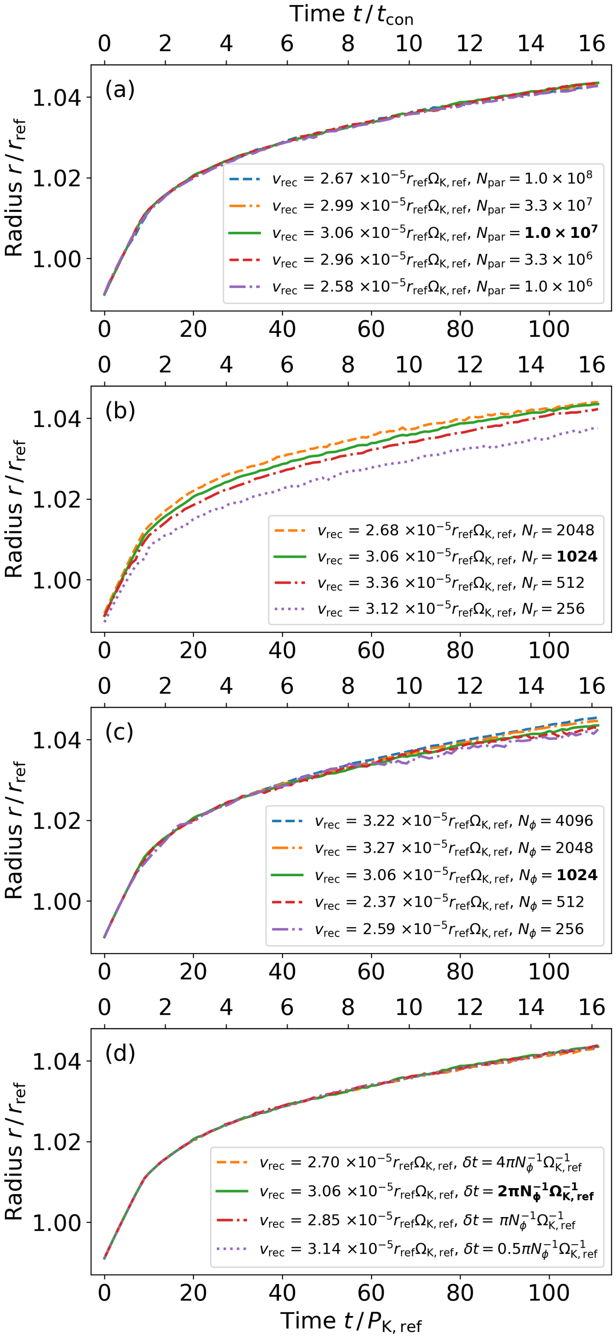

Figure 2.1: Convergence tests in terms of the time evolution of the optical edge. (a): The convergence test of the super-particle resolution $N_{\rm par}$. **(b):** The convergence test of the radial resolution N_r. **(c):** The convergence test of the azimuthal resolution N_ϕ. **(d):** The convergence test of the time step δt. The top axis labels the simulation time in the unit of the concentration timescale (see Section 2.2.2). The bottom axis labels the simulation time in the unit of the reference orbital period. The legend labels the recession speed of the optical edge (see Section 2.2.4), with the fiducial parameters marked in bold.

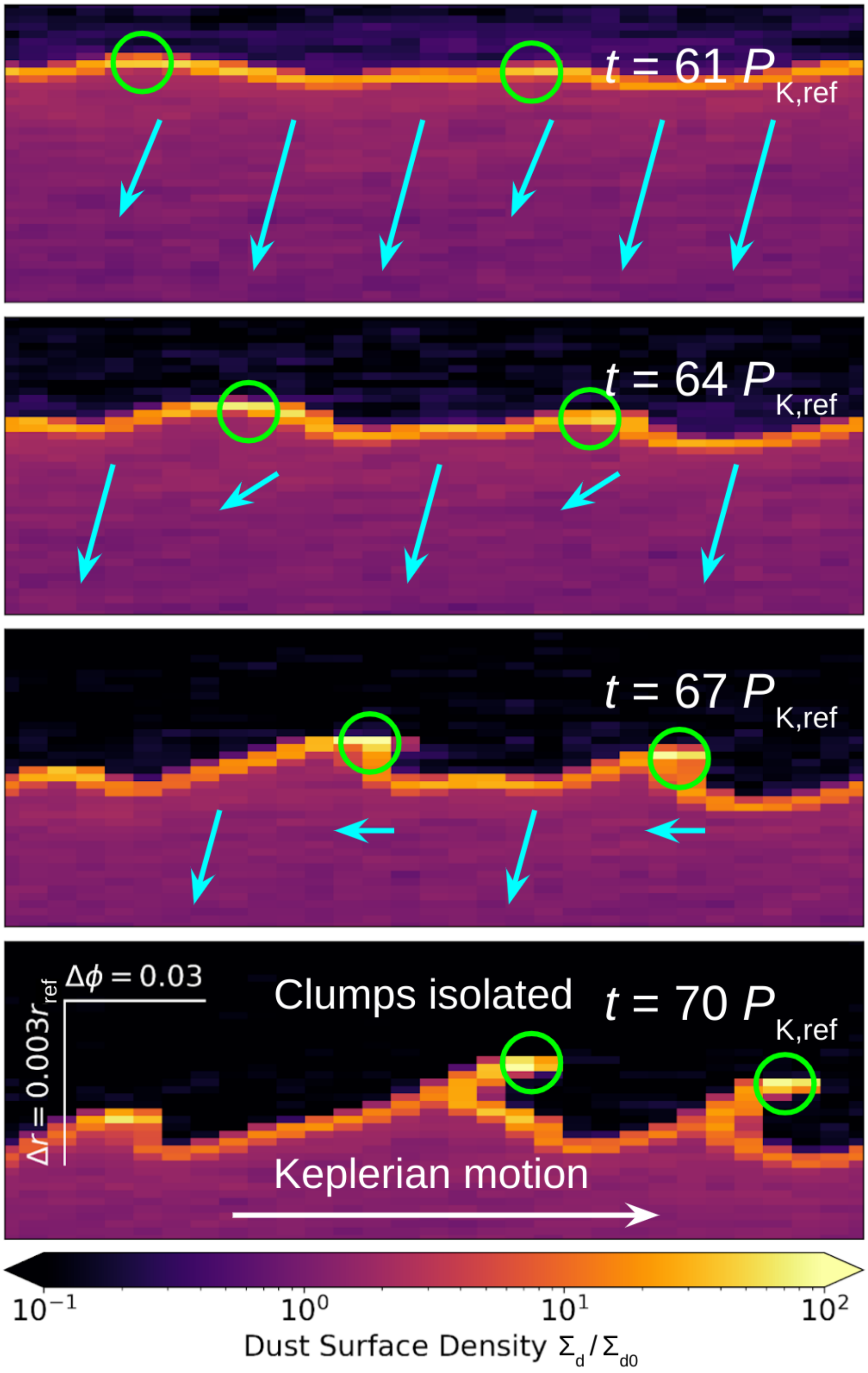

Figure 2.2: Time evolution of the dust surface density breaking down the steps of clump formation. The snapshots are taken from the model with $\beta = 1$, $\mathrm{St_{ref}} = 10^{-4}$, and $\Sigma_{\mathrm{d0}} = 7.7 \times 10^{-3}$ g/cm^2. The green circles mark the location of the overdensities at the disk edge, and the cyan arrows mark the motion of disk material at different azimuths relative to the overdensities.

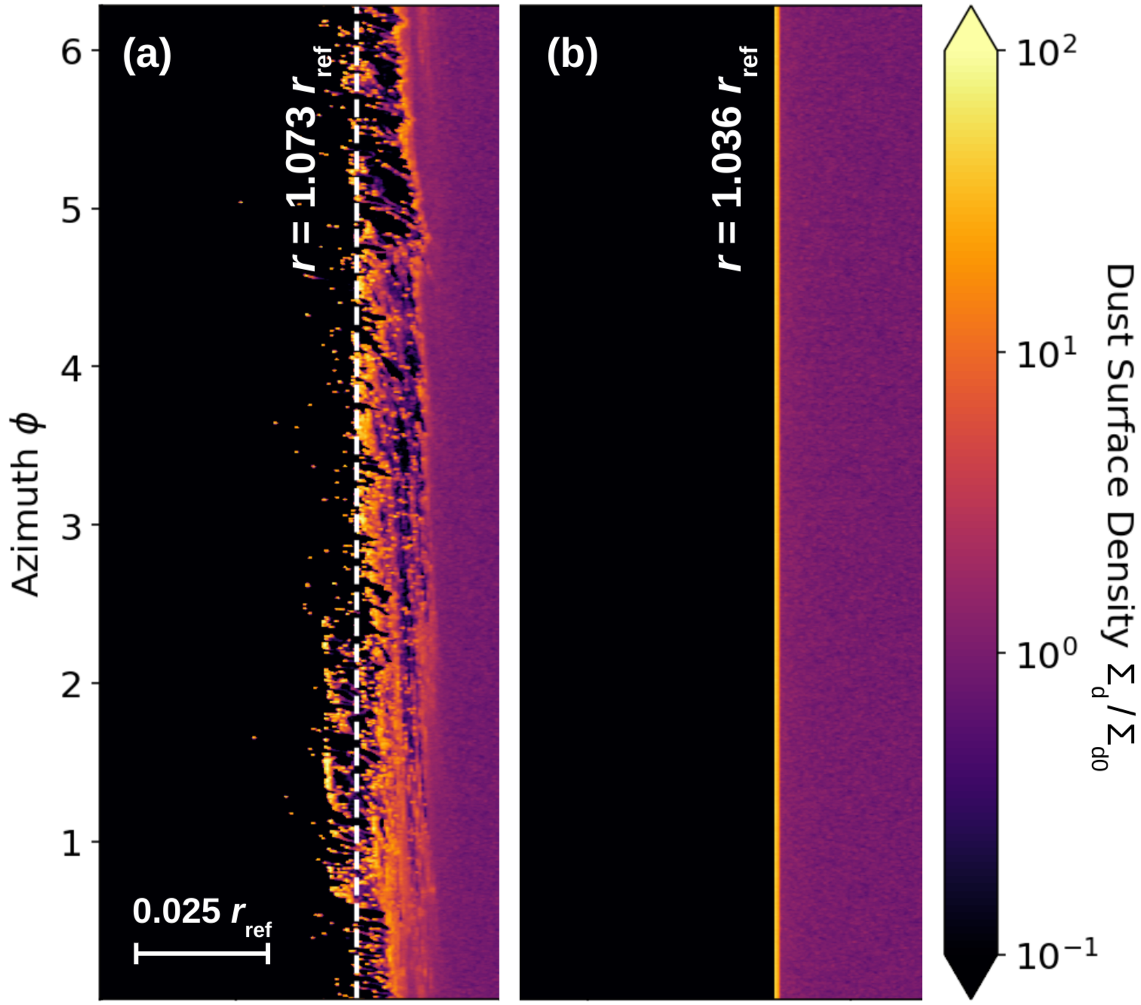

Figure 2.3: Comparison of disk edges showing the effect of the instability. The snapshots are taken at $t = 500P_{\mathrm{K,ref}}$ in **(a)** the fiducial model and **(b)** the instability-inactivated model. In the latter case, the optical depth τ is azimuthally averaged at every time step.

Common models of dust migration due to radiation pressure assume axisymmetry. Figure 2.3 illustrates what would happen if we enforce such a condition. On the right panel, we inactivate the instability by artificially setting τ equal to its azimuthally averaged value $\langle\tau\rangle$ at every time step. The disk edge then develops into a dense but symmetric wall. We note that the disk edges are formed at different radii in the two models, which means that the clump formation has a qualitative effect on the radial migration of dust. We will discuss this in Section 2.2.4.

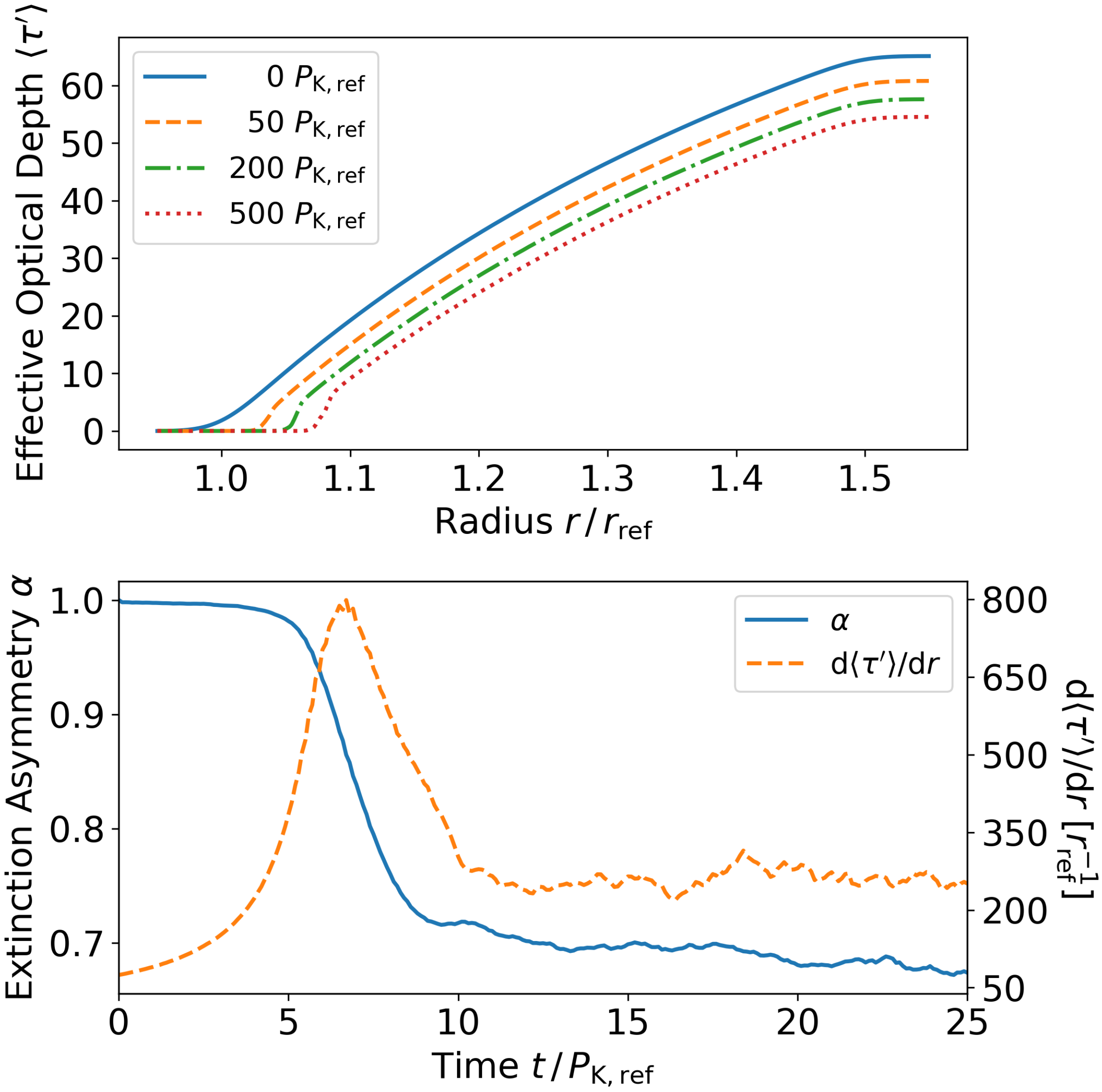

Figure 2.4: Time evolution of the effective optical depth and the extinction asymmetry. **Upper:** The effective optical depth $\langle \tau' \rangle$ in the disk. **Lower:** The extinction asymmetry parameter α and the radial gradient of the effective optical depth $\mathrm{d}\langle \tau' \rangle / \mathrm{d}r$. Both values are measured at the optical edge in the fiducial model.

2.2.2 Clump Formation and Destruction

The formation of high-density dust clumps at the inner edge of illuminated disks is important in many ways. The one that we focus on here is that it reduces the optical depth of the disk (upper panel of Figure 2.4). This reduction allows radiation to penetrate deeper into the disk and change the course of dust migration.

Instead of looking at individual clumps, we measure their collective influence using an *extinction asymmetry* parameter α, which we define as

$$\alpha = \frac{1 - e^{-\langle \tau' \rangle}}{1 - e^{-\langle \tau \rangle}}. \tag{2.16}$$

α is measured at the optical edge (where $\langle \tau' \rangle = 1$). Since $\langle \tau' \rangle < \langle \tau \rangle$ in general, we have $1 - e^{-1} < \alpha \leq 1$ at the optical edge, with a smaller α denoting more effective clumping.

As mentioned, clump formation begins with the formation of a sharp dust wall. The lower panel of Figure 2.4 shows the time evolution of α and the radial gradient of $\langle \tau' \rangle$ in the fiducial model. Initially, $\mathrm{d}\langle \tau' \rangle / \mathrm{d}r$ increases as the dust wall forms, while α remains at $\sim$1. Once $\mathrm{d}\langle \tau' \rangle / \mathrm{d}r$ goes above $\sim 500 r_{\mathrm{ref}}^{-1}$, α starts to decrease, signaling clump formation. Isolated clumps that are optically thick are separated from the disk edge, which is still being pushed outward by radiation pressure. This causes $\mathrm{d}\langle \tau' \rangle / \mathrm{d}r$ to decrease as α continues to fall. Eventually, both $\mathrm{d}\langle \tau' \rangle / \mathrm{d}r$ and α stabilize. α stabilizes because it has almost approached the minimum value $1 - e^{-1}$. $\mathrm{d}\langle \tau' \rangle / \mathrm{d}r$ stabilizes because clump formation and destruction are near equilibrium.

In our simulations, clumps are not held together by any internal forces[3]. When dust grains are apart from the clump body by roughly one grid size azimuthally, the exposure to much stronger radiation pushes them outward rapidly. Therefore, the destruction timescale of clumps is related to our numerical resolution. Smaller clumps survive longer in our simulations, sometimes as long as our simulation time. The shredded clumps form a new wall behind the existing clumps, where the next generation of clump formation begins.

There are a number of simplifications in our model that may affect the physics of clump formation. First, forming a sharp dust wall is a prerequisite for clump formation, but to form such a wall requires the radial concentration of the disk edge to overcome diffusive effects such as grain collisions and gas turbulence[4]. Here, we define a concentration timescale

$$t_{\mathrm{con}} = \frac{\Delta r_{\mathrm{trans}}}{\Delta v_{r,\mathrm{term}}} \tag{2.17}$$

to estimate the time for the initial optical depth transition to become sufficiently

---

[3] Although, in reality, they could be held together by self-gravity.

[4] We note that the lack of collision and turbulence in our study leads to the diffusion timescale being infinite, which means that the optical depth transition is always able to become sufficiently sharp to trigger effective clump formation.

sharp to trigger effective clump formation. $\Delta r_{\mathrm{trans}}$ is the radial extent of the optical depth transition that varies with Σ_{d0}. In this study, we define $\Delta r_{\mathrm{trans}}$ numerically from where $\langle\tau\rangle = 0.1$ to where $\langle\tau\rangle = 1$ in the initial profile. $\Delta v_{r,\mathrm{term}}$ is the difference between the radial terminal velocity of dust at the inner and outer edges of the optical depth transition discussed above (see Equation A.1).

This concentration time t_{con} determines the time to form a dust wall, and therefore the time to form clumps. In Figure 2.5 we show α values at the optical edge with a variety of β, $\mathrm{St}_{\mathrm{ref}}$, and Σ_{d0} (see Table 2.1) at different simulation time. It is clear that when $t = t_{\mathrm{con}}$, the initially axisymmetric optical edge starts to become clumpy, and ends up with $\alpha \sim 1 - \mathrm{e}^{-1}$ when $t \gg t_{\mathrm{con}}$. The result remains self-similar over time. Given sufficient time, all of our diffusion-less models will develop clumps. With some diffusion, clump formation may cease to occur if t_{con} is too long.

We also note that the parameter space in Table 2.1 focuses on the regime where the gas-dust coupling is strong ($\mathrm{St}_{\mathrm{ref}} \ll 1$). This is because a certain level of gas drag is necessary to form clumps. Because radiation pressure is a radial force that does not modify the orbital angular momentum of dust grains, Without the dissipation from gas drag, dust grains would conserve their orbital angular momentum, and only evolve their orbital energy. This would lead to the excitation of their eccentricities, increasing the overall velocity dispersion in the disk, and erasing organized structures like clumps.

Finally, we note that dust grains may be able to drift out of our simulation domain at $t = 500P_{\mathrm{K,ref}}$ in models with low values of β and high values of $\mathrm{St}_{\mathrm{ref}}$ (e.g., $\beta = 10^{-2}$, $\mathrm{St}_{\mathrm{ref}} = 10^{-2}$). In those models, the inward drift is so fast that the edge is not able to develop any asymmetry before leaving the domain. This is essentially a numerical issue, and the corresponding markers in the bottom panel of Figure 2.5 have been removed for clarity. However, it also casts light on the competition between clump formation and the inward drift, which plays a critical role in the disk edge dynamics described in Section 2.2.4.

2.2.3 The Optical Thickness of Clumps

In our models, dust grains only interact through shadowing. This means the optical thickness of individual clumps, i.e, their contribution to the optical depth, directly determines their influence on dust dynamics. In this section, we investigate the evolution of clumps by tracing their optical thickness.

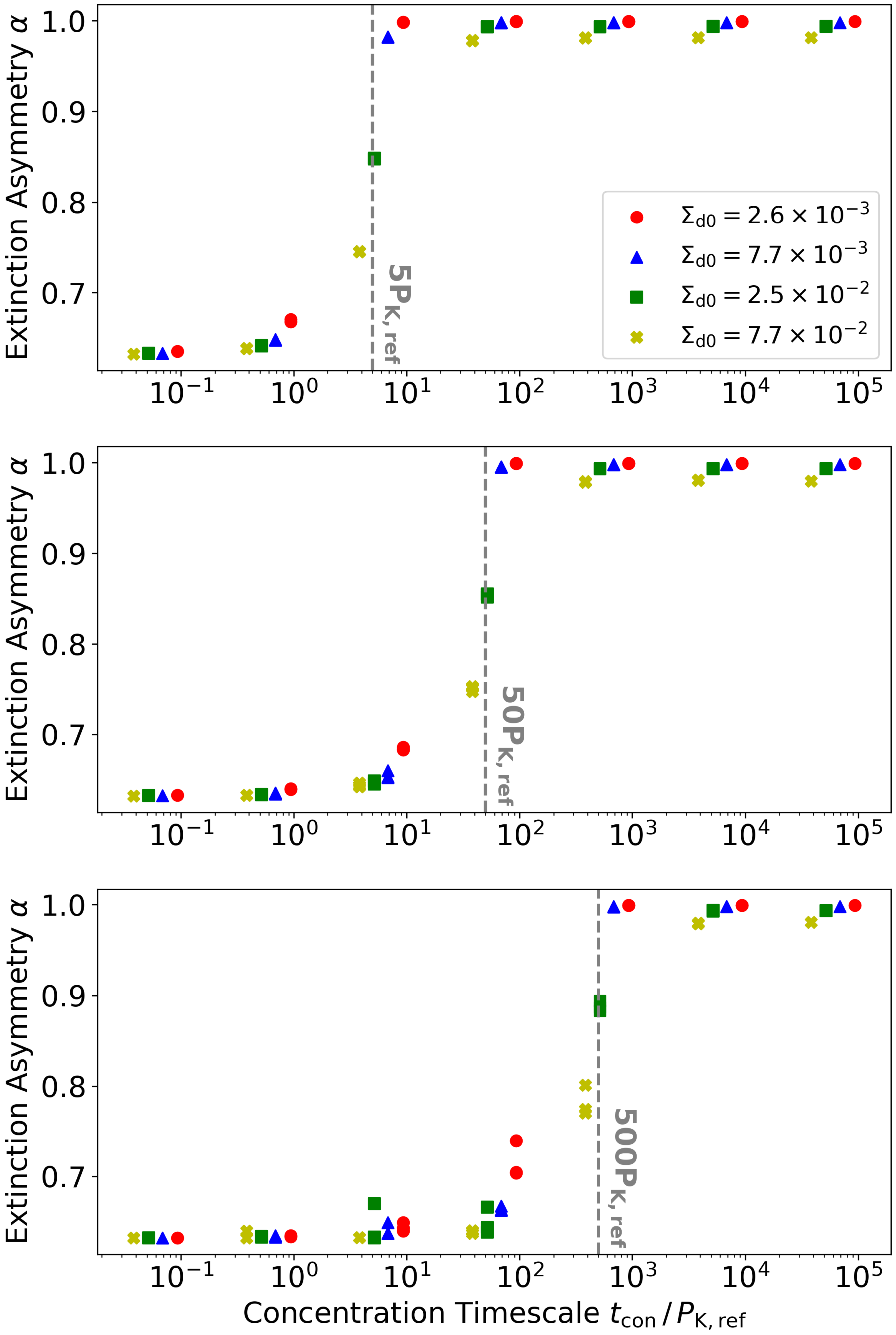

Figure 2.5: Snapshots of the extinction asymmetry parameter in models with different concentration timescales. Snapshots are taken at $t = 5P_{\mathrm{K,ref}}$ (*upper*), $t = 50P_{\mathrm{K,ref}}$ (*middle*), and $t = 500P_{\mathrm{K,ref}}$ (*lower*). The parameter space for different t_{con} is listed in Table 2.1. We note that a large fraction of the sample is hidden by the overlapping of markers. Models with different Σ_{d0} suffer from different levels of Poisson noise that may affect the initial axisymmetry.

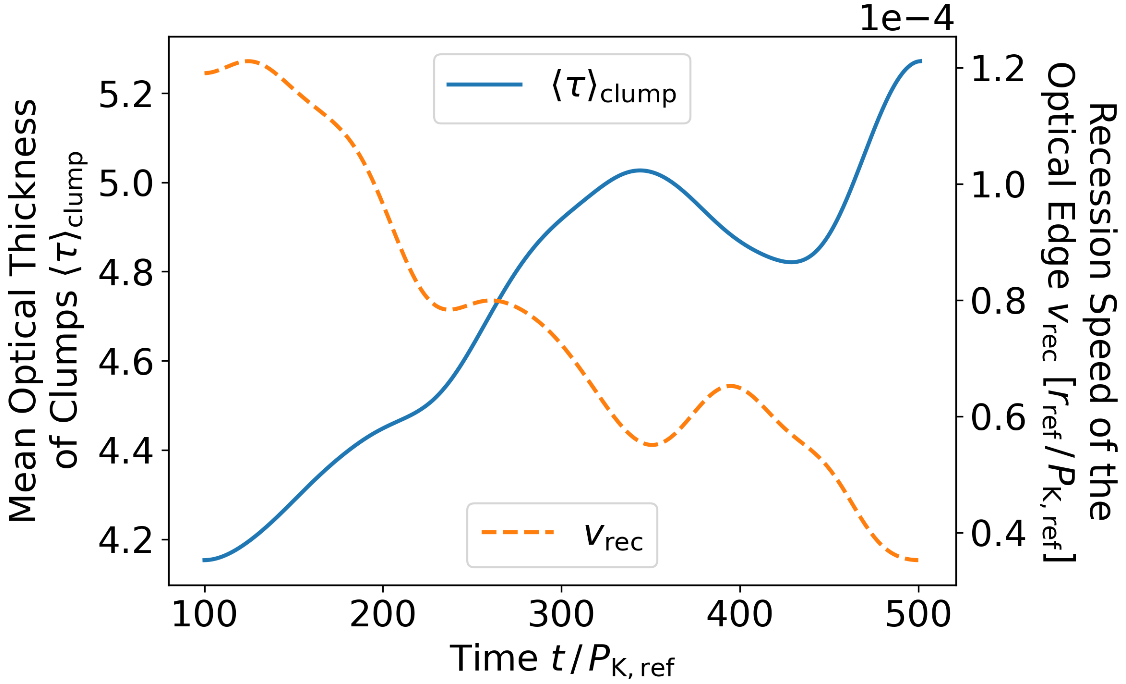

Figure 2.6: Time evolution of the mean optical thickness of clumps and the recession speed of the optical edge in the fiducial model. Both curves are convolved with a $\sigma_t = 20P_{\rm K,ref}$ Gaussian kernel to reduce noise.

Table 2.1: The parameter space for studying the concentration timescale

β	1.0×10^{-2}	1.0×10^{-1}	1.0×10^{0}	1.0×10^{1}
$\mathrm{St}_{\rm ref}$	1.0×10^{-5}	1.0×10^{-4}	1.0×10^{-3}	1.0×10^{-2}
$\Sigma_{\rm d0}$	2.6×10^{-3}	7.7×10^{-3}	2.5×10^{-2}	7.7×10^{-2}

NOTE — We investigate all combinations of the listed values, such that there are 64 cases shown in each panel of Figure 2.5. The unit of $\Sigma_{\rm d0}$ is g/cm^2.

Here is how we identify clumps from our models: Given a τ map at a specific time, we first calculate the optical thickness $\mathrm{d}\tau$ of each grid cell. We then seek locations where $\mathrm{d}\tau$ has a local maximum in the surrounding 3×3 grid and is also greater than a threshold value $\mathrm{d}\tau_{\rm th1}$. In this way, we sample the overdensities in the disk and rule out false positives due to the Poisson noise. However, this is not sufficient as it also samples the non-isolated overdensities (e.g., the dust wall). So, we then measure the ambient value of $\mathrm{d}\tau$ around each sampled local maximum by adding up the $\mathrm{d}\tau$ value in the outer rim of the 5×5 grid (16 grid cells), and rule out the ones that have an ambient value larger than another threshold value $\mathrm{d}\tau_{\rm th2}$. Through trial and error, we

Table 2.2: The mean optical thickness of clumps with different physical parameters

β	$\mathrm{St}_{\mathrm{ref}}$	Σ_{d0}	t_{con}	$\langle\tau\rangle_{\mathrm{clump}}$
20	1.0×10^{-4}	7.7×10^{-3}	$3.43\ P_{\mathrm{K,ref}}$	3.93
10	1.0×10^{-4}	7.7×10^{-3}	$6.85\ P_{\mathrm{K,ref}}$	3.73
5	1.0×10^{-4}	7.7×10^{-3}	$13.7\ P_{\mathrm{K,ref}}$	2.78
2.5	1.0×10^{-4}	7.7×10^{-3}	$27.4\ P_{\mathrm{K,ref}}$	2.39
10	4.0×10^{-4}	7.7×10^{-3}	$1.71\ P_{\mathrm{K,ref}}$	4.13
10	2.0×10^{-4}	7.7×10^{-3}	$3.43\ P_{\mathrm{K,ref}}$	3.86
10	1.0×10^{-4}	7.7×10^{-3}	$6.85\ P_{\mathrm{K,ref}}$	3.73
10	5.0×10^{-5}	7.7×10^{-3}	$13.7\ P_{\mathrm{K,ref}}$	3.49
10	2.5×10^{-5}	7.7×10^{-3}	$27.4\ P_{\mathrm{K,ref}}$	3.14
10	1.0×10^{-4}	7.7×10^{-2}	$3.82\ P_{\mathrm{K,ref}}$	4.09
10	1.0×10^{-4}	2.5×10^{-2}	$5.18\ P_{\mathrm{K,ref}}$	4.20
10	1.0×10^{-4}	7.7×10^{-3}	$6.85\ P_{\mathrm{K,ref}}$	3.73
10	1.0×10^{-4}	2.6×10^{-3}	$9.32\ P_{\mathrm{K,ref}}$	2.78

NOTE — The $\langle\tau\rangle_{\mathrm{clump}}$ values are measured at $t = 10t_{\mathrm{con}}$ in all cases. The $\langle\tau\rangle_{\mathrm{clump}}(t)$ functions are convolved with a $\sigma_t = t_{\mathrm{con}}$ Gaussian kernel to reduce noise. Σ_{d0} is in the unit of g/cm^2.

find $\mathrm{d}\tau_{\mathrm{th1}} = 0.5$ and $\mathrm{d}\tau_{\mathrm{th2}} = 0.1$ are reasonable threshold values.

Not surprisingly, we find that clumps are optically thick. Their mean optical depth ranges between roughly 2 and 4 at $t = 10\ t_{\mathrm{con}}$ (Table 2.2). This value is not steady in time — generally, clumps become more optically thick as time passes. This is likely because the dust wall (which fragments to form clumps) is becoming more massive over time, with grains piling onto it from the inner disk pushed by radiation pressure, and the outer disk driven by inward dust drift. The fact that the dust wall is increasing in mass can also be seen indirectly in Figure 2.6, where it shows that the motion of the dust wall is gradually slowing down as radiation pressure is blocked by more and more dust mass.

Table 2.2 also shows that $\langle\tau\rangle_{\mathrm{clump}}$ is positively correlated to both β and $\mathrm{St}_{\mathrm{ref}}$. This is in line with our expectations since clump formation is the outcome of the instability, which can be enhanced by stronger radiation pressure and suppressed by stronger gas drag. Therefore, higher β and $\mathrm{St}_{\mathrm{ref}}$ values should make the disk more susceptible to the clumping effect. Meanwhile, we find a rough positive correlation between $\langle\tau\rangle_{\mathrm{clump}}$ and Σ_{d0}. To understand this further, Figure 2.7 shows the morphology of disk edges when Σ_{d0} varies. We find that lower Σ_{d0} models have more clumps spread over a

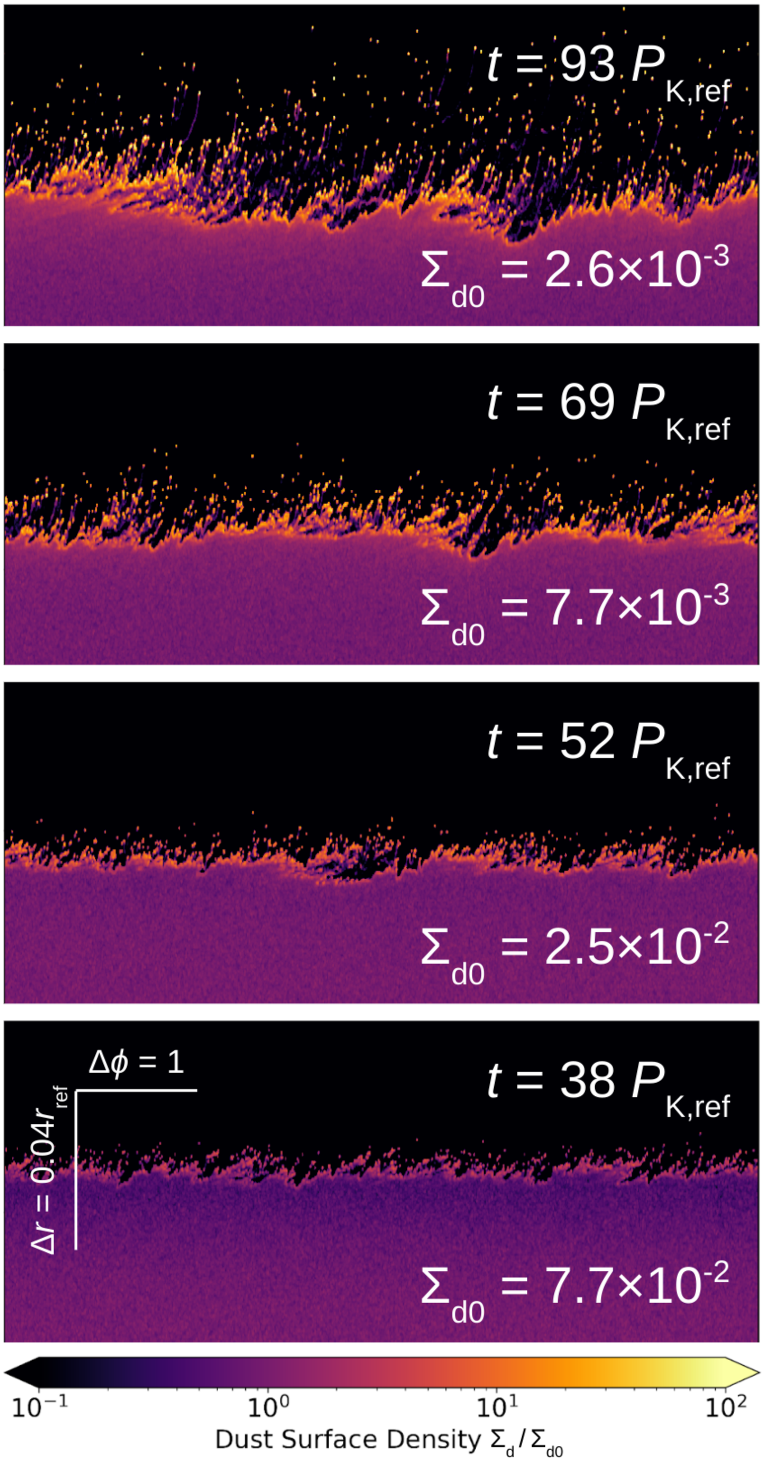

Figure 2.7: Comparison of disk edges showing the effect of the disk mass. Snapshots are taken at $t = 10t_{\mathrm{con}}$ in models with $\beta = 10$, $\mathrm{St}_{\mathrm{ref}} = 10^{-4}$, but different Σ_{d0}. Σ_{d0} is in the unit of $\mathrm{g/cm^2}$.

Table 2.3: The mean optical thickness of clumps with different numerical parameters

$N_{\rm par}$	N_r	N_ϕ	$t_{\rm con}$	$\langle\tau\rangle_{\rm clump}$
1.0×10^8	1024	1024	$6.85\ P_{\rm K,ref}$	3.66
3.3×10^7	1024	1024	$6.85\ P_{\rm K,ref}$	3.60
1.0×10^7	1024	1024	$6.85\ P_{\rm K,ref}$	3.73
3.3×10^6	1024	1024	$6.85\ P_{\rm K,ref}$	3.54
1.0×10^6	1024	1024	$6.85\ P_{\rm K,ref}$	3.65
2.0×10^7	2048	1024	$6.85\ P_{\rm K,ref}$	3.86
1.0×10^7	1024	1024	$6.85\ P_{\rm K,ref}$	3.73
5.0×10^6	512	1024	$6.85\ P_{\rm K,ref}$	3.21
2.5×10^6	256	1024	$6.85\ P_{\rm K,ref}$	2.55
2.0×10^7	1024	2048	$6.85\ P_{\rm K,ref}$	3.44
1.0×10^7	1024	1024	$6.85\ P_{\rm K,ref}$	3.73
5.0×10^6	1024	512	$6.85\ P_{\rm K,ref}$	3.94
2.5×10^6	1024	256	$6.85\ P_{\rm K,ref}$	4.02

NOTE — The $\langle\tau\rangle_{\rm clump}$ values are measured at $t = 10t_{\rm con}$ in all cases. The $\langle\tau\rangle_{\rm clump}(t)$ functions are convolved with a $\sigma_t = t_{\rm con}$ Gaussian kernel to reduce noise.

wider radial extent, although the clumps are less dense. Since our density profiles are fixed, the same amount of dust is distributed over a wider radial range in lower $\Sigma_{\rm d0}$ models, at least initially. We, therefore, speculate that they favor forming smaller clumps because there is a stronger Keplerian shear to overcome in order to form massive clumps.

Finally, to check that our results are not sensitive to numerics, we measure $\langle\tau\rangle_{\rm clump}$ with different super-particle, radial, and azimuthal resolutions at $t = 10\ t_{\rm con}$. The results are shown in Table 2.3. We find good convergence of $\langle\tau\rangle_{\rm clump}$ with different values of $N_{\rm par}$ and N_r. For N_ϕ, we reiterate that clumps are eroded (and eventually destroyed) when grains move away from the clump body by one azimuthal grid cell; thus, lower azimuthal resolutions naturally make it harder for dust grains to leave the clump body, explaining why $\langle\tau\rangle_{\rm clump}$ increases when N_ϕ decreases in Table 2.3. As N_ϕ increases, clumps simply shrink with cell size due to the CIC prescription; it may not be possible to obtain good convergence with respect to N_ϕ unless additional physics, such as some diffusive effects, is included to set a limit to how small clumps can be.

2.2.4 Recession of the Disk Edge

Going back to Figure 2.3, we notice that the radius of the fragmented disk edge (left) is noticeably larger than the axisymmetric edge (right), even though they use the same initialization. This illustrates another result of the instability, which is that it causes the disk edge to recede, even after the formation of a sharp dust wall.

The disk edge recedes because radiation leaks through the regions of underdensity at the asymmetric disk edge, exposing the previously shaded disk materials to stronger radiation pressure, and pushing them to higher orbits. This is shown in Figure 2.8, where we find multiple *leaking points* in the extinction map. Since the leaking points can move azimuthally relative to the disk edge due to the orbital shear, the entire disk is exposed to stronger radiation levels in a time-averaged sense compared with the axisymmetric case in Figure 2.3. This qualitative description is equivalent to the decrease of the overall disk optical depth due to clumping effects (see Figure 2.4). Moreover, we note that when the disk edge recedes, the dust density decreases following the geometric factor r^2, which leads to a further reduction of the optical depth and promotes recession as positive feedback.

However, this recession is not guaranteed to last forever. Whether it can be sustained depends on whether it can overcome the inward drift of dust. Dust grains naturally drift inward because the sub-Keplerian rotation of the background gas exerts a headwind on them, gradually removing their angular momentum. As dust grains drift in, they add to the optical depth of the inner edge, making it heavier and heavier for radiation pressure to push. This competes with the effects that reduce optical depth. If $\langle \tau' \rangle$ increases with time, we expect the edge will eventually stop receding and start to drift inward. We, in fact, do observe this *turnover* in some of our models with $\mathrm{St}_{\mathrm{ref}} = 10^{-2}$. A similar turnover is also seen in previous 1D studies (e.g., Dominik and Dullemond 2011); 1D treatment cannot capture clumping and so the turnover becomes inevitable in those models. We will discuss the turnover further in Section 2.3.1. Otherwise, if $\langle \tau' \rangle$ decreases with time (e.g., the upper panel of Figure 2.4), the recession may be sustained.

In the rest of this section, we identify receding disks in our parameter space and investigate how β, $\mathrm{St}_{\mathrm{ref}}$, and Σ_{d0} affect their recession speeds. The migration of disk edges is shown in Figure 2.9. We then compute the recession speed of the optical edge v_{rec} by averaging between $t = 10 t_{\mathrm{con}}$ and $t = 15 t_{\mathrm{con}}$ for each model. The results are shown in Table 2.4.

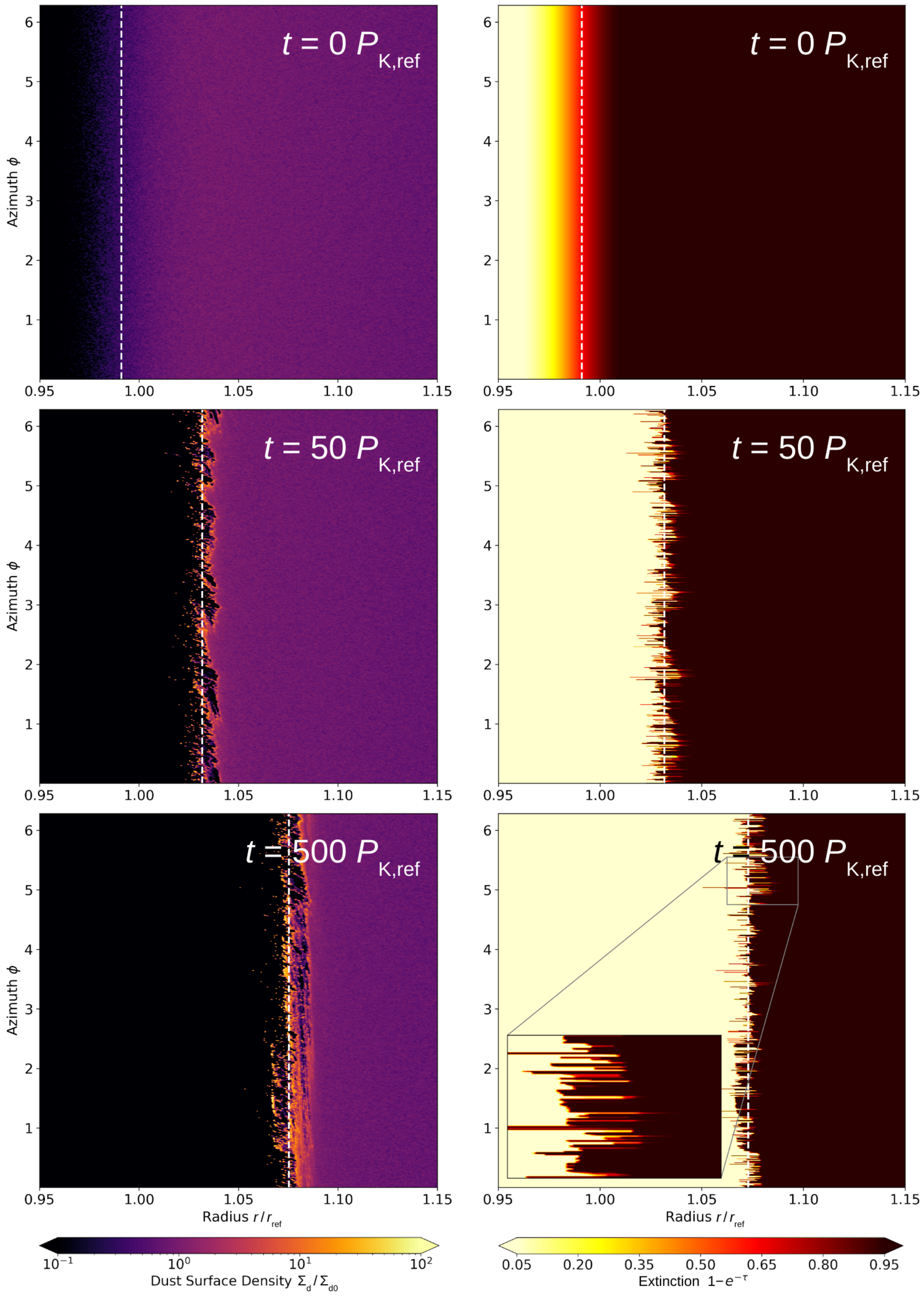

Figure 2.8: Time evolution of the dust surface density and the extinction in the fiducial model. Snapshots of the dust surface density $\Sigma_{\rm d0}$ (*left*) and the extinction $1-e^{-\tau}$ (*right*) are taken at $t = 5P_{\rm K,ref}$ (*upper*), $t = 50P_{\rm K,ref}$ (*middle*), and $t = 500P_{\rm K,ref}$ (*lower*). The dashed line marks the optical edge (where $\langle \tau' \rangle = 1$), separating the optically thin and optically thick regions.

Table 2.4: Recession speed of the optical edge with different physical parameters

β		20	**10**	5	2.5
$v_{\rm rec}$ $[10^{-5} r_{\rm ref}\Omega_{\rm K,ref}]$		5.92	**3.06**	1.31	0.75
$\rm St_{ref}$ $[\times 10^{-4}]$	4.0	2.0	**1.0**	0.5	0.25
$v_{\rm rec}$ $[10^{-5} r_{\rm ref}\Omega_{\rm K,ref}]$	9.85	5.77	**3.06**	1.48	0.75
$\Sigma_{\rm d0}$ $[\times 10^{-3}\,{\rm g/cm^2}]$		2.6	**7.7**	25	77
$v_{\rm rec}$ $[10^{-5} r_{\rm ref}\Omega_{\rm K,ref}]$		5.33	**3.06**	1.76	1.65

NOTE — Values of the recession speed $v_{\rm rec}$ are averaged between $t = 10t_{\rm con}$ and $t = 15t_{\rm con}$ for each model. The fiducial parameters and results are bold-marked.

Our results show that $v_{\rm rec}$ is typically on the order of $10^{-5}\, r_{\rm ref}\Omega_{\rm K,ref}$, which is considerably fast. Assuming $r_{\rm ref} = 1$ au, it could result in a cavity that is a few tens of astronomical units wide in 1 Myr if it can overcome the accretion flow of the disk. The accretion velocity $v_{\rm acc}$ in a viscous disk model is

$$v_{\rm acc} = -\frac{3\nu}{2r_{\rm ref}}, \tag{2.18}$$

where ν is the kinematics viscosity. Assuming a constant $\nu = 10^{-6}\, r_{\rm ref}^2\Omega_{\rm K,ref}$, which is equivalent to $\alpha = 4\times 10^{-4}$ at $r_{\rm ref}$ (Shakura and Sunyaev 1973), we have $v_{\rm acc} = -1.5\times 10^{-6}\, r_{\rm ref}\Omega_{\rm K,ref}$. It is certainly within the realms of possibility that this recession of dust can resist and overcome the accretion flow.

If the typical order of the recession rate in Table 2.4 can be sustained over the disk lifetime, we can write

$$\frac{{\rm d}r}{{\rm d}t} = 10^{-5}\sqrt{\frac{GM_\star}{r}}, \tag{2.19}$$

where r is the location of the disk edge. Given $M_\star = M_\odot$, and a disk age of $\sim 10^6$ years, we can integrate the above equation and find that $r \approx 20$ au in the end, even if r is negligibly small at first.

We expect stronger radiation pressure (higher β) and weaker gas drag (higher $\rm St_{ref}$) to produce higher $v_{\rm rec}$. The parameter survey shows that $v_{\rm rec}$ is positively correlated to β and $\rm St_{ref}$ as expected. And the correlations are almost proportional, consistent with the terminal velocity scenario (see Appendix A.1). We find $v_{\rm rec}$ increases when $\Sigma_{\rm d0}$ decreases since higher $\Sigma_{\rm d0}$ values naturally make the disk edge heavier for

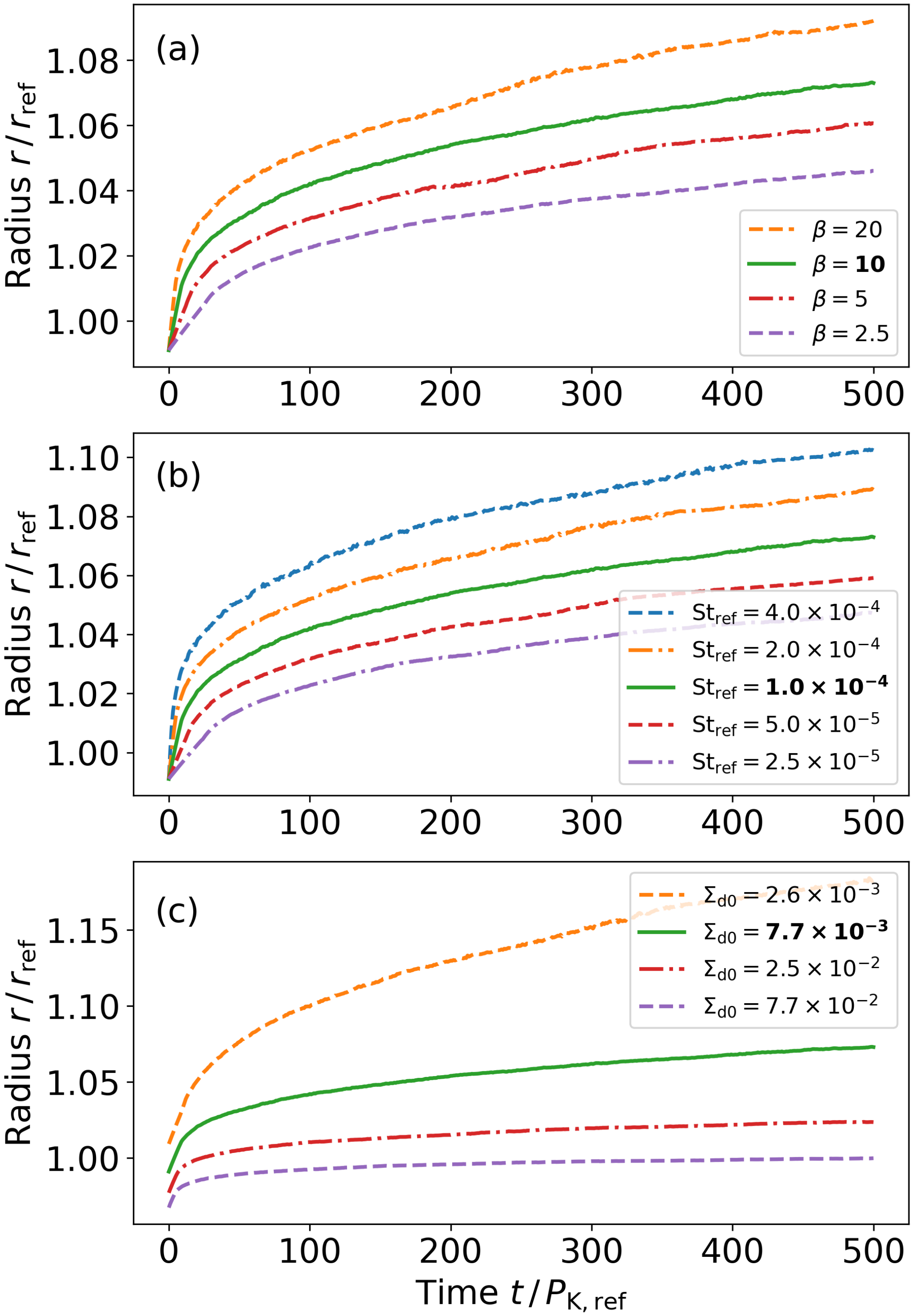

Figure 2.9: Time evolution of the optical edge with different physical parameters. (a): Models with different β. **(b):** Models with different $\mathrm{St_{ref}}$. **(c):** Models with different Σ_d0. Σ_d0 is in the unit of $\mathrm{g/cm^2}$. The fiducial parameters are bold-marked in the legend.

radiation pressure to push outward. Moreover, we find the correlation between $v_{\rm rec}$ and $\Sigma_{\rm d0}$ follows $v_{\rm rec} \propto \Sigma_{\rm d0}^{-0.5}$ when $\Sigma_{\rm d0}$ is not too high (e.g., $\Sigma_{\rm d0} \leq 2.5 \times 10^{-2}$ g/cm^2). Whether this is a coincidence or there is physics behind it will be explored in future studies.

2.3 Discussion

2.3.1 The Turnover of the Recession

The recession of the disk edge may be eventually overcome by a constant influx of dust grains adding to the optical depth of the inner dust wall (see Section 2.2.4), similar to the disk evolution described in Dominik and Dullemond (2011). In this case, the instability and clump formation at the disk edge can only delay the turnover but not avoid it. Here, we discuss the possible conditions for this turnover to occur.

The motion of dust grains at terminal velocity is described in Appendix A.1 (also see Takeuchi and Artymowicz (2001)). The radial terminal velocity is given as

$$W_{\rm r,term} = \frac{\rm St}{1 + {\rm St}^2}(\beta e^{-\tau} - \eta). \tag{2.20}$$

Even though β is likely orders of magnitude larger than η for micron-sized grains, the above equation shows that inward drift would still occur when $\tau > \ln(\beta/\eta)$. In a simple picture, a constant stream of micron-sized grains flows toward the inner edge from the optically thick portion of the disk, forcing τ at the inner edge to increase without bound. This is what would ultimately lead to a turnover of the recession.

In reality, not all of the dust grains are fated to end up concentrated at disk edges. They are likely to go through a turbulent evolutionary path, colliding, coagulating, and fragmenting, as they migrate through the disk (e.g., Laibe et al. 2008; Birnstiel et al. 2012; Krijt et al. 2016; Schoonenberg et al. 2018). Some grains may never reach the inner edge if grain growth is sufficiently fast to turn them into bodies that are not sensitive to aerodynamic effects (e.g., Okuzumi et al. 2012; Garcia and Gonzalez 2020). Even at the edge itself, opacity should evolve over time as grain size evolves. Clumps found in our models should accelerate grain size evolution by having higher dust concentration and, hence, higher collision rates. Considering these complications, it is not clear if τ at the inner edge should always be increasing. If grain growth is able to reduce τ more rapidly than the addition of small grains through inward drift, we might expect disk recession to continue without a turnover. This clearly demands more sophisticated models than the basic ones presented here, and so whether a turnover might occur, or how long would disk recession last, are questions for future studies.

2.3.2 Multi-size Dust Models and Collisions

We have assumed a single grain size in our proof-of-concept models. Including a distribution of grain sizes is a natural next step, but it would lead to unrealistic results without also considering grain collisions. Revisiting Equation 2.20, we note that if $\beta < \eta$ for a given grain size, those grains will always drift inward regardless of the value of τ. For our fiducial parameters, this size is on the order of a millimeter. Assuming a grain size distribution of $\mathrm{d}n_\mathrm{s} \propto s^{-3.5}\,\mathrm{d}s$ (Mathis et al. 1977), the optical depth contribution from mm-sized grains is $\sim$3% of that from μm-sized grains. This is a small but significant contribution. Without considering collisions, mm-sized grains would drift past the inner dust wall like ghosts, and shield the entire disk from radiation pressure.

In reality, these larger grains will collide with the inner dust wall. Such collisions tend to favor mass transfer from larger bodies to smaller ones (Hasegawa et al. 2021), which may lead to a net reduction in the local opacity of the disk material, potentially accelerating the disk recession. Collision, once again, likely plays a critical role.

2.3.3 Turbulence

Gas turbulence is another piece of physics that we have not included in our models. In protoplanetary disks, turbulence is often treated as a diffusive or mixing process. Taking this interpretation at face value, turbulence would hamper the generation of dust clumps by diffusing the sharp inner dust wall. However, turbulence is only diffusive on a large scale; on a smaller scale, such as within the thickness of the inner dust wall, turbulence is likely better described as a stochastic perturbation, which makes the wall thinner at some azimuth and thicker elsewhere. In this picture, turbulence may, in fact, seed the density perturbation that leads to clump formation.

Turbulence can also promote grain collisions and facilitate grain size evolution. In our single-size models, the grains are typically so tightly coupled to the gas that, even if there is turbulence, they are unlikely to collide with each other, allowing us to safely ignore this effect. The same cannot be said for models with a distribution of grain sizes. Echoing the previous sections, turbulence, grain collision, and grain size evolution are tightly connected, and may all play important roles in the long-term evolution of the inner disk edge and dust clumps.

2.3.4 Outlooks

Dust clumps, in general, are of interest to the topic of planet formation. For instance, self-gravitationally collapsed dust clumps could potentially form planetesimals (e.g., Johansen et al. 2007; Simon et al. 2016). The clump formation observed in this work may interact with other clump formation mechanisms, such as streaming instability (e.g., Youdin and Goodman 2005; Youdin and Johansen 2007; Johansen and Youdin 2007; Jacquet et al. 2011), coagulation instability (Tominaga et al. 2021), and some mesoscale instability triggered by the dust feedback in dust rings (Huang et al. 2020). If our clumps do tend to coagulate, a receding disk edge could leave behind a trail of planetesimals, creating an ideal breeding ground for close-in super-Earths.

How the instability described in this work may operate in a 3D dust disk is another aspect worth investigating. In 2D, the disk is shielded from radiation pressure behind an inner dust wall. But in a flared 3D disk, the wall becomes a shell that envelopes the disk surface. Will there be clumps on the optical surface? How massive can those clumps be? If the dynamics become significantly different from what we have seen in 2D, how will the disk surface react to radiation pressure? These are all important questions to be answered in future studies.

2.4 Conclusion

In this chapter, we demonstrate a possible mechanism to explain the dust-cleared cavity of transitional disks. We perform simplified, proof-of-concept simulations of dusty disks to show that the inner edge of a dust disk is susceptible to a new irradiation instability that amplifies azimuthal asymmetry. We show that:

- Dust clumps, which are isolated density features, can form out of the azimuthal density perturbations at the inner cavity edge of the disk.
- The clumps make the inner disk edge asymmetric, reduce the effective optical depth of the disk and lead to rapid outward recession of the disk edge.

When the transition of the optical depth is sufficiently sharp at the inner cavity edge of the disk, azimuthal density perturbations can be amplified by the combined effect of radiation pressure, shadowing, and orbital shear to form clumps (Section 2.2.1, Figure 2.2). Without internal forces, the clumps in our model are susceptible to destruction due to orbital shear (Section 2.2.2). The balance between clump formation and destruction maintains a stabilized sharpness of the optical depth transition at the disk edge (Figure 2.4).

The clumps are typically more optically thick than their surroundings (Section 2.2.3). The average density of clumps (equivalent to their averaged optical thickness $\langle\tau\rangle_{\rm clump}$) generally increases with time (Figure 2.6). The clumps are denser when radiation pressure is stronger (higher β), when dust grains are less (but still) coupled to the gas (higher $\mathrm{St}_{\rm ref}$), and when the disk has more dust (higher $\Sigma_{\rm d0}$; Table 2.2).

While the clumps can block radiation at specific azimuths, light can leak at other positions and push disk material outward relative to the clumps (Figure 2.8). Quantitatively, this can be seen as the clumping effect reducing the effective optical depth of the disk (Figure 2.4), which can lead to the disk edge recession (Section 2.2.4). In our fiducial model, the recession speed is on the order of $10^{-5} r_{\rm ref}/P_{\rm K,ref}$, which is sufficiently fast to overcome viscous accretion, if we assume a conventional viscosity of $\alpha = 4 \times 10^{-4}$. Stronger radiation pressure levels (higher β), weaker dust-gas coupling (higher $\mathrm{St}_{\rm ref}$), and lower surface densities (lower $\Sigma_{\rm d0}$) are in favor of faster recession (Table 2.4).

Chapter 3

In the Post-Planet-Formation Era: Dust Dynamics under Planet-Disk Interactions at Pressure Bumps

This chapter is organized as follows: We describe the disk-planet system of interest and different numerical models in Section 3.1. We present our results in Section 3.2, which includes three parts: The first part shows the widening effect of dust rings due to planet-related effects. The second part shows the combined effect of the planet and different levels of dust back-reaction on dust rings. The third part provides an analytical approach to estimate the dust ring width. In Section 3.3 we discuss the connection between dust diffusivity and gas turbulent viscosity under planet-related effects. Finally, we conclude in Section 3.4.

3.1 Planet-Disk Model

We consider a 3D protoplanetary disk composed of gas and dust with an embedded planet of mass $M_{\rm p}$ around a central star of mass $M_\star$. We neglect disk self-gravity, magnetic fields, planet orbital migration, and planet accretion. We use $\{r, \phi, \theta\}$ to denote spherical radius, azimuth, and polar angle, and $\{R, \phi, Z\}$ to denote cylindrical radius, azimuth, and height. Both coordinates are centered on the star.

In the following sections, the subscript "ref" denotes azimuthally averaged values at $R = R_{\rm ref}$ on the disk midplane, where $R_{\rm ref}$ is a reference radius. The subscript "0" is only used for time-varying quantities, and it denotes their initial values. The symbol $\langle\rangle$ denotes azimuthally averaged values.

3.1.1 Basic Equations and Numerical Setups

The volumetric density, pressure, and velocity of gas are denoted by $\{\rho_{\rm g}, P, \boldsymbol{V}\}$. The time-independent, vertically isothermal, axisymmetric gas temperature and sound speed are given by $T(R) = T_{\rm ref}(R/R_{\rm ref})^{-q}$ and $c_{\rm s}(R) = c_{\rm s,ref}(R/R_{\rm ref})^{-q/2}$. The isothermal equation of state and the pressure scale-height are given by $P = \rho_{\rm g} c_{\rm s}^2$ and $H_{\rm g} = c_{\rm s}/\Omega_{\rm K}$, where $\Omega_{\rm K}(R) = \sqrt{GM_\star/R^3}$ is the Keplerian angular velocity and G is the gravitational constant. The disk is assumed to be nonflared with a constant aspect ratio $h = H_{\rm g}/R = 0.05$, corresponding to $q = 1$.

We consider a single species of dust modeled as a pressureless fluid with volumetric density and velocity $\{\rho_{\rm d}, \boldsymbol{W}\}$. The Epstein gas drag on the dust is parameterized by the Stokes number $\mathrm{St} = \tau_{\rm s}\Omega_{\rm K}$, where

$$\tau_{\rm s} = \frac{\rho_{\rm g,norm}}{\rho_{\rm g}} \frac{c_{\rm s,ref}}{c_{\rm s}} \frac{\mathrm{St}_{0,\rm ref}}{\Omega_{\rm K,ref}} \tag{3.1}$$

is the particle stopping time. $\rho_{\rm g,norm}$ is a normalization that equals to $\rho_{\rm g0,ref}$ in type A models (see Section 3.1.2).

The hydrodynamic equations for gas and dust are given by

$$\frac{\partial \rho_{\rm g}}{\partial t} + \nabla \cdot (\rho_{\rm g} \boldsymbol{V}) = 0, \tag{3.2}$$

$$\begin{aligned} \frac{\partial \boldsymbol{V}}{\partial t} + \boldsymbol{V} \cdot \nabla \boldsymbol{V} = &- \frac{1}{\rho_{\rm g}} \nabla P - \nabla \Phi \\ &+ \frac{\epsilon_\rho}{\tau_{\rm s}} (\boldsymbol{W} - \boldsymbol{V}) + \frac{1}{\rho_{\rm g}} \nabla \cdot \mathcal{T}, \end{aligned} \tag{3.3}$$

$$\frac{\partial \rho_{\rm d}}{\partial t} + \nabla \cdot (\rho_{\rm d} \boldsymbol{W}) = 0, \tag{3.4}$$

$$\frac{\partial \boldsymbol{W}}{\partial t} + \boldsymbol{W} \cdot \nabla \boldsymbol{W} = -\nabla \Phi - \frac{1}{\tau_{\rm s}} (\boldsymbol{W} - \boldsymbol{V}). \tag{3.5}$$

Here, $\Phi = -GM_\star/r + \Phi_{\rm p} + \Phi_{\rm ind}$ is the net gravitational potential composed of terms from the star, the planet, and the indirect planet-star gravitational interactions, respectively. $\Phi_{\rm ind}$ is added to account for the effect of stellar motion on the disk due to the asymmetric planet-star gravitational field. The disk-related potential terms are neglected for the non-selfgravitating disk. $\epsilon_\rho = \rho_{\rm d}/\rho_{\rm g}$ is the *local* dust-to-gas ratio, which should be distinguished from the vertically integrated *global* dust-to-gas ratio $\epsilon_\Sigma = \Sigma_{\rm d}/\Sigma_{\rm g}$. $\mathcal{T}$ is the viscous stress tensor (see Equation 11 in (Bi et al. 2021)) which involves a gas kinematic viscosity ν. We implement $\nu = 10^{-5} R_{\rm ref}^2 \Omega_{\rm K,ref}$ to suppress interference such as vertical shear instability (Nelson et al. 2013) and vortex formation (Koller et al. 2003; Li et al. 2005, 2009; Lin and Papaloizou 2010) at gap edges. To isolate planet-related effects on the dust ring, turbulent-induced dust diffusion (Weber et al. 2019) is neglected. Unless otherwise specified, dust back-reaction on the gas is included.

We consider a planet on a fixed, circular orbit at $R = R_{\rm ref}$ on the disk midplane. The planet-related potential terms are

$$\Phi_{\rm p} + \Phi_{\rm ind} = -\frac{G m_{\rm p}(t)}{\sqrt{r'^2 + r_{\rm s}^2}} + \frac{G m_{\rm p}(t)}{R_{\rm ref}^2} R \cos\left(\phi - \phi_{\rm p}\right), \tag{3.6}$$

where $\phi_{\rm p}$ is the azimuth of the planet, $r_{\rm s} = 0.1 H_{\rm g}$ is a smoothing length, and r' is the distance to the planet. Here, we define a time-dependent planet mass $m_{\rm p}(t)$, with its value increasing gradually from zero to $M_{\rm p}$ (see Equation 14 in (Bi et al. 2021)) at the start of simulations to avoid transient impacts of adding a full-mass planet to the disk. The planet's potential is turned on over a timescale of $t_{\rm g} = 500 P_{\rm K,ref}$, where $P_{\rm K,ref} = 2\pi\Omega_{\rm K,ref}^{-1}$ is the reference orbital period.

Our models are evolved by the FARGO3D code (Benítez-Llambay and Masset 2016; Benítez-Llambay et al. 2019). We adopt a spherical domain centered on the star with $r \in [0.2, 4.0] R_{\rm ref}$, $\phi \in [0, 2\pi]$, and polar angle such that $\tan(\pi/2 - \theta) \in [-3h, 3h]$. The resolutions we choose are $N_r \times N_\theta \times N_\phi = 360 \times 90 \times 720$, with logarithmic spacing in r and uniform spacing in θ and ϕ.

The gas density is damped to its initial value at radial boundaries and is assumed to be in vertical hydrostatic equilibrium at vertical boundaries. The dust density is symmetric at both radial and vertical boundaries. The meridional velocities of gas and dust are set to zero at radial and vertical boundaries, except that the inner radial boundary is open for mass loss of dust. The azimuthal velocities at those boundaries are assigned at the Keplerian speed with a pressure offset for gas. Periodic boundaries are imposed in the ϕ direction.

3.1.2 Models

The models in our paper are categorized into three types, namely type A, B, and C. The three types differ in the prescription of gas evolution and initial conditions. In type A models, the initial radial profile of dust surface density $\Sigma_{\rm d0}$ is a power-law function, whereas in type B and C models $\Sigma_{\rm d0}$ is a Gaussian radial bump. Different from that in type B models, the evolution of $\{\rho_{\rm g}, \boldsymbol{V}\}$ is artificially stalled in C, which means they are time-invariant.

Type A Models: How will $M_{\rm p}$ and St affect the widening effect?

Type A models are used to *quantitatively* study how planet-related effects would change the radial width of dust rings at the outer gap edge. The corresponding results are shown in Sections 3.2.3 and 3.3. There are 12 type A models with different planet masses $M_{\rm p}$ ranging from $2\times10^{-4}M_\star$ to $7\times10^{-4}M_\star$, and two initial reference Stokes numbers $\mathrm{St}_{0,\rm ref} = 10^{-3}$ and 10^{-2}. Here, we define the model with $\{M_{\rm p}, \mathrm{St}_{0,\rm ref}\} = \{3\times10^{-4}M_\star, 10^{-3}\}$ as the fiducial model, representing a Saturn-mass planet around a solar-mass star, with 0.1-mm-sized grains at $\sim$ 45 au in a young protoplanetary disk such as HL Tau[1].

The initialization of gas and dust in type A models are the same as those in Bi et al. (2021). The axisymmetric gas density profile is initialized to

$$\rho_{\rm g0} = \rho_{\rm g0,ref}\left(\frac{R}{R_{\rm ref}}\right)^{-p}\times\exp\left[\frac{GM_\star}{c_{\rm s}^2}\left(\frac{1}{r}-\frac{1}{R}\right)\right], \tag{3.7}$$

with $p = 1.5$ and $\rho_{\rm g0,ref}$ being arbitrary for a non-selfgravitating disk. The dust density is initialized to

$$\rho_{\rm d0} = \left(\epsilon_{\rho0}\rho_{\rm g0}\right)\Big|_{Z=0}\times\exp\left(-\frac{Z^2}{2H_\epsilon^2}\right), \tag{3.8}$$

where $\epsilon_{\rho0}|_{Z=0} = 0.1$ and $H_\epsilon = H_{\rm g}H_{\rm d}(H_{\rm g}^2 - H_{\rm d}^2)^{-1/2}$ is valued such that the dust scale-height $H_{\rm d0} = 0.1H_{\rm g}$ and $\epsilon_{\Sigma0} = 0.01$. The azimuthal velocities are initialized to

$$V_{\phi0} = R\Omega_{\rm K}\left(\sqrt{1-2\eta} + \frac{\epsilon_{\rho0}\eta}{\epsilon_{\rho0}+1}\frac{1}{\mathrm{St}'^2+1}\right) \tag{3.9}$$

$$W_{\phi0} = \sqrt{\frac{GM_\star}{r}} - R\Omega_{\rm K}\left(\frac{\eta}{\epsilon_{\rho0}+1}\frac{1}{\mathrm{St}'^2+1}\right), \tag{3.10}$$

where $\mathrm{St}' = \mathrm{St}/(1+\epsilon_\rho)$, and $2\eta = (p+q)h^2 + q(1-R/r)$ is a dimensionless measurement

---

[1] Here we assume that the grain internal density is 1.5 g/cm^3, the total disk mass is 0.2 $M_\odot$ (Booth and Ilee 2020), the outer disk radius is 150 au, and the surface density power-law index is -1.5.

of the radial pressure gradient. The radial velocities are initialized to

$$V_{R0} = \frac{2\epsilon_{\rho 0}\eta}{\epsilon_{\rho 0}+1}\frac{\mathrm{St}'}{\mathrm{St}'^2+1}R\Omega_\mathrm{K} \tag{3.11}$$

$$W_{R0} = -\frac{2\eta}{\epsilon_{\rho 0}+1}\frac{\mathrm{St}'}{\mathrm{St}'^2+1}R\Omega_\mathrm{K}. \tag{3.12}$$

And the initial vertical velocities are $V_{Z0} = W_{Z0} = 0$.

Type B Models: How will dust back-reaction affect the widening effect?

Type B models are used to *qualitatively* study the effect of different levels of dust back-reaction on the dust ring width. The corresponding results are shown in Section 3.2.2 and Figure 3.2. The models include a gas gap already opened by a planet, as well as a Gaussian dust ring at the outer gap edge. There are 5 type B models, namely B1 to B5, with different levels of dust load in the dust ring.

To have a gas gap opened by the planet, the gas initialization $\{\rho_\mathrm{g0}, \boldsymbol{V}_0\}$ in all type B models are taken from the snapshot at $t = 3000P_\mathrm{K,ref}$ in the fiducial type A model (i.e., $\{M_\mathrm{p}, \mathrm{St}_\mathrm{0,ref}\} = \{3\times10^{-4}M_\star, 10^{-3}\}$), in which the gap profile has almost reached an equilibrium state. Here, we set $t_\mathrm{g} = 0$ to maintain the initial gap profile, and consequently, the planet mass is fixed at $m_\mathrm{p} = 3\times10^{-4}M_\star$.

Dust grains in type B models have $\mathrm{St}_\mathrm{0,ref} = 10^{-3}$. The dust density is initialized to an axisymmetric Gaussian ring with

$$\rho_\mathrm{d0} = \frac{\Sigma_\mathrm{d0}}{\sqrt{2\pi}H_\mathrm{d0}} \times \exp\left[-\frac{(R-R_\mathrm{pmax})^2}{2w_\mathrm{d0}^2} - \frac{Z^2}{2H_\epsilon^2}\right], \tag{3.13}$$

where $H_\mathrm{d0} = 0.1H_\mathrm{g}$, $R_\mathrm{pmax} = 1.243R_\mathrm{ref}$ is the radius of the midplane pressure maximum, and $w_\mathrm{d0} = H_\mathrm{g,ref}$ is the initial radial width of the ring. Σ_d0 is valued such that $\epsilon_{\Sigma 0} = \{5\times10^{-4}, 5\times10^{-3}, 5\times10^{-2}, 5\times10^{-1}, 5\}$ at $R = R_\mathrm{pmax}$ in Model B1, B2, B3, B4, B5, respectively (see Table 3.1). We note that $\epsilon_{\Sigma 0}$ for Model B3 best reproduces the dust load level of the ring at $t = 3000P_\mathrm{K,ref}$ in the fiducial type A model. The dust velocities in all type B models are initialized to $W_{\phi 0} = \sqrt{GM_\star/r}$ and $W_{R0} = W_{Z0} = 0$.

Table 3.1: Dust Load Initialization of Type B Models

Model	$\epsilon_{\Sigma 0}^{\max}$
B1	0.0005
B2	0.005
B3	0.05
B4	0.5
B5	5

NOTE — $\epsilon_{\Sigma 0}^{\max}$ is the initial dust-to-gas surface density ratio at the radial peak of the dust ring. Except for the dust load, all the other dust and gas initial conditions are identical for all type B models.

Type C Models: Isolating the multiple effects caused by the planet

Type C models are used to *qualitatively* study how various planet-related effects would change the dust ring width. The corresponding results are shown in Section 3.2.1 and Figure 3.1. Like type B models, these models also include a Gaussian dust ring and a gas gap, but the further evolution of gas density and velocity is stalled to control variables.

There are five type C models to isolate planet-related effects, which are differentiated by the initialization of gas and whether planetary potential terms are included (see Table 3.2). The face-on views of gas initialization in Model C1 and C5 are provided in Appendix B.1 to visualize the differences. The initialization of dust in all type C models is identical to that in Model B3 (i.e., an axisymmetric Gaussian ring with $\epsilon_{\Sigma 0} = 0.05$ at $R = R_{\mathrm{pmax}}$ and $\mathrm{St}_{0,\mathrm{ref}} = 10^{-3}$). In Model C1, the prescription of the planet is identical to the one in type B models. To avoid errors while disabling gas evolution, the gas damping effect at boundaries and dust back-reaction on the gas are disabled as well.

Table 3.2: Gas Initialization of Type C Models

Model	$\rho_{\rm g}$	$V_{\rm R}$	V_ϕ	$V_{\rm Z}$	$\Phi_{\rm p}+\Phi_{\rm ind}$	Axisymmetry
C1	$\rho'_{\rm g}$	$V'_{\rm R}$	V'_ϕ	$V'_{\rm Z}$	Included	with density spirals with velocity spirals
C2	$\rho'_{\rm g}$	$V'_{\rm R}$	V'_ϕ	$V'_{\rm Z}$	Neglected	with density spirals with velocity spirals
C3	$\langle\rho'_{\rm g}\rangle$	$V'_{\rm R}$	V'_ϕ	$V'_{\rm Z}$	Neglected	without density spirals with velocity spirals
C4	$\rho'_{\rm g}$	0	$\sqrt{R^2\Omega_{\rm K}^2\left(1-\frac{3}{2}\frac{Z^2}{R^2}\right)+\frac{R}{\rho'_{\rm g}}\frac{\partial P'}{\partial R}}$	0	Neglected	with density spirals without velocity spirals
C5	$\langle\rho'_{\rm g}\rangle$	0	$\sqrt{R^2\Omega_{\rm K}^2\left(1-\frac{3}{2}\frac{Z^2}{R^2}\right)+\frac{R}{\langle\rho'_{\rm g}\rangle}\frac{\partial\langle P'\rangle}{\partial R}}$	0	Neglected	without density spirals without velocity spirals

NOTE — The superscript "$'$" in this table denotes evaluations from the snapshot at $t = 3000P_{\rm K,ref}$ in the fiducial Type A model, which are asymmetric fields with planet-driven spirals and meridional flows. The symbol $\langle\rangle$ denotes azimuthally averaged values. V_ϕ in model C4 and C5 assume hydrodynamic equilibrium. All values listed in this table are time-invariant in type C models. The last column explains the outcome of modifying $\{\rho_{\rm g}, \boldsymbol{V}\}$ fields. The velocity spiral refers primarily to the nonzero gas radial velocity correlated to the planet-driven spirals.

3.2 Results

3.2.1 Dust Rings Widened by the Gap-opening Planet

Compared with pressure bumps that are not planet-related (e.g., formed at the edge of dead zones or condensation frontiers), those at the outer edge of planet-opened gaps are additionally perturbed, as they are periodically swept by planetary wakes. In the meantime, dust grains trapped in those pressure bumps feel the wakes in two ways: perturbations in the gas density field that change the local stopping time of dust, and perturbations in the gas velocity field that change the velocity of dust. Here, we show that these two mechanisms, together with the insignificant nonaxisymmetric planetary potential on the dust (see below), can widen the dust ring.

Figure 3.1 shows the dust surface density profile in type C models at $t = 1000 P_{\rm K,ref}$. We first focus on the comparison between Model C1 and C5 in the top panel, which are static-gas models including a Gaussian dust ring at the edge of a planet-opened gap, with all three planet-related effects preserved in Model C1 and eliminated in C5 (see Table 3.2). Starting from the same initialization, the dust ring in Model C1 becomes much wider, whereas that in C5 continues to concentrate to the pressure maximum. This comparison shows that the net effect of the three planet-related effects widens the dust ring.

We then question which effect of the three contributes the most to the widening effect. We isolate the three effects by turning off the planetary potential and individually modifying $\rho_{\rm g}$ and $\boldsymbol{V}$ in Models C2, C3, and C4 (see Table 3.2), respectively. In the top panel of Figure 3.1, the comparison between Models C1 and C2 shows that the planetary potential on the dust is insignificant. In the bottom panel, {C2 vs C3} and {C4 vs C5} show that the perturbation in the gas density field is not the dominant effect. Finally, {C2 vs C4} and {C3 vs C5} show that it is the planetary wakes in the gas velocity field that are most responsible for the widening of the dust ring.

Meanwhile, we note that the dominance of gas velocity perturbations may only be applicable to the well-coupled dust ($\tau_{\rm s} \ll \Omega_{\rm K}^{-1}$) in our models, for which the terminal velocity approximation (Youdin and Goodman 2005; Jacquet et al. 2011; Price and Laibe 2015; Lovascio and Paardekooper 2019)

$$\boldsymbol{W} = \boldsymbol{V} + \frac{\nabla P}{\rho_{\rm g}(1+\epsilon_\rho)}\tau_{\rm s} \tag{3.14}$$

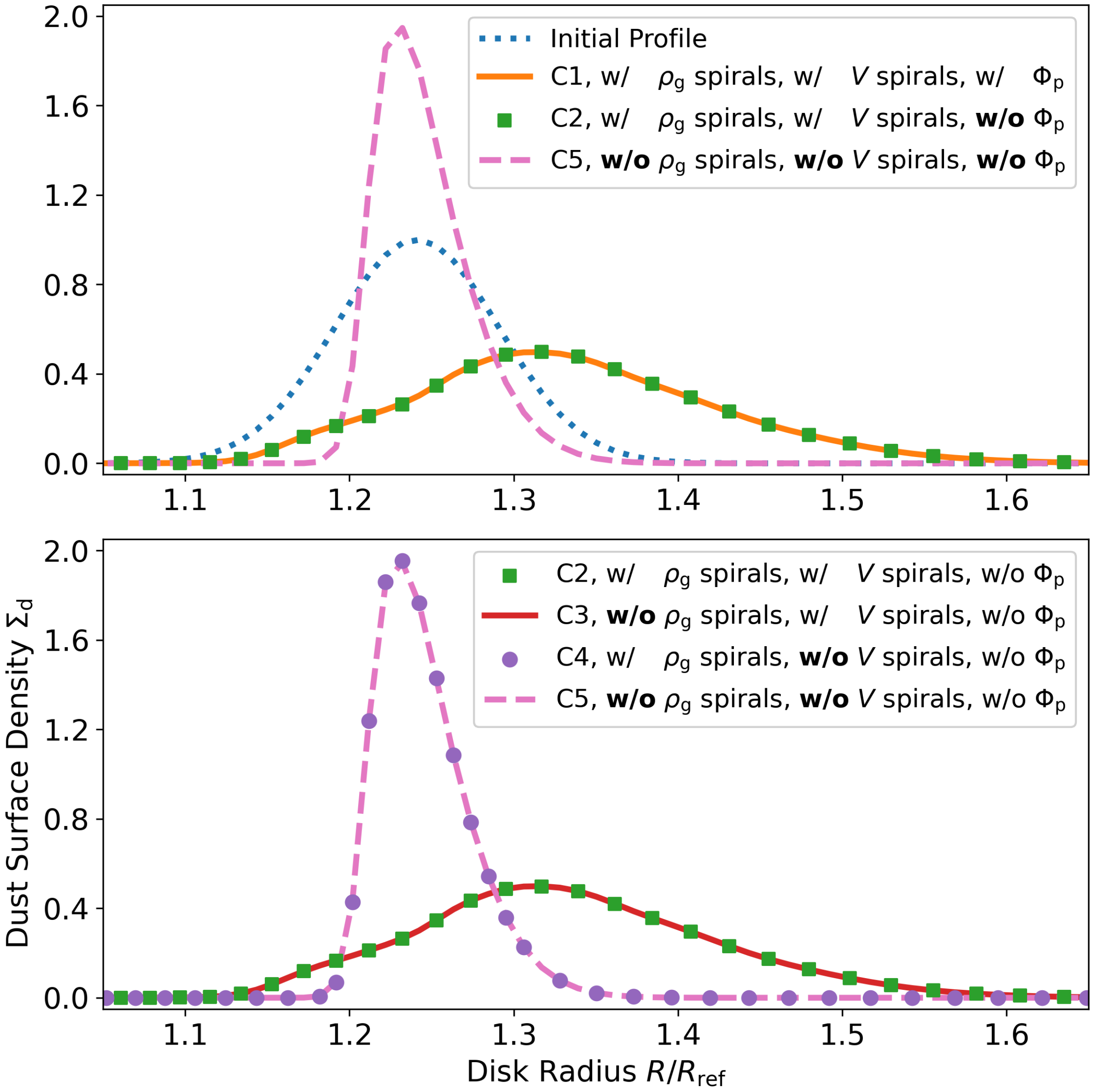

Figure 3.1: Azimuthally averaged dust surface density at $t = 1000P_{K,ref}$ in type C models. Two panels are provided for more convenient comparisons. All profiles are normalized to the peak value in the initial profile. The initial profile peaks at the radius of the pressure maximum in the midplane. The corresponding face-on views in Model C1 and C5 are provided in Figure 1.2.

is always dominated by the gas kinematics term, even if the density perturbations launched by the planet can lead to changes of τ_s by a few tens of percent. For larger grains in the disk, we would expect the density perturbations to play a more important role. Besides, we note that dust rings in Models C1, C2, and C3 are carried to larger radii while being widened by planet-related effects. This is the result of disabling dust back-reaction, which is required by the no-gas-evolution implementation and will be discussed in Section 3.2.2.

3.2.2 The Effect of Dust Back-reaction on Dust Rings

For a long time, numerical disk models neglected the dust back-reaction on the gas for simplicity and to reduce computational cost. This approximation worked well because conventional notions indicate a low dust-to-gas ratio ($\epsilon_\rho \ll 1$) in protoplanetary disks. However, Kanagawa et al. (2018) showed that in dust rings, where the dust concentrates, effective dust back-reaction is capable of flattening the radial profile of the pressure bump, leading to a broadened dust ring. Therefore, dust back-reaction is critical to the study of dust ring morphology.

To show that a gap-opening planet can widen dust rings on top of the effect of dust back-reaction, we make comparisons among type B models, which also include a Gaussian dust ring and a gas gap, but with different dust load levels. Different from the type C models in Section 3.2.1, the type B models here include the gas evolution and dust back-reaction. The top panel of Figure 3.2 shows how different levels of dust back-reaction would change the dust ring morphology on top of the same planet-related effects.

First, we find that in Models B1 and B2, in which dust back-reaction is negligible due to low dust load, the dust rings are widened and moved outward as much as that in Model C1. Then in Models B3 and B4, in which the midplane dust-to-gas ratio is close to one, the rings become narrower compared with those in Models B1 and B2, and are closer to the pressure maximum.

The comparison between models of low and moderate dust load levels confirms that dust back-reaction helps dust to resist effects that are related to the gas kinematics. When the dust back-reaction is negligible (Models B1 and B2) or even neglected (Model C1), the planetary wakes are capable of not only widening the dust ring but also providing an outward net mass flux that, together with the gas meridional flows, carries well-coupled dust grains outward. When the dust back-reaction is moderately strong ($\epsilon_\rho \sim 1$), the dust ring can still be widened, albeit to a lesser extent, and it becomes harder for it to be carried outward by gas flows, as it acts like a damper to those effects.

Therefore, we conclude that when ϵ_ρ increases from 0 to 1, the dust ring at the edge of the planet-opened gap would become narrower. It may seem to contradict the result in Kanagawa et al. (2018), which states effective dust back-reaction would flatten the

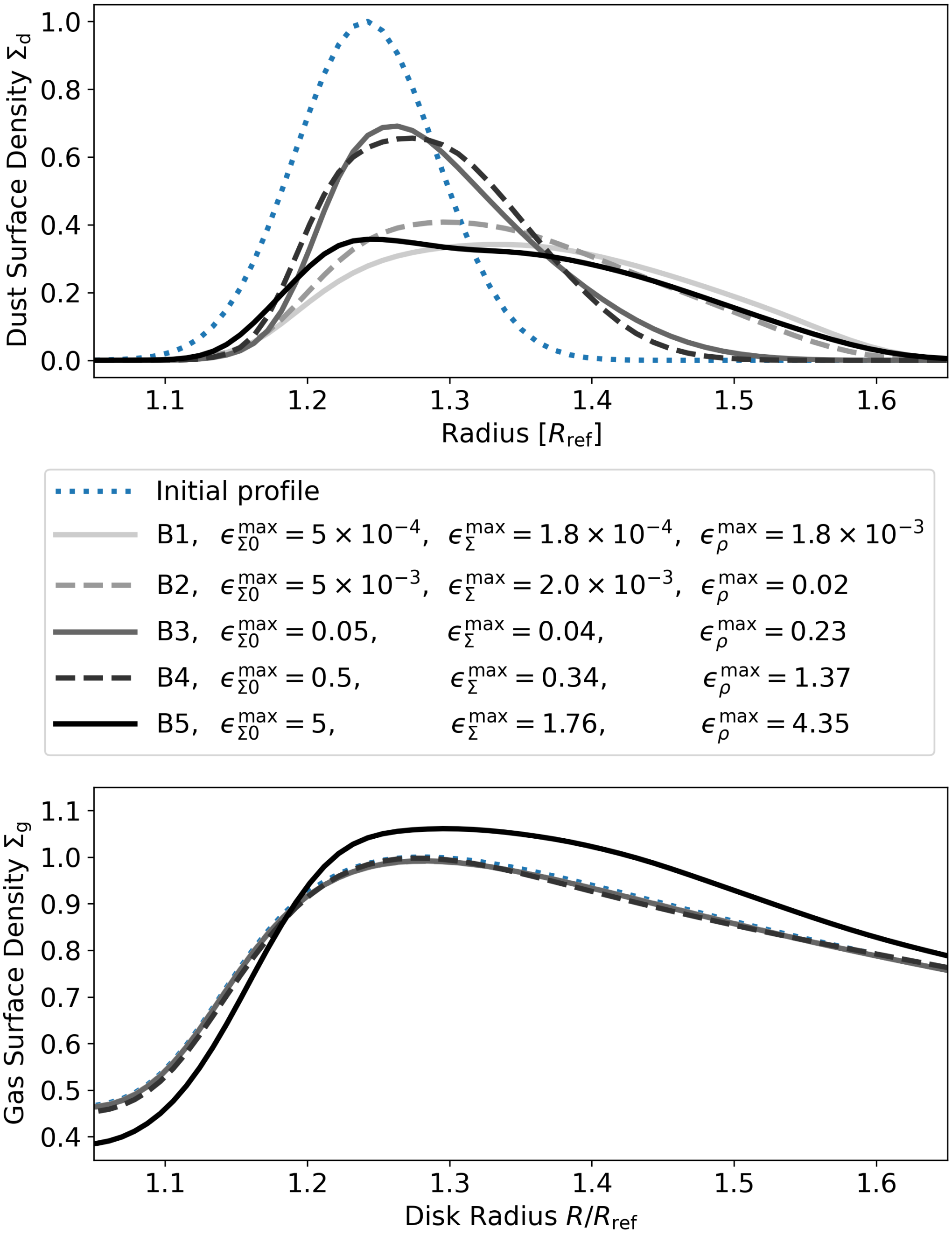

Figure 3.2: Azimuthally averaged dust and gas surface density at $t = 1000P_{\rm K,ref}$ in type B models. All profiles are normalized to the corresponding maximum value in the initial profile. Because dust rings in different models are initialized with the same radial width but different dust load levels, we only compare the radial location and width of profiles in the top panel. The maximum values of the dust-to-gas surface density ratio $\epsilon_{\Sigma}^{\rm max}$, as well as its initial value $\epsilon_{\Sigma 0}^{\rm max}$ and the corresponding midplane density ratio $\epsilon_{\rho}^{\rm max}$, are listed in the legends.

global pressure profile and make the dust ring wider, but it is not. In Models B3 and B4, the maximum *local* density ratio $\epsilon_\rho^{\max}$ is close to one, but the vertically integrated *global* surface density ratio $\epsilon_\Sigma^{\max}$, which is the term monitored in the 2D disk model in Kanagawa et al. (2018), is much smaller. This means even though the dust can deform the pressure profile close to the midplane via back-reaction, the gas on top of the midplane can compensate for that. Similar phenomena can be seen from the comparison between the axisymmetric (radial-vertical), unstratified disk models in Taki et al. (2016) and the stratified models in Onishi and Sekiya (2017). In our models, this argument is supported by the bottom panel of Figure 3.2, which shows that the gas density profiles from Models B1 to B4 are all consistent with each other. When it comes to both $\epsilon_\Sigma^{\max} > 1$ and $\epsilon_\rho^{\max} > 1$ in Model B5, the dust ring becomes so dust-rich that it is capable of deforming the global gas density profile via overwhelming back-reaction. Then the dust ring becomes wider as a result of the pressure profile being flattened, in agreement with Kanagawa et al. (2018).

To conclude, moderate dust back-reaction ($\epsilon_\rho \sim 1$) tends to make the dust ring narrower by damping the planetary perturbations. However, when $\epsilon_\Sigma > 1$ and $\epsilon_\rho > 1$, the ring expands itself during the process of deforming the global pressure profile via overwhelming back-reaction, with the widening effect being no more attributable to the planet-related effects. We note that Model B3 provides the most similar dust load level to our type A models ($\epsilon_\rho^{\max} \sim 0.5$) in Section 3.2.3 and conventional models of protoplanetary disks. Therefore, the dust rings in our type A models tend to demonstrate the minimum width under the net effect of planetary perturbations and dust back-reaction.

3.2.3 How Much Can the Dust Ring Be Widened by a Planet?

The radial FWHM of an equilibrated dust ring $w_{\rm d}$ is determined by the balance between the concentration effect due to pressure gradient and the expansion effect due to diffusion. Therefore, in our models without the turbulence-induced dust diffusion, if the planet can widen dust rings and maintain this effect, the dust rings can be modeled as being widened by an effective diffusion with a diffusion tensor $\mathcal{D}$. In this section, we first try to establish a quantification of $\mathcal{D}$ via gradient diffusion hypothesis, and then derive the relation between $\mathcal{D}$ and $w_{\rm d}$.

Quantify $\mathcal{D}$ with Gradient Diffusion Hypothesis

The planet-related effects expand dust rings via introducing fluctuations to the disk, which may be modeled as diffusion. If so, we would like to quantify those fluctuations in order to obtain the diffusion coefficients. In our disk models, a physical variable A can be azimuthally decomposed to $A = \langle A\rangle + \Delta A$, where $\langle A\rangle$ is the mean field and ΔA is the fluctuation term with $\langle \Delta A\rangle = 0$. Applying the decomposition to Equation 3.4 and then taking the azimuthal average, we get

$$\frac{\partial\langle\rho_{\rm d}\rangle}{\partial t} = -\nabla\cdot(\langle\rho_{\rm d}\rangle\langle\boldsymbol{W}\rangle) - \nabla\cdot\langle\Delta\rho_{\rm d}\Delta\boldsymbol{W}\rangle. \tag{3.15}$$

The product term of fluctuations above is associated with diffusion via the gradient diffusion hypothesis (e.g., Cuzzi et al. 1993; Tominaga et al. 2019)

$$\langle\Delta\rho_{\rm d}\Delta\boldsymbol{W}\rangle = -\mathcal{D}\nabla\langle\rho_{\rm d}\rangle, \tag{3.16}$$

where

$$\mathcal{D} = \begin{bmatrix} \mathcal{D}_{RR} & \mathcal{D}_{RZ} \\ \mathcal{D}_{ZR} & \mathcal{D}_{ZZ} \end{bmatrix} \tag{3.17}$$

is a diffusion tensor that describes the dust diffusion in the frame of the disk. We note that only diffusions in $\{R, Z\}$ directions are considered here, as the ϕ components become irrelevant in Equation 3.15. Equation 3.16 provides a quantification of $\mathcal{D}$, but it does not give a unique solution, because it only has two equations for the four components of $\mathcal{D}$. Therefore, we assume $\mathcal{D}_{RZ} = \mathcal{D}_{ZR} = 0$, indicating the radial gradient of density does not contribute to vertical diffusion, and vice versa, to reduce number of unknowns. Then, for conciseness, we use $\mathcal{D}_R$ and $\mathcal{D}_Z$ to denote $\mathcal{D}_{RR}$ and $\mathcal{D}_{ZZ}$, respectively. Nevertheless, $\mathcal{D}$ at the dust peak (where $\nabla\langle\rho_{\rm d}\rangle = 0$), which is the key for the widening effect of the dust ring, cannot be quantified via Equation 3.16. Therefore, we quantify $\mathcal{D}$ via balancing the advection term and the diffusion term in Equation 3.15, in a steady state where $\partial\langle\rho_{\rm d}\rangle/\partial t = 0$. Later, in Section 3.2.3, we will show that a profile of $\mathcal{D}$ with $\nabla\mathcal{D} \sim 0$ in the extent of the dust ring, and a scenario where advection and diffusion are balanced in individual directions, are preferred while associating $\mathcal{D}$ with $w_{\rm d}$. Therefore, here we would expect a constant

$\overline{\mathcal{D}}$ at the dust ring with

$$\nabla_Z \cdot (\langle\rho_{\rm d}\rangle\langle W_Z\rangle) = \overline{\mathcal{D}}_Z \nabla_Z^2 \langle\rho_{\rm d}\rangle \tag{3.18}$$

$$\nabla_R \cdot (\langle\rho_{\rm d}\rangle\langle W_R\rangle) = \overline{\mathcal{D}}_R \nabla_R^2 \langle\rho_{\rm d}\rangle. \tag{3.19}$$

We then run type A models to validate this method. Different from those in type B and C models, gas and dust densities in type A models are both initialized to power-law radial profiles, with no gaps or rings. When simulations begin, the planet mass increases from zero and gradually opens a gap, which eventually leads to the formation of a dust ring. Type A models are differentiated by the planet mass and Stokes number, with the model of $\{M_{\rm p}, {\rm St}_{0,{\rm ref}}\} = \{3 \times 10^{-4} M_\star, 10^{-3}\}$ being the fiducial one. To provide near-steady states, all type A models are run for $3000 P_{\rm K,ref}$.

The profiles of terms in Equations 3.18 and 3.19, evaluated vertically and radially across the dust peak, are shown in panels *a* and *b* in Figure 3.3. We choose constant values of $\overline{\mathcal{D}}$ and find no good match between the advection term and the diffusion term. Panel *a* shows that, while the vertical profile of the diffusion term is an even function relative to the midplane, the profile of the advection term is close to an odd one. In our model, this qualitative mismatch is resulted from a meridional flow that not only crosses the midplane but also penetrates through the dust layer, which breaks the symmetry along the midplane that is conventionally assumed in previous studies. The meridional flows affect the radial profiles as well. In panel *b*, although the two profiles are similar in a large radial extent, they have different zero-crossings, which indicates that there are negative diffusion coefficients in part of the ring. Besides, the two profiles diverge at $R \sim 1.23 R_{\rm ref}$, which is still within the half width at half maximum to the peak. In addition, we note that the two mismatches in the radial and vertical direction do not compensate for each other, and they cannot be fixed by setting nonzero values of $\overline{\mathcal{D}}_{RZ}$ and $\overline{\mathcal{D}}_{ZR}$ (see Appendix B.2). Therefore, we conclude that this method of quantifying a constant $\overline{\mathcal{D}}$ at the dust ring using the gradient diffusion hypothesis is not applicable to our disk models with active meridional flows induced by gap-opening planets.

Modifying the Gradient Diffusion Hypothesis

In our models, the advection of well-coupled dust is correlated to the gas kinematics. However, the method in the above section does not have any explicit dependence on the gas. Here, we show that, after taking the nontrivial gas density and velocity field

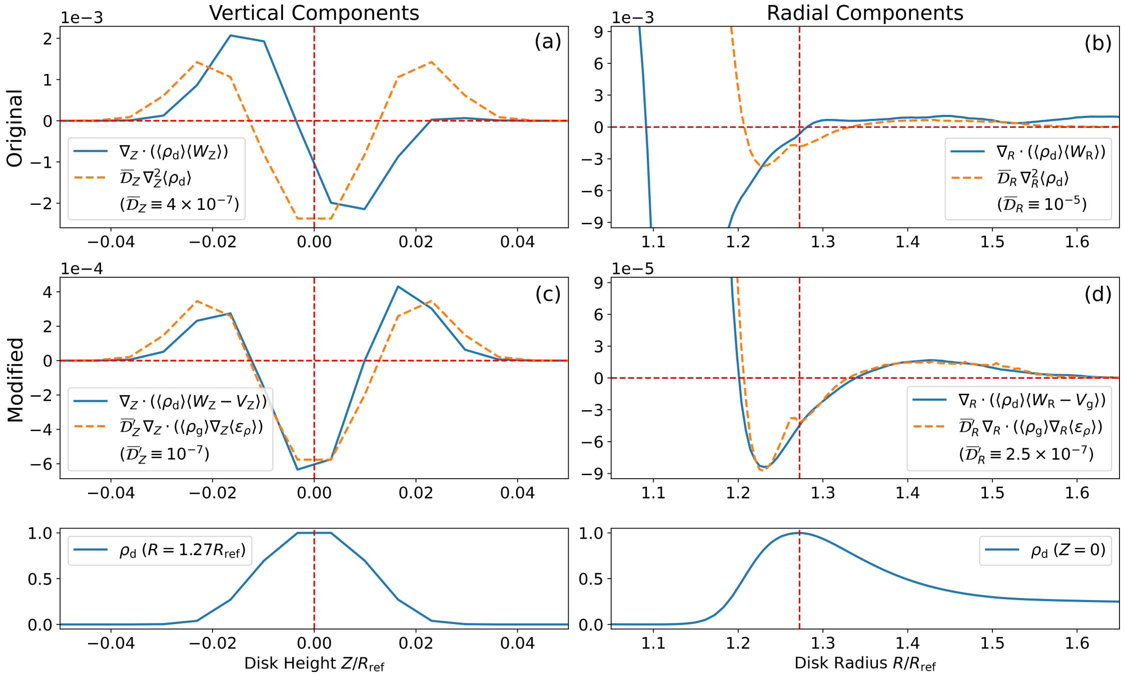

Figure 3.3: The comparison among the simulation result and different advection-diffusion theories. (a): The vertical profile of terms in Equation 3.18 at the dust peak. (b): The radial profile of terms in Equation 3.19 in the midplane. (c): The vertical profile of vertical components in Equation 3.23 at the dust peak. (d): The radial profile of radial components in Equation 3.23 in the midplane. All profiles are evaluated in the fiducial type A model at $t = 3000P_\mathrm{K,ref}$. The demonstrative constant diffusion coefficients $\overline{\mathcal{D}}$ and $\overline{\mathcal{D}}'$, in the unit of $R_\mathrm{ref}^2\Omega_\mathrm{K,ref}$, are chosen such that the two curves in each panel are at the same order of magnitude. Panel a and b represent the original gradient diffusion hypothesis in Section 3.2.3. Panel c and d represent the modified gradient diffusion hypothesis in Section 3.2.3. Panel a and c are normalized to the midplane dust density at the dust peak. Panel b and d are normalized to the radial profile of the midplane dust density. The vertical red dashed lines in the left column denote $Z = 0$, the ones in the right column denote the dust peak at $R = 1.27R_\mathrm{ref}$. The horizontal red dashed lines denote $y = 0$. The normalized vertical and radial profiles of dust density are shown in the bottom for reference.

into consideration, a *modified* gradient diffusion hypothesis can model fluctuations of the relative motion between gas and dust.

To address the effects of bulk motion and fluctuation of gas, we first apply the azimuthal decomposition to Equation 3.2 to get

$$\frac{\partial\langle\rho_\mathrm{g}\rangle}{\partial t} = -\nabla\cdot(\langle\rho_\mathrm{g}\rangle\langle\boldsymbol{V}\rangle) - \nabla\cdot\langle\Delta\rho_\mathrm{g}\Delta\boldsymbol{V}\rangle. \tag{3.20}$$

Considering both fluctuation terms in Equations 3.15 and 3.20, we modify Equation

3.16 (to be justified a posteriori) to

$$\nabla \cdot \langle \Delta\rho_{\rm d} \Delta \boldsymbol{W} \rangle - \langle \epsilon_\rho \rangle \nabla \cdot \langle \Delta\rho_{\rm g} \Delta \boldsymbol{V} \rangle \\ = -\nabla \cdot \Big(\mathcal{D}' \langle \rho_{\rm g} \rangle \nabla \langle \epsilon_\rho \rangle \Big), \tag{3.21}$$

where $\langle \epsilon_\rho \rangle = \langle \rho_{\rm d} \rangle / \langle \rho_{\rm g} \rangle$ is the mean field dust-to-gas ratio. Here, $\mathcal{D}'$ is the diffusion tensor that describes the diffusion of dust *relative to* the gas, also with nondiagonal elements assumed to be zero. Instead of the steady state for both gas and dust with $\partial\langle \rho_{\rm d} \rangle / \partial t = \partial \langle \rho_{\rm g} \rangle / \partial t = 0$, we suggest that $\mathcal{D}'$ can be quantified in a more general case with

$$\frac{{\rm D}\langle \epsilon_\rho \rangle}{{\rm D}t} = \frac{\partial \langle \epsilon_\rho \rangle}{\partial t} + \langle \boldsymbol{V} \rangle \cdot \nabla \langle \epsilon_\rho \rangle = 0. \tag{3.22}$$

Equation 3.22 is an advection equation that says the Lagrangian derivative of $\langle \epsilon_\rho \rangle$ is zero. That is, the dust-to-gas ratio following a gas parcel remains constant. Considering Equations 3.15, 3.20, and 3.21, Equation 3.22 is equivalent to (see Appendix B.3)

$$\nabla \cdot \Big(\langle \rho_{\rm d} \rangle \langle \boldsymbol{W} - \boldsymbol{V} \rangle \Big) + \nabla \cdot \Big(\mathcal{D}' \langle \rho_{\rm g} \rangle \nabla \langle \epsilon_\rho \rangle \Big) = 0, \tag{3.23}$$

which says the relative advection between gas and dust balances the relative diffusion between them.

We note that the dust and gas in the above state are not necessarily steady ($\partial/\partial t \neq 0$). For example, Equations 3.22 and 3.23 are still applicable when the dust and gas are moving together in space due to bulk motions while maintaining no relative evolution. In other words, for the purpose of associating $\mathcal{D}'$ with $w_{\rm d}$ in Section 3.2.3, we only need an equilibrated $w_{\rm d}$. We also note that the combination of Equations 3.22 and 3.23 agrees with the correct[2] advection-diffusion equation in the context of protoplanetary disks discussed in Desch et al. (2017).

Figure 3.3 (panel *c*–*d*) shows the profiles of terms in Equation 3.23. We find that the relative diffusion and advection balance in both directions, and the match of profiles can be obtained by constant $\overline{\mathcal{D}}'_R$ and $\overline{\mathcal{D}}'_Z$, but with different values. Therefore, we conclude that the radial component of diffusion coefficient $\mathcal{D}'_R$ at the dust peak can be quantified using the modified gradient diffusion hypothesis, and it can be approximated as a constant value in the radial extent of the dust ring.

---

[2] Other forms may lead to inappropriate derivations with wrong coefficients or unphysical terms

Associating $\mathcal{D}'$ with the Dust Ring Width $w_{\rm d}$

After quantifying $\mathcal{D}'_R$, the dust ring width $w_{\rm d}$ can be obtained with certain dust and gas density profiles. For simplicity, in this section we focus on the correlation between $\mathcal{D}'_R$ and $w_{\rm d}$ within the immediate vicinity of the dust peak in the midplane. For conciseness, all variables in this section are azimuthally averaged by default. Although $\rho_{\rm d}$ and $\rho_{\rm g}$ may not peak at the same location, we assume $\partial\rho_{\rm g}/\partial R \sim 0$, and consequently $\partial\epsilon/\partial R \sim 0$, in the vicinity[3].

As we show in Figure 3.3, the balance in Equation 3.23 can be reached in individual directions. Here, we write the radial part of it:

$$-\frac{\partial}{\partial R}\left[R\rho_{\rm d}(W_R - V_R)\right] + \frac{\partial}{\partial R}\left(R\mathcal{D}'_R\rho_{\rm g}\frac{\partial\epsilon_\rho}{\partial R}\right) = 0. \tag{3.24}$$

With the dust kinematics in our models agreeing with the terminal velocity approximation (Equation 3.14), after rewriting $\rho_{\rm g}\partial\epsilon_\rho/\partial R = \partial\rho_{\rm d}/\partial R - \epsilon_\rho\partial\rho_{\rm g}/\partial R$, and considering the locally isothermal equation of state and the power-law radial temperature profile, we get

$$\begin{aligned}\frac{\partial}{\partial R}\Bigg[\epsilon_\rho R\left(\frac{\tau_{\rm s}c_{\rm s}^2}{1+\epsilon_\rho} + \mathcal{D}'_R\right)\frac{\partial\rho_{\rm g}}{\partial R}& \\ -\epsilon_\rho qR\frac{\tau_{\rm s}c_{\rm s}^2}{1+\epsilon_\rho}\frac{\rho_{\rm g}}{R} - R\mathcal{D}'_R\frac{\partial\rho_{\rm d}}{\partial R}\Bigg] &= 0.\end{aligned} \tag{3.25}$$

Assuming $\partial\mathcal{D}'_R/\partial R \sim 0$ in the vicinity[4], and recalling previous assumptions of $\partial\rho_{\rm d}/\partial R \sim \partial\rho_{\rm g}/\partial R \sim \partial\epsilon_\rho/\partial R \sim 0$ there, the terms with first-order derivatives in Equation 3.25 can be dropped, and Equation 3.25 can be approximated to

$$\epsilon_\rho\left(\frac{\tau_{\rm s}c_{\rm s}^2}{1+\epsilon_\rho} + \mathcal{D}'_R\right)\frac{\partial^2\rho_{\rm g}}{\partial R^2} + \frac{q^2}{2}\frac{\tau_{\rm s}c_{\rm s}^2}{1+\epsilon_\rho}\frac{\rho_{\rm d}}{R} - \mathcal{D}'_R\frac{\partial^2\rho_{\rm d}}{\partial R^2} = 0. \tag{3.26}$$

To associate Equation 3.26 with the radial width of disk structures, we assume both

---

[3] This approximation is appropriate in our type A models with moderate ($\epsilon_\rho \sim 1$) dust back-reaction.

[4] This approximation is discussed in Section 3.2.3.

gas and dust density profiles in the vicinity are Gaussian:

$$\rho_{\rm g}(R) = \rho_{\rm g}(R_{\rm g}) \times \exp\left[-\frac{(R-R_{\rm g})^2}{2w_{\rm g}^2}\right] \tag{3.27}$$

$$\rho_{\rm d}(R) = \rho_{\rm d}(R_{\rm d}) \times \exp\left[-\frac{(R-R_{\rm d})^2}{2w_{\rm d}^2}\right]. \tag{3.28}$$

$R_{\rm g}$ and $R_{\rm d}$ are the radii where the gas and dust density profile peak, and $w_{\rm g}$ and $w_{\rm d}$ are the widths of the dust ring and the gas bump. By approximating $w_{\rm g}^2 \gg (R-R_{\rm g})^2$ within the vicinity of the dust peak, we find

$$\frac{\partial^2 \rho_{\rm g}}{\partial R^2} = \rho_{\rm g}\frac{(R-R_{\rm g})^2 - w_{\rm g}^2}{w_{\rm g}^4} \approx -\frac{\rho_{\rm g}}{w_{\rm g}^2} \tag{3.29}$$

$$\frac{\partial^2 \rho_{\rm d}}{\partial R^2} = \rho_{\rm d}\frac{(R-R_{\rm d})^2 - w_{\rm d}^2}{w_{\rm d}^4} \approx -\frac{\rho_{\rm d}}{w_{\rm d}^2}. \tag{3.30}$$

Then taking those back to Equation 3.26, we finally get

$$w_{\rm d} = \sqrt{\frac{\mathcal{D}'_R}{\left(\frac{\tau_{\rm s} c_{\rm s}^2}{1+\epsilon_\rho} + \mathcal{D}'_R\right)\frac{1}{w_{\rm g}^2} - \frac{\tau_{\rm s} c_{\rm s}^2}{1+\epsilon_\rho}\frac{q^2}{2R^2}}}, \tag{3.31}$$

which shows how much the dust ring can be widened by the diffusion-like behavior, given the radial location, the stopping time, the dust-to-gas ratio, the sound speed profile, and the gas structure at the dust ring. We note that, in the limit of $w_{\rm g}^2 \ll 2R^2/q^2$ and $(1+\epsilon_\rho)\mathcal{D}'_R \ll \tau_{\rm s} c_{\rm s}^2$, Equation 3.31 can be approximated to

$$w_{\rm d} = w_{\rm g}\sqrt{\frac{(1+\epsilon_\rho)\mathcal{D}'_R}{\tau_{\rm s} c_{\rm s}^2}}, \tag{3.32}$$

which is similar to the Equation 46 in Dullemond et al. (2018), but with different definitions of parameters.

3.3 Discussion

Connection to the Turbulent Viscosity

In this work, we provide a way to associate the planet-related diffusion coefficient $\mathcal{D}'_R$ with the dust ring width $w_{\rm d}$. However, in disk observations, $\mathcal{D}'_R$ is neither measurable nor a property that can be easily constrained by measurables, making it hard to infer any properties of the suspected planet using the dust ring width. Here, we discuss the feasibility of associating $\mathcal{D}'_R$ of the dust component with the Reynolds stress $\mathcal{R}$ of the gas component, which describes the radial turbulent angular momentum transport in the disk and is more easily constrained in observations.

In our 3D disk model, we calculate the azimuthally averaged profile of the Reynolds stress via

$$\mathcal{R} = \langle \rho_{\rm g} \Delta V_{\rm R} \Delta V_{\phi} \rangle, \tag{3.33}$$

where ΔV is the fluctuation of gas velocity to its mean field. Then the turbulent viscosity parameter $\alpha_{\rm turb}$ (Shakura and Sunyaev 1973) can be obtained via

$$\alpha_{\rm turb} = \mathcal{R}/\langle P \rangle = \frac{\nu_{\rm turb}}{c_{\rm s} H}, \tag{3.34}$$

where $\nu_{\rm turb}$ is the measured kinematics viscosity and may not be identical to the implemented ν in the model. Because the ratio between the momentum diffusivity (i.e., the kinematics viscosity) and the mass diffusivity (i.e., the diffusion coefficient) is the Schmidt number Sc, Equation 3.31 and 3.32 can be rewritten to

$$w_{\rm d} = \left[\left(1 + \frac{1}{\psi^2}\right) \frac{1}{w_{\rm g}^2} - \frac{1}{\psi^2} \frac{q^2}{2R^2} \right]^{-1/2} \tag{3.35}$$

and

$$w_{\rm d} = w_{\rm g} \psi, \tag{3.36}$$

where

$$\psi = \sqrt{\frac{(1+\epsilon_\rho)\mathcal{D}'_R}{\tau_{\rm s} c_{\rm s}^2}} = \sqrt{\frac{(1+\epsilon_\rho)\alpha_{\rm turb}}{\mathrm{St}\,\mathrm{Sc}}}. \tag{3.37}$$

Figure 3.4 shows the measured $\mathcal{D}'_R$, $\alpha_{\rm turb}$, and the corresponding Schmidt number at the dust peak in type A models with different planet masses and Stokes numbers of dust. Our resulting $\alpha_{\rm turb}$ values agree with the accretion levels estimated in disks with one or more planets of a few Earth masses in previous works (Goodman and Rafikov 2001; Fung and Chiang 2017). In the meantime, we show that the resulting Schmidt number is larger than the conventionally assumed of order unity. These large Sc numbers suggest that the planet-related transport of mass and momentum may depend on the specific form of turbulence or perturbation that only partially represents the turbulent or perturbed nature in the gas. Therefore, we advise caution with regard

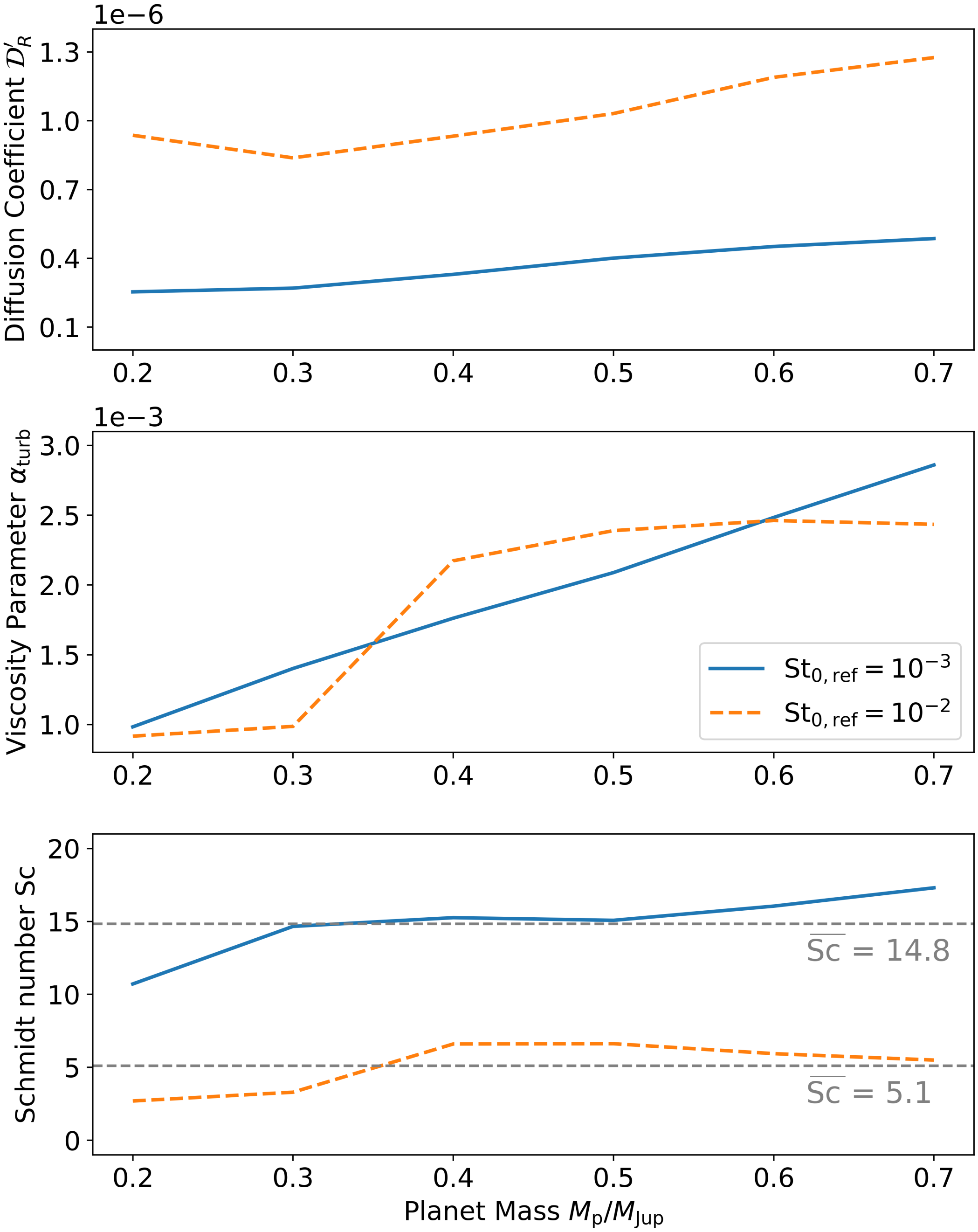

Figure 3.4: Diffusion-related parameters in type A models showing the effect of the planet mass. The radial diffusion coefficient $\mathcal{D}'_R$ (*top*) from Equation 3.24, the turbulent viscosity parameter $\alpha_{\rm turb}$ (*middle*) from Equation 3.34, and the corresponding Schmidt number Sc (*bottom*) at the dust peak in different type A models. All profiles are evaluated in the midplane at $t = 3000 P_{\rm K,ref}$. The unit of $\mathcal{D}'_R$ in the top panel is $R^2_{\rm ref}\Omega_{\rm K,ref}$. Horizontal dashed lines in the bottom panel mark the averaged Schmidt number $\overline{\rm Sc}$ for models with the same $\mathrm{St}_{0,\rm ref}$.

to the assumption of Sc $= 1$ in studies on turbulent effects in protoplanetary disks. For models with the same $\mathrm{St}_{0,\mathrm{ref}}$, we find the Schmidt numbers are similar. Whether this is a coincidence, why Sc decreases with increasing St, and how Sc changes with other disk parameters, will be investigated in the future.

Overall, there is a possible avenue to estimate the properties of the suspected planet from disk observations. Since Sc is only sensitive to St in our setting (bottom panel of Figure 3.4), measurements of the size and St of dust at the ring via multiwavelength dust observations and spectral energy distribution modeling (e.g., Guidi et al. 2022) or mm-wavelength polarization observations (e.g., Kataoka et al. 2016) may lead to constraints on Sc. Because the α_{turb} value and the dust ring width w_{d} may be obtained from gas and dust observations (e.g., Flaherty et al. 2020), the gas bump width w_{g} may be constrained from Equation 3.36 with certain assumptions on the level of ϵ_ρ. Finally, because the radial gas density profile modified by a gap-opening planet, which includes the gas bump, can be estimated analytically (e.g., Duffell 2015, 2020), the orbital radius and mass of the suspected planet may be obtained.

3.4 Conclusion

In this chapter, we use 3D hydrodynamic simulations to study dust kinematics in protoplanetary disks where a planet is present. Our main findings are:

1. Compared with dust rings trapped at axisymmetric pressure bumps, those trapped at planet-induced pressure bumps featuring density waves are widened by planet-disk interactions. For dust rings composed of small ($\mathrm{St} \lesssim 10^{-2}$) grains, the fluctuations in the gas velocity field due to planetary wakes are most responsible for the widening effect.

2. Moderate dust back-reaction with local dust-to-gas ratio $\lesssim 1$ tends to narrow dust rings under the planet-related effects, compared with the cases where dust back-reaction is negligible. However, overwhelming dust back-reaction with dust-to-gas ratios of both volumetric and surface density > 1 would lead to the dust ring expanding itself while deforming the global pressure profile. In the overwhelmingly high dust mass regime, both dust back-reaction and planet-related effects are in effect, but the former takes dominance.

3. The widening effect of dust rings due to planet-related effects can be modeled by our modified gradient diffusion hypothesis, and can be quantified by a diffusion coefficient on the order of 10^{-7}–$10^{-6} R^2\Omega_{\rm K}$. We note that the conventional gradient diffusion hypothesis with globally constant diffusion coefficients is not applicable to our 3D disk models with planet-induced meridional flows.

4. We show that the widening effect can also be quantified by the Reynolds stress, with the corresponding turbulent viscous parameter $\alpha_{\rm turb}$ on the order of 10^{-3}. However, we caution about the Schmidt number being greater than order unity. It suggests that a high momentum diffusivity of gas does not always translate to high mass diffusivity of dust, even for well-coupled dust ($\tau_{\rm s} \ll \Omega_{\rm K}^{-1}$) in the disk.

Appendix A

In the Pre-Planet-Formation Era: Dust Dynamics under Irradiation Instability in Transitional Disks

A.1 Terminal Velocity of Dust Grains under Radiation Pressure

A significant fraction of our parameter employs a small Stokes number St. The corresponding stopping time is often shorter than the time step of our simulations, and so we would expect the velocities of the super-particles to be closely approximated by their terminal velocities. We solve for these velocities in this appendix.

Without loss of generality, we define the terminal values of the radial speed and specific angular momentum of a super-particle as follows

$$W_{\mathrm{r,term}} = u\, v_{\mathrm{K}} \tag{A.1}$$

$$l_{\mathrm{term}} = (1 - L)\, l_{\mathrm{K}}\,, \tag{A.2}$$

where u and L are dimensionless parameters, $v_{\mathrm{K}} = \sqrt{GM/r}$ and $l_{\mathrm{K}} = v_{\mathrm{K}} r$ are the Keplerian speed and angular momentum, respectively. At terminal speed, we expect u and L to reach equilibrium, constant values, in other words, $\dot{u} = \dot{L} = 0$. Without any explicit dependence on time, the radial acceleration can be expressed as $\dot{W}_{\mathrm{r,term}} = (\mathrm{d}W_{\mathrm{r,term}}/\mathrm{d}r)W_{\mathrm{r,term}}$, and similarly for the torque $\dot{l}_{\mathrm{term}}$. This allows us to write the acceleration and torque equations as

$$-\frac{1}{2}\frac{W_{\mathrm{r,term}}^2}{r} = -\frac{GM}{r^2}\left(1 - \beta e^{-\tau}\right) + \frac{l_{\mathrm{term}}^2}{r^3} - \frac{W_{\mathrm{r,term}}}{\mathrm{St}\,\Omega_{\mathrm{K}}^{-1}} \tag{A.3}$$

$$\frac{1}{2}\frac{l_{\mathrm{term}} W_{\mathrm{r,term}}}{r} = -\frac{l_{\mathrm{term}} - l_{\mathrm{gas}}}{\mathrm{St}\,\Omega_{\mathrm{K}}^{-1}}\,. \tag{A.4}$$

Dividing Equation A.3 by v_K^2/r and A.4 by v_K^2, we obtain the dimensionless equations

$$-\frac{u^2}{2} = -1 + \beta_\mathrm{eff} + (1-L)^2 - \frac{u}{\mathrm{St}} \tag{A.5}$$

$$\frac{u\,(1-L)}{2} = \frac{-1 + L + f_\mathrm{gas}}{\mathrm{St}}\,, \tag{A.6}$$

where we have, for convenience, defined $\beta_\mathrm{eff} = \beta e^{-\tau}$ and $l_\mathrm{gas} = f_\mathrm{gas} l_\mathrm{K}$ such that $f_\mathrm{gas} = \sqrt{1-\eta}$. Solving for u and L, we obtain

$$u = \frac{1 - \sqrt{1 - 2\mathrm{St} u_0}}{\mathrm{St}} \tag{A.7}$$

$$L = \frac{1 - f_\mathrm{gas} + \frac{\mathrm{St}}{2} u}{1 + \frac{\mathrm{St}}{2} u}\,, \tag{A.8}$$

where $u_0 = \mathrm{St}\left(\beta_\mathrm{eff} - 2L + L^2\right)$. This set of equations has no simple analytic solution, but can be solved through iterations to any desired precision. A good starting point is to assume $\mathrm{St}\,u_0 \ll 1$, which allows us to write

$$u = u_0 + O(\mathrm{St}\,u_0^2)\,, \tag{A.9}$$

and

$$L = 1 - f_\mathrm{gas} + f\frac{\mathrm{St}}{2} u_0 + O((\mathrm{St}\,u_0)^2)\,. \tag{A.10}$$

Dropping terms of order $(\mathrm{St}\,u_0)^2$ and smaller, we can solve for L:

$$L \approx \frac{1 + \mathrm{St}^2 f_\mathrm{gas}}{\mathrm{St}^2 f_\mathrm{gas}} \left(1 - \sqrt{1 - 2\frac{\mathrm{St}^2 f_\mathrm{gas}\left(1 - f_\mathrm{gas} + \mathrm{St}^2 f_\mathrm{gas}\beta_\mathrm{eff}/2\right)}{(1 + \mathrm{St}^2 f_\mathrm{gas})^2}}\right)\,, \tag{A.11}$$

and then obtain u by plugging L back into Equation A.7. Using this approximation as the initial guess and applying Steffensen's method for iterative root finding, we can solve Equations A.7 and A.8 to double precision numerical accuracy in typically one or two iterations.

While we use Equations A.7, A.8, and A.11 to obtain numerically accurate solutions, it is helpful to also simplify the equations further to gain some intuition into the problem. Taking $\eta \ll 1$ and keeping only leading order terms in η, u_0, and L, we get:

$$u \approx \frac{\mathrm{St}}{1+\mathrm{St}^2}\left(\beta_{\mathrm{eff}}-\eta\right) \tag{A.12}$$

$$L \approx \frac{\eta+\mathrm{St}^2\beta_{\mathrm{eff}}}{2\left(1+\mathrm{St}^2\right)}\,. \tag{A.13}$$

We use these approximated solutions to inform our analysis in Section 2.2.

Appendix B

In the Post-Planet-Formation Era: Dust Dynamics under Planet-Disk Interactions at Pressure Bumps

B.1 Disk Plots of Model C1 and C5

To show the differences in the gas initialization between Model C1 and C5, we plot the face-on view of gas surface density and midplane gas radial velocity in Figure B.1.

B.2 The Mismatch Between Advection and Diffusion With the Gradient Diffusion Hypothesis

Figure B.2 shows the vertically integrated advection and diffusion terms from Equation 3.15 and 3.16. In the top panel, the constant diffusion tensor elements $\overline{\mathcal{D}}_R$ and $\overline{\mathcal{D}}_Z$ are identical to the ones in the top row of Figure 3.3. We find that the two profiles still do not match, similar to those in Figure 3.3 (*a*–*b*), even when both radial and vertical components are taken into consideration. In the bottom panel, $\overline{\mathcal{D}}_R$ and $\overline{\mathcal{D}}_Z$ are numerically fitted within the plotted range for the best match between the two profiles. While we do not find a match as good as the ones in the middle row of Figure 3.3 with the modified gradient diffusion hypothesis, the fitted $\overline{\mathcal{D}}_R$ and $\overline{\mathcal{D}}_Z$ are also not realistic.

We then release the constraint of $\mathcal{D}_{ZR} = \mathcal{D}_{RZ} = 0$, allowing them to be non-zero but still constant. Figure B.3 shows the fitted results in radial and vertical directions. We find the diffusion profiles still do not match the advection ones, even with the contribution from both directions considered. Therefore, a constant diffusion tensor $\overline{\mathcal{D}}$ in the original gradient diffusion hypothesis is not applicable to our models.

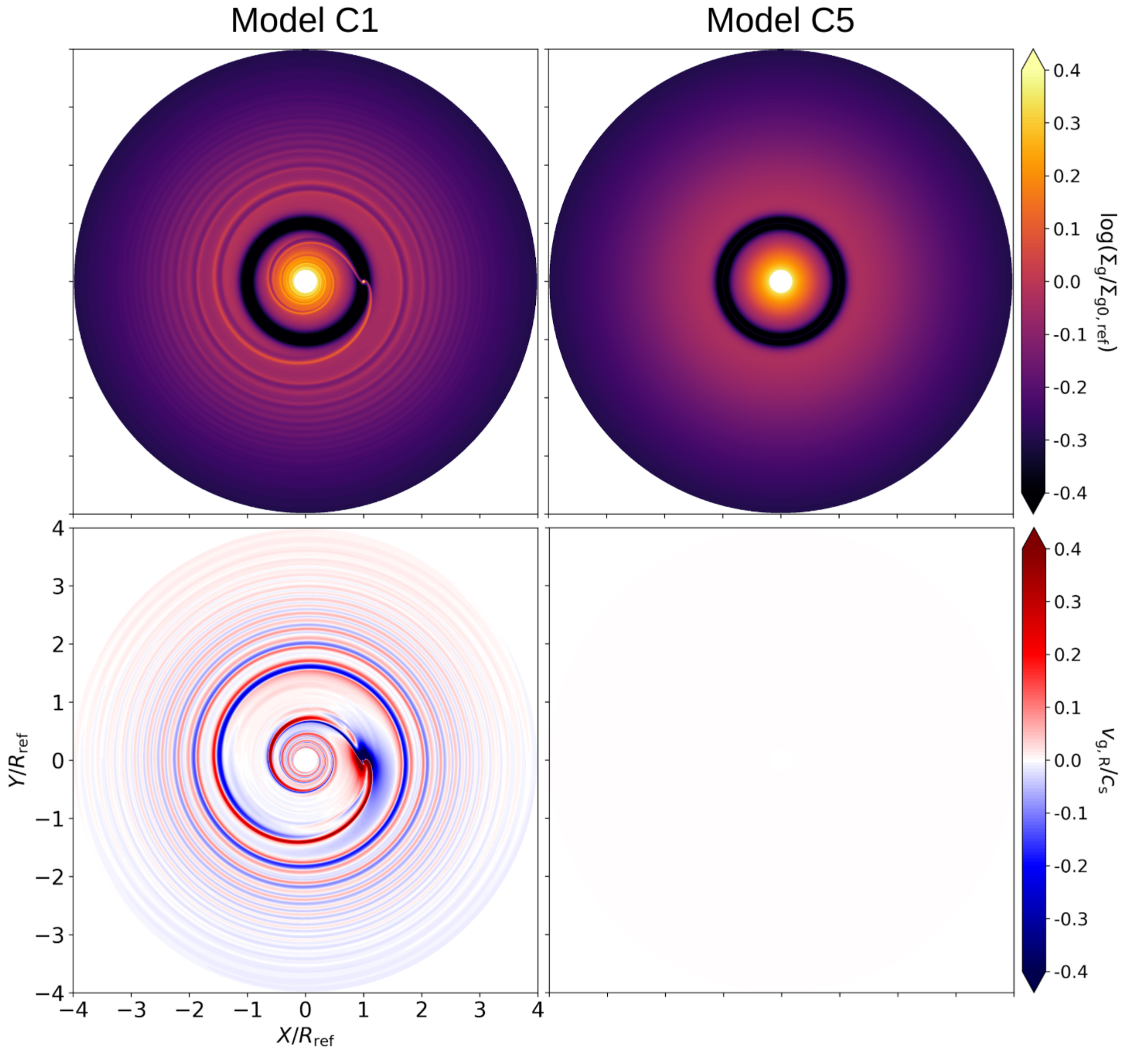

Figure B.1: Gas surface density and midplane gas radial velocity of Model C1 and C5. Panels are showing gas surface density on the top and midplane gas radial velocity at the bottom. Plots for Model C1 are shown on the left and those for Model C5 are on the right. Because gas evolution is stalled in type C models, all four panels are time-invariant. In Model C1, planet-related spirals in both gas density and velocity fields are preserved, whereas those in Model C5 are erased by azimuthal averaging. The bottom right panel is all white because the midplane gas in Model C5 has zero radial velocity.

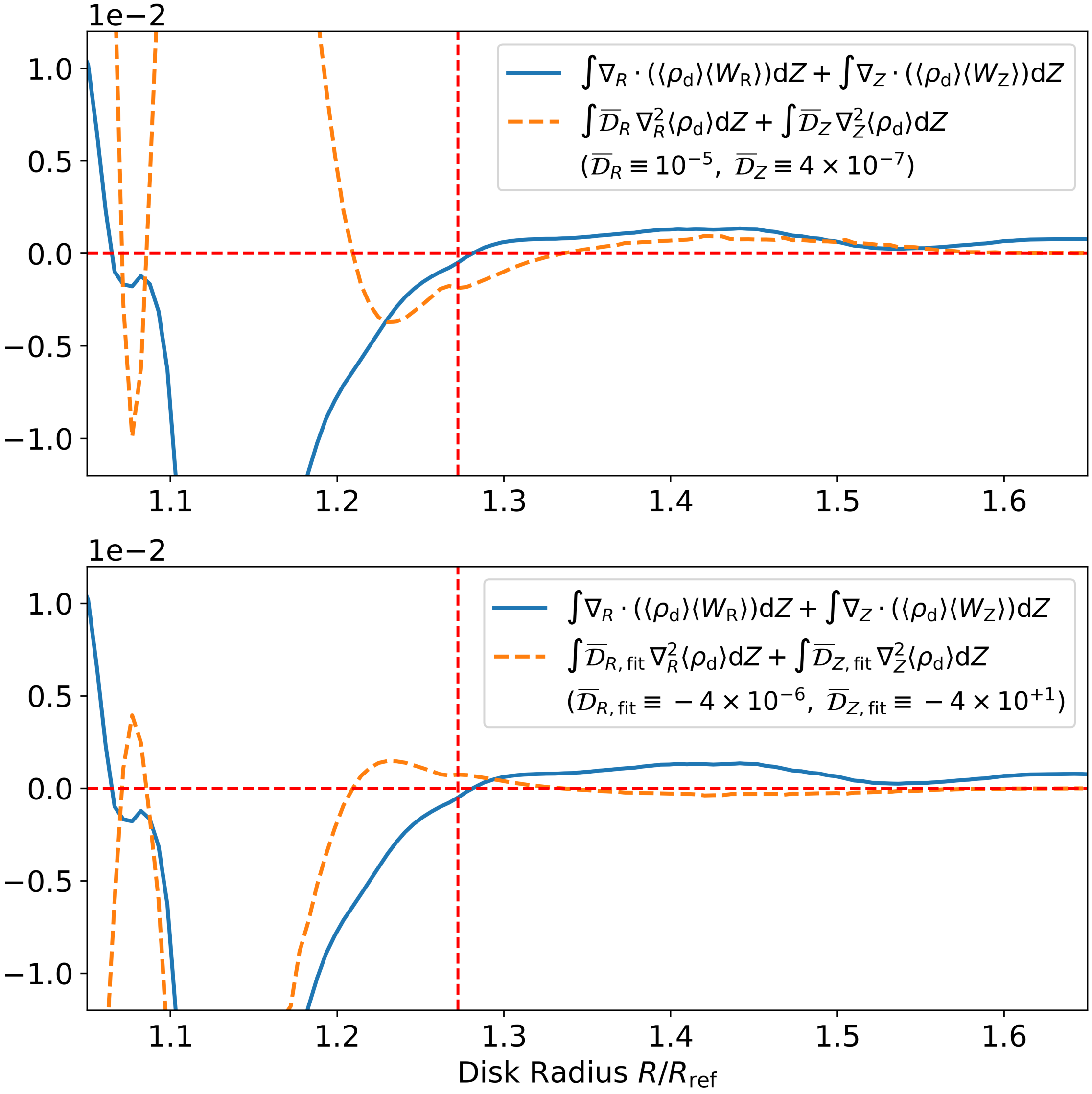

Figure B.2: Radial profile of the vertically integrated advection and diffusion terms from the old gradient diffusion hypothesis. All profiles are normalized to the dust surface density profile and are evaluated in the fiducial type A model at $t = 3000 P_\mathrm{K,ref}$. $\overline{\mathcal{D}}_R$ and $\overline{\mathcal{D}}_Z$ in the top panel are identical to the ones in Figure 3.3 (*a*–*b*). In the bottom panel, $\overline{\mathcal{D}}_R$ and $\overline{\mathcal{D}}_Z$ are fitted within the plotted range for the best match. The unit of $\overline{\mathcal{D}}_R$ and $\overline{\mathcal{D}}_Z$ is $R_\mathrm{ref}^2 \Omega_\mathrm{K,ref}$. The horizontal red dashed line denotes $y = 0$. The vertical red dashed line denotes the dust peak at $R = 1.27 R_\mathrm{ref}$.

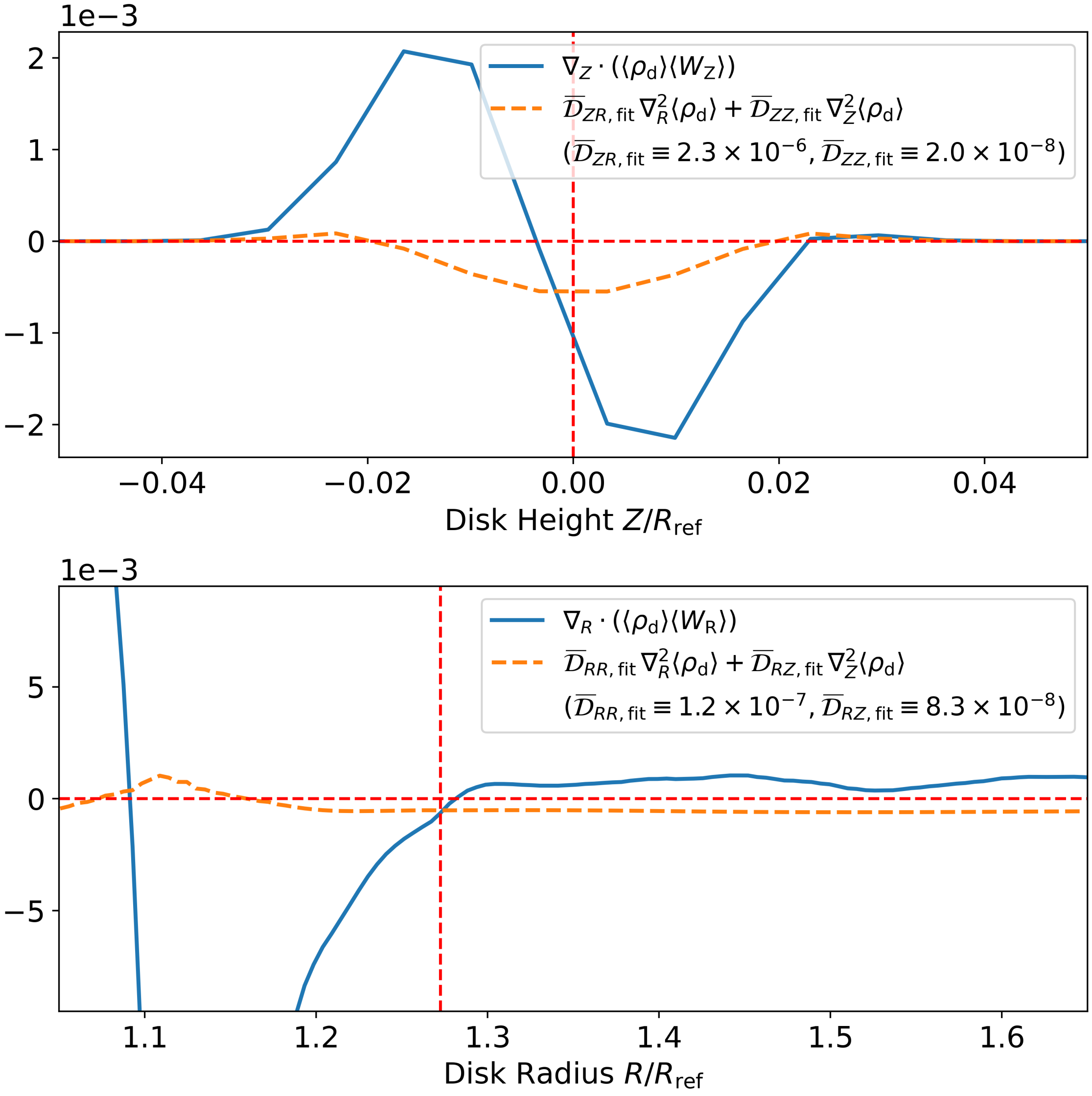

Figure B.3: Reproducing panels *a* and *b* in Figure 3.3 but allowing $\mathcal{D}_{ZR}$ and $\mathcal{D}_{RZ}$ to be nonzero. All four diffusion coefficients are fitted within the plotted range for the best match.

B.3 Steps From Equation 3.22 to Equation 3.23

Considering Equation 3.20, 3.15, and 3.21, and multiplying $\langle\rho_\mathrm{g}\rangle$ to both sides, Equation 3.22 writes

$$\begin{aligned}
0 &= \langle\rho_\mathrm{g}\rangle\frac{\partial\langle\epsilon_\rho\rangle}{\partial t} + \langle\rho_\mathrm{g}\rangle\langle\boldsymbol{V}\rangle\nabla\langle\epsilon_\rho\rangle && \text{(B.1)}\\
&= \frac{\partial\langle\rho_\mathrm{d}\rangle}{\partial t} - \langle\epsilon_\rho\rangle\frac{\partial\langle\rho_\mathrm{g}\rangle}{\partial t} + \langle\rho_\mathrm{g}\rangle\langle\boldsymbol{V}\rangle\nabla\langle\epsilon_\rho\rangle && \text{(B.2)}\\
&= -\nabla\cdot\Big(\langle\rho_\mathrm{d}\rangle\langle\boldsymbol{W}\rangle\Big) - \nabla\cdot\langle\Delta\rho_\mathrm{d}\Delta\boldsymbol{W}\rangle + \langle\epsilon_\rho\rangle\nabla\cdot\Big(\langle\rho_\mathrm{g}\rangle\langle\boldsymbol{V}\rangle\Big) && \text{(B.3)}\\
&\quad + \langle\epsilon_\rho\rangle\nabla\cdot\langle\Delta\rho_\mathrm{g}\Delta\boldsymbol{V}\rangle + \langle\rho_\mathrm{g}\rangle\langle\boldsymbol{V}\rangle\nabla\langle\epsilon_\rho\rangle\\
&= -\nabla\cdot\Big(\langle\rho_\mathrm{d}\rangle\langle\boldsymbol{W}\rangle\Big) - \nabla\cdot\langle\Delta\rho_\mathrm{d}\Delta\boldsymbol{W}\rangle + \nabla\cdot\Big(\langle\epsilon_\rho\rangle\langle\rho_\mathrm{g}\rangle\langle\boldsymbol{V}\rangle\Big) && \text{(B.4)}\\
&\quad + \langle\epsilon_\rho\rangle\nabla\cdot\langle\Delta\rho_\mathrm{g}\Delta\boldsymbol{V}\rangle\\
&= -\nabla\cdot\Big(\langle\rho_\mathrm{d}\rangle\langle\boldsymbol{W}-\boldsymbol{V}\rangle\Big) - \nabla\cdot\langle\Delta\rho_\mathrm{d}\Delta\boldsymbol{W}\rangle + \langle\epsilon_\rho\rangle\nabla\cdot\langle\Delta\rho_\mathrm{g}\Delta\boldsymbol{V}\rangle && \text{(B.5)}\\
&= -\nabla\cdot\Big(\langle\rho_\mathrm{d}\rangle\langle\boldsymbol{W}-\boldsymbol{V}\rangle\Big) + \nabla\cdot\Big(\mathcal{D}\langle\rho_\mathrm{g}\rangle\nabla\langle\epsilon_\rho\rangle\Big). && \text{(B.6)}
\end{aligned}$$

Bibliography

ALMA Partnership, C. L. Brogan, L. M. Pérez, T. R. Hunter, W. R. F. Dent, A. S. Hales, R. E. Hills, S. Corder, E. B. Fomalont, C. Vlahakis, Y. Asaki, D. Barkats, A. Hirota, J. A. Hodge, C. M. V. Impellizzeri, R. Kneissl, E. Liuzzo, R. Lucas, N. Marcelino, S. Matsushita, K. Nakanishi, N. Phillips, A. M. S. Richards, I. Toledo, R. Aladro, D. Broguiere, J. R. Cortes, P. C. Cortes, D. Espada, F. Galarza, D. Garcia Appadoo, L. Guzman Ramirez, E. M. Humphreys, T. Jung, S. Kameno, R. A. Laing, S. Leon, G. Marconi, A. Mignano, B. Nikolic, L.-A. Nyman, M. Radiszcz, A. Remijan, J. A. Rodón, T. Sawada, S. Takahashi, R. P. J. Tilanus, B. Vila Vilaro, L. C. Watson, T. Wiklind, E. Akiyama, E. Chapillon, I. de Gregorio Monsalvo, J. Di Francesco, F. Gueth, A. Kawamura, C.-F. Lee, Q. Nguyen Luong, J. Mangum, V. Pietu, P. Sanhueza, K. Saigo, S. Takakuwa, C. Ubach, T. van Kempen, A. Wootten, A. Castro Carrizo, H. Francke, J. Gallardo, J. Garcia, S. Gonzalez, T. Hill, T. Kaminski, Y. Kurono, H.-Y. Liu, C. Lopez, F. Morales, K. Plarre, G. Schieven, L. Testi, L. Videla, E. Villard, P. Andreani, J. E. Hibbard, and K. Tatematsu. The 2014 ALMA Long Baseline Campaign: First Results from High Angular Resolution Observations Toward the HL Tau Region. *The Astrophysical Journal*, 808 (1):L3, July 2015. ISSN 2041-8213. doi: 10.1088/2041-8205/808/1/L3. URL `https://iopscience.iop.org/article/10.1088/2041-8205/808/1/L3`.

Sean M. Andrews, Jane Huang, Laura M. Pérez, Andrea Isella, Cornelis P. Dullemond, Nicolás T. Kurtovic, Viviana V. Guzmán, John M. Carpenter, David J. Wilner, Shangjia Zhang, Zhaohuan Zhu, Tilman Birnstiel, Xue-Ning Bai, Myriam Benisty, A. Meredith Hughes, Karin I. Öberg, and Luca Ricci. The Disk Substructures at High Angular Resolution Project (DSHARP). I. Motivation, Sample, Calibration, and Overview. *The Astrophysical Journal*, 869(2):L41, December 2018. ISSN 2041-8213. doi: 10.3847/2041-8213/aaf741. URL `https://iopscience.iop.org/article/10.3847/2041-8213/aaf741`.

M. Benisty, C. Dominik, K. Follette, A. Garufi, C. Ginski, J. Hashimoto, M. Keppler, W. Kley, and J. Monnier. Optical and Near-infrared View of Planet-forming Disks and Protoplanets. *arXiv:2203.09991 [astro-ph]*, March 2022. URL `http://arxiv.org/abs/2203.09991`. arXiv: 2203.09991.

Myriam Benisty, Jaehan Bae, Stefano Facchini, Miriam Keppler, Richard Teague, Andrea Isella, Nicolas T. Kurtovic, Laura M. Pérez, Anibal Sierra, Sean M. Andrews, John Carpenter, Ian Czekala, Carsten Dominik, Thomas Henning, Francois Menard, Paola Pinilla, and Alice Zurlo. A Circumplanetary Disk around PDS70c. *The Astrophysical Journal Letters*, 916(1):L2, July 2021. ISSN 2041-8205, 2041-8213. doi: 10.3847/2041-8213/ac0f83. URL `https://iopscience.iop.org/article/10.3847/2041-8213/ac0f83`.

Pablo Benítez-Llambay and Frédéric S. Masset. FARGO3D: A New GPU-oriented MHD Code. *The Astrophysical Journal Supplement Series*, 223(1):11, March 2016. ISSN 1538-4365. doi: 10.3847/0067-0049/223/1/11. URL `https://iopscience.iop.org/article/10.3847/0067-0049/223/1/11`.

Pablo Benítez-Llambay, Leonardo Krapp, and Martin E. Pessah. Asymptotically Stable Numerical Method for Multispecies Momentum Transfer: Gas and Multifluid Dust Test Suite and Implementation in FARGO3D. *The Astrophysical Journal Supplement Series*, 241(2):25, April 2019. ISSN 1538-4365. doi: 10.3847/1538-4365/ab0a0e. URL `https://iopscience.iop.org/article/10.3847/1538-4365/ab0a0e`.

Jiaqing Bi, Min-Kai Lin, and Ruobing Dong. Puffed-up Edges of Planet-opened Gaps in Protoplanetary Disks. I. Hydrodynamic Simulations. *The Astrophysical Journal*, 912(2):107, May 2021. ISSN 0004-637X, 1538-4357. doi: 10.3847/1538-4357/abef6b. URL `https://iopscience.iop.org/article/10.3847/1538-4357/abef6b`.

T. Birnstiel, H. Klahr, and B. Ercolano. A simple model for the evolution of the dust population in protoplanetary disks. *Astronomy & Astrophysics*, 539:A148, March 2012. ISSN 0004-6361, 1432-0746. doi: 10.1051/0004-6361/201118136. URL `http://www.aanda.org/10.1051/0004-6361/201118136`.

Alice S Booth and John D Ilee. 13C17O Suggests Gravitational Instability in the HL Tau Disc. *Monthly Notices of the Royal Astronomical Society: Letters*, 493(1):

L108–L113, March 2020. ISSN 1745-3925, 1745-3933. doi: 10.1093/mnrasl/slaa014. URL `https://academic.oup.com/mnrasl/article/493/1/L108/5715469`.

Brendan P. Bowler. Imaging Extrasolar Giant Planets. *Publications of the Astronomical Society of the Pacific*, 128(968):102001, October 2016. ISSN 0004-6280, 1538-3873. doi: 10.1088/1538-3873/128/968/102001. URL `https://iopscience.iop.org/article/10.1088/1538-3873/128/968/102001`.

Eugene Chiang and Ruth Murray-Clay. Inside-out evacuation of transitional protoplanetary discs by the magneto-rotational instability. *Nature Physics*, 3(9): 604–608, September 2007. ISSN 1745-2473, 1745-2481. doi: 10.1038/nphys661. URL `http://www.nature.com/articles/nphys661`.

Lucas A Cieza, Camilo González-Ruilova, Antonio S Hales, Paola Pinilla, Dary Ruíz-Rodríguez, Alice Zurlo, Simón Casassus, Sebastián Pérez, Hector Cánovas, Carla Arce-Tord, Mario Flock, Nicolas Kurtovic, Sebastian Marino, Pedro H Nogueira, Laura Perez, Daniel J Price, David A Principe, and Jonathan P Williams. The Ophiuchus DIsc Survey Employing ALMA (ODISEA) – III. The evolution of substructures in massive discs at 3–5 au resolution. *Monthly Notices of the Royal Astronomical Society*, 501(2):2934–2953, January 2021. ISSN 0035-8711, 1365-2966. doi: 10.1093/mnras/staa3787. URL `https://academic.oup.com/mnras/article/501/2/2934/6030048`.

Thayne Currie, Kellen Lawson, Glenn Schneider, Wladimir Lyra, John Wisniewski, Carol Grady, Olivier Guyon, Motohide Tamura, Takayuki Kotani, Hajime Kawahara, Timothy Brandt, Taichi Uyama, Takayuki Muto, Ruobing Dong, Tomoyuki Kudo, Jun Hashimoto, Misato Fukagawa, Kevin Wagner, Julien Lozi, Jeffrey Chilcote, Taylor Tobin, Tyler Groff, Kimberly Ward-Duong, William Januszewski, Barnaby Norris, Peter Tuthill, Nienke van der Marel, Michael Sitko, Vincent Deo, Sebastien Vievard, Nemanja Jovanovic, Frantz Martinache, and Nour Skaf. Images of Embedded Jovian Planet Formation At A Wide Separation Around AB Aurigae. *Nature Astronomy*, 6:751, April 2022. ISSN 2397-3366. doi: 10.1038/s41550-022-01634-x. URL `https://www.nature.com/articles/s41550-022-01634-x`.

Jeffrey N. Cuzzi, Anthony R. Dobrovolskis, and Joelle M. Champney. Particle-Gas Dynamics in the Midplane of a Protoplanetary Nebula. *Icarus*, 106(1):102–134, November 1993. doi: 10.1006/icar.1993.1161. URL `https://ui.adsabs.harvard.edu/abs/1993Icar..106..102C`.

Steven J. Desch, Paul R. Estrada, Anusha Kalyaan, and Jeffrey N. Cuzzi. Formulas for Radial Transport in Protoplanetary Disks. *The Astrophysical Journal*, 840(2): 86, May 2017. ISSN 1538-4357. doi: 10.3847/1538-4357/aa6bfb. URL `https://iopscience.iop.org/article/10.3847/1538-4357/aa6bfb`.

C. Dominik and C. P. Dullemond. Accretion through the inner hole of transitional disks: what happens to the dust? *Astronomy & Astrophysics*, 531:A101, July 2011. ISSN 0004-6361, 1432-0746. doi: 10.1051/0004-6361/201116629. URL `http://www.aanda.org/10.1051/0004-6361/201116629`.

Joanna Drążkowska, Bertram Bitsch, Michiel Lambrechts, Gijs D. Mulders, Daniel Harsono, Allona Vazan, Beibei Liu, Chris W. Ormel, Katherine Kretke, and Alessandro Morbidelli. Planet Formation Theory in the Era of ALMA and Kepler: from Pebbles to Exoplanets. *arXiv:2203.09759 [astro-ph]*, March 2022. URL `http://arxiv.org/abs/2203.09759`. arXiv: 2203.09759.

Paul C. Duffell. A Simple Analytical Model for Gaps in Protoplanetary Disks. *The Astrophysical Journal*, 807(1):L11, June 2015. ISSN 2041-8213. doi: 10.1088/2041-8205/807/1/L11. URL `https://iopscience.iop.org/article/10.1088/2041-8205/807/1/L11`.

Paul C. Duffell. An Empirically Derived Formula for the Shape of Planet-induced Gaps in Protoplanetary Disks. *The Astrophysical Journal*, 889(1):16, January 2020. ISSN 1538-4357. doi: 10.3847/1538-4357/ab5b0f. URL `https://iopscience.iop.org/article/10.3847/1538-4357/ab5b0f`.

Cornelis P. Dullemond, Tilman Birnstiel, Jane Huang, Nicolás T. Kurtovic, Sean M. Andrews, Viviana V. Guzmán, Laura M. Pérez, Andrea Isella, Zhaohuan Zhu, Myriam Benisty, David J. Wilner, Xue-Ning Bai, John M. Carpenter, Shangjia Zhang, and Luca Ricci. The Disk Substructures at High Angular Resolution Project (DSHARP). VI. Dust Trapping in Thin-Ringed Protoplanetary Disks. *The Astrophysical Journal*, 869(2):L46, December 2018. ISSN 2041-8213. doi: 10.3847/2041-8213/aaf742. URL `https://iopscience.iop.org/article/10.3847/2041-8213/aaf742`.

Barbara Ercolano, Giovanni Picogna, Kristina Monsch, Jeremy J Drake, and Thomas Preibisch. The Dispersal of Protoplanetary Discs – II: Photoevaporation Models with Observationally Derived Irradiating Spectra. *Monthly Notices of the Royal Astronomical Society*, 508(2):1675–1685, October 2021. ISSN 0035-8711, 1365-2966. doi: 10.1093/mnras/stab2590. URL `https://academic.oup.com/mnras/article/508/2/1675/6373466`.

Kevin Flaherty, A. Meredith Hughes, Jacob B. Simon, Chunhua Qi, Xue-Ning Bai, Alyssa Bulatek, Sean M. Andrews, David J. Wilner, and Ágnes Kóspál. Measuring Turbulent Motion in Planet-forming Disks with ALMA: A Detection around DM Tau and Nondetections around MWC 480 and V4046 Sgr. *The Astrophysical Journal*, 895(2):109, June 2020. ISSN 1538-4357. doi: 10.3847/1538-4357/ab8cc5. URL `https://iopscience.iop.org/article/10.3847/1538-4357/ab8cc5`.

Logan Francis and Nienke van der Marel. Dust-depleted Inner Disks in a Large Sample of Transition Disks through Long-baseline ALMA Observations. *The Astrophysical Journal*, 892(2):111, April 2020. ISSN 1538-4357. doi: 10.3847/1538-4357/ab7b63. URL `https://iopscience.iop.org/article/10.3847/1538-4357/ab7b63`.

Jeffrey Fung and Pawel Artymowicz. Irradiation Instability at the Inner Edges of Accretion Disks. *The Astrophysical Journal*, 790(1):78, July 2014. ISSN 0004-637X, 1538-4357. doi: 10.1088/0004-637X/790/1/78. URL `https://iopscience.iop.org/article/10.1088/0004-637X/790/1/78`.

Jeffrey Fung and Eugene Chiang. Save the Planet, Feed the Star: How Super-Earths Survive Migration and Drive Disk Accretion. *The Astrophysical Journal*, 839(2):100, April 2017. ISSN 1538-4357. doi: 10.3847/1538-4357/aa6934. URL `https://iopscience.iop.org/article/10.3847/1538-4357/aa6934`.

Jeffrey Fung and Dhruv Muley. A Staggered Semi-analytic Method for Simulating Dust Grains Subject to Gas Drag. *The Astrophysical Journal Supplement Series*, 244(2):42, October 2019. ISSN 1538-4365. doi: 10.3847/1538-4365/ab45f3. URL `https://iopscience.iop.org/article/10.3847/1538-4365/ab45f3`.

E. Furlan, K. L. Luhman, C. Espaillat, P. D'Alessio, L. Adame, P. Manoj, K. H. Kim, Dan M. Watson, W. J. Forrest, M. K. McClure, N. Calvet, B. A. Sargent, J. D. Green, and W. J. Fischer. The Spitzer Infrared Spectrograph Survey of T Tauri Stars in Taurus. *The Astrophysical Journal Supplement Series*, 195(1):3, July 2011. ISSN 0067-0049, 1538-4365. doi: 10.1088/0067-0049/195/1/3. URL `https://iopscience.iop.org/article/10.1088/0067-0049/195/1/3`.

Anthony J L Garcia and Jean-François Gonzalez. Evolution of Porous Dust Grains in Protoplanetary Discs – I. Growing Grains. *Monthly Notices of the Royal Astronomical Society*, 493(2):1788–1800, April 2020. ISSN 0035-8711, 1365-2966. doi: 10.1093/mnras/staa382. URL `https://academic.oup.com/mnras/article/493/2/1788/5731863`.

A. Garufi, H. Avenhaus, S. Pérez, S. P. Quanz, R. G. van Holstein, G. H.-M. Bertrang, S. Casassus, L. Cieza, D. A. Principe, G. van der Plas, and A. Zurlo. Disks Around T Tauri Stars with SPHERE (DARTTS-S): II. Twenty-one New Polarimetric Images of Young Stellar Disks. *Astronomy & Astrophysics*, 633:A82, January 2020. ISSN 0004-6361, 1432-0746. doi: 10.1051/0004-6361/201936946. URL `https://www.aanda.org/10.1051/0004-6361/201936946`.

J. Goodman and R. R. Rafikov. Planetary Torques as the Viscosity of Protoplanetary Disks. *The Astrophysical Journal*, 552:793–802, May 2001. doi: 10.1086/320572. URL `https://ui.adsabs.harvard.edu/abs/2001ApJ...552..793G`.

G. Guidi, A. Isella, L. Testi, C. J. Chandler, H. B. Liu, H. M. Schmid, G. Rosotti, C. Meng, J. Jennings, J. P. Williams, J. M. Carpenter, I. de Gregorio-Monsalvo, H. Li, S. F. Liu, S. Ortolani, S. P. Quanz, L. Ricci, and M. Tazzari. Distribution of solids in the rings of the HD 163296 disk: a multiwavelength study. *Astronomy & Astrophysics*, 664:A137, August 2022. ISSN 0004-6361, 1432-0746. doi: 10.1051/0004-6361/202142303. URL `https://www.aanda.org/10.1051/0004-6361/202142303`.

J. Guzmán-Díaz, I. Mendigutía, B. Montesinos, R. D. Oudmaijer, M. Vioque, C. Rodrigo, E. Solano, G. Meeus, and P. Marcos-Arenal. Homogeneous study of Herbig Ae/Be stars from spectral energy distributions and Gaia EDR3. *Astronomy & Astrophysics*, 650:A182, June 2021. ISSN 0004-6361, 1432-0746. doi: 10.1051/0004-6361/202039519. URL `https://www.aanda.org/10.1051/0004-6361/202039519`.

Matías Gárate, Timmy N. Delage, Jochen Stadler, Paola Pinilla, Til Birnstiel, Sebastian Markus Stammler, Giovanni Picogna, Barbara Ercolano, Raphael Franz, and Christian Lenz. Large gaps and high accretion rates in photoevaporative transition disks with a dead zone. *Astronomy & Astrophysics*, 655:A18, November 2021. ISSN 0004-6361, 1432-0746. doi: 10.1051/0004-6361/202141444. URL https://www.aanda.org/10.1051/0004-6361/202141444.

S. Y. Haffert, A. J. Bohn, J. de Boer, I. A. G. Snellen, J. Brinchmann, J. H. Girard, C. U. Keller, and R. Bacon. Two Accreting Protoplanets Around the Young Star PDS 70. *Nature Astronomy*, 3:749–754, June 2019. doi: 10.1038/s41550-019-0780-5.

Iain Hammond, Valentin Christiaens, Daniel J Price, Claudia Toci, Christophe Pinte, Sandrine Juillard, and Himanshi Garg. Confirmation and Keplerian motion of the gap-carving protoplanet HD 169142 b. *Monthly Notices of the Royal Astronomical Society: Letters*, 522(1):L51–L55, March 2023. ISSN 1745-3925, 1745-3933. doi: 10.1093/mnrasl/slad027. URL https://academic.oup.com/mnrasl/article/522/1/L51/7070740.

Yukihiko Hasegawa, Takeru K. Suzuki, Hidekazu Tanaka, Hiroshi Kobayashi, and Koji Wada. Collisional Growth and Fragmentation of Dust Aggregates with Low Mass Ratios. I. Critical Collision Velocity for Water Ice. *The Astrophysical Journal*, 915(1):22, July 2021. ISSN 0004-637X, 1538-4357. doi: 10.3847/1538-4357/abf6cf. URL https://iopscience.iop.org/article/10.3847/1538-4357/abf6cf.

C. Hayashi. Structure of the Solar Nebula, Growth and Decay of Magnetic Fields and Effects of Magnetic and Turbulent Viscosities on the Nebula. *Progress of Theoretical Physics Supplement*, 70:35–53, January 1981. doi: 10.1143/PTPS.70.35. URL https://ui.adsabs.harvard.edu/abs/1981PThPS..70...35H.

R. W. Hockney and J. W. Eastwood. Computer Simulation Using Particles. *Computer Simulation Using Particles, New York: McGraw-Hill, 1981*, 1981. URL http://adsabs.harvard.edu/abs/1981csup.book.....H.

Jane Huang, Sean M. Andrews, L. Ilsedore Cleeves, Karin I. Öberg, David J. Wilner, Xuening Bai, Til Birnstiel, John Carpenter, A. Meredith Hughes, Andrea Isella, Laura M. Pérez, Luca Ricci, and Zhaohuan Zhu. CO and Dust Properties in the TW Hya Disk from High-resolution ALMA Observations. *The Astrophysical Journal*, 852(2):122, January 2018a. ISSN 1538-4357. doi: 10.3847/1538-4357/aaa1e7. URL https://iopscience.iop.org/article/10.3847/1538-4357/aaa1e7.

Jane Huang, Sean M. Andrews, Cornelis P. Dullemond, Andrea Isella, Laura M. Pérez, Viviana V. Guzmán, Karin I. Öberg, Zhaohuan Zhu, Shangjia Zhang, Xue-Ning Bai, Myriam Benisty, Tilman Birnstiel, John M. Carpenter, A. Meredith Hughes, Luca Ricci, Erik Weaver, and David J. Wilner. The Disk Substructures at High Angular Resolution Project (DSHARP). II. Characteristics of Annular Substructures. *The Astrophysical Journal*, 869(2):L42, December 2018b. ISSN 2041-8213. doi: 10.3847/2041-8213/aaf740. URL `https://iopscience.iop.org/article/10.3847/2041-8213/aaf740`.

Pinghui Huang, Hui Li, Andrea Isella, Ryan Miranda, Shengtai Li, and Jianghui Ji. Meso-Scale Instability Triggered by Dust Feedback in Dusty Rings: Origin and Observational Implications. *The Astrophysical Journal*, 893(2):89, April 2020. ISSN 1538-4357. doi: 10.3847/1538-4357/ab8199. URL `https://iopscience.iop.org/article/10.3847/1538-4357/ab8199`.

Emmanuel Jacquet, Steven Balbus, and Henrik Latter. On Linear Dust-gas Streaming Instabilities in Protoplanetary Discs: Linear Dust-gas Streaming Instabilities. *Monthly Notices of the Royal Astronomical Society*, 415(4):3591–3598, August 2011. ISSN 00358711. doi: 10.1111/j.1365-2966.2011.18971.x. URL `https://academic.oup.com/mnras/article-lookup/doi/10.1111/j.1365-2966.2011.18971.x`.

Haochang Jiang and Chris W Ormel. Survival of ALMA rings in the absence of pressure maxima. *Monthly Notices of the Royal Astronomical Society*, 505(1): 1162–1179, June 2021. ISSN 0035-8711, 1365-2966. doi: 10.1093/mnras/stab1278. URL `https://academic.oup.com/mnras/article/505/1/1162/6270896`.

Haochang Jiang and Chris W Ormel. Efficient planet formation by pebble accretion in ALMA rings. *Monthly Notices of the Royal Astronomical Society*, 518(3):3877–3900, December 2022. ISSN 0035-8711, 1365-2966. doi: 10.1093/mnras/stac3275. URL `https://academic.oup.com/mnras/article/518/3/3877/6835515`.

A. Johansen and A. Youdin. Protoplanetary Disk Turbulence Driven by the Streaming Instability: Nonlinear Saturation and Particle Concentration. *The Astrophysical Journal*, 662(1):627–641, June 2007. ISSN 0004-637X, 1538-4357. doi: 10.1086/516730. URL `https://iopscience.iop.org/article/10.1086/516730`.

A. Johansen, A. Youdin, and H. Klahr. Zonal Flows and Long-lived Axisymmetric Pressure Bumps in Magnetorotational Turbulence. *The Astrophysical Journal*, 697

(2):1269–1289, June 2009. ISSN 0004-637X, 1538-4357. doi: 10.1088/0004-637X/697/2/1269. URL https://iopscience.iop.org/article/10.1088/0004-637X/697/2/1269.

Anders Johansen, Jeffrey S. Oishi, Mordecai-Mark Mac Low, Hubert Klahr, Thomas Henning, and Andrew Youdin. Rapid planetesimal formation in turbulent circumstellar disks. *Nature*, 448(7157):1022–1025, August 2007. ISSN 0028-0836, 1476-4687. doi: 10.1038/nature06086. URL http://www.nature.com/articles/nature06086.

Kazuhiro D. Kanagawa, Takayuki Muto, Hidekazu Tanaka, Takayuki Tanigawa, Taku Takeuchi, Takashi Tsukagoshi, and Munetake Momose. Mass Constraint for a Planet in a Protoplanetary Disk from the Gap Width. *Publications of the Astronomical Society of Japan*, 68(3):43, June 2016. ISSN 0004-6264, 2053-051X. doi: 10.1093/pasj/psw037. URL https://academic.oup.com/pasj/article-lookup/doi/10.1093/pasj/psw037.

Kazuhiro D. Kanagawa, Takayuki Muto, Satoshi Okuzumi, Takayuki Tanigawa, Tetsuo Taki, and Yuhito Shibaike. Impacts of Dust Feedback on a Dust Ring Induced by a Planet in a Protoplanetary Disk. *The Astrophysical Journal*, 868 (1):48, November 2018. ISSN 1538-4357. doi: 10.3847/1538-4357/aae837. URL https://iopscience.iop.org/article/10.3847/1538-4357/aae837.

Akimasa Kataoka, Takayuki Muto, Munetake Momose, Takashi Tsukagoshi, and Cornelis P Dullemond. Grain Size Constraints on HL Tau with Polarization Signature. *The Astrophysical Journal*, 820(1):54, March 2016. ISSN 1538-4357. doi: 10.3847/0004-637X/820/1/54. URL https://iopscience.iop.org/article/10.3847/0004-637X/820/1/54.

M. Keppler, M. Benisty, A. Müller, Th. Henning, R. van Boekel, F. Cantalloube, C. Ginski, R. G. van Holstein, A.-L. Maire, A. Pohl, M. Samland, H. Avenhaus, J.-L. Baudino, A. Boccaletti, J. de Boer, M. Bonnefoy, G. Chauvin, S. Desidera, M. Langlois, C. Lazzoni, G.-D. Marleau, C. Mordasini, N. Pawellek, T. Stolker, A. Vigan, A. Zurlo, T. Birnstiel, W. Brandner, M. Feldt, M. Flock, J. Girard, R. Gratton, J. Hagelberg, A. Isella, M. Janson, A. Juhasz, J. Kemmer, Q. Kral, A.-M. Lagrange, R. Launhardt, A. Matter, F. Ménard, J. Milli, P. Mollière, J. Olofsson, L. Pérez, P. Pinilla, C. Pinte, S. P. Quanz, T. Schmidt, S. Udry,

Z. Wahhaj, J. P. Williams, E. Buenzli, M. Cudel, C. Dominik, R. Galicher, M. Kasper, J. Lannier, D. Mesa, D. Mouillet, S. Peretti, C. Perrot, G. Salter, E. Sissa, F. Wildi, L. Abe, J. Antichi, J.-C. Augereau, A. Baruffolo, P. Baudoz, A. Bazzon, J.-L. Beuzit, P. Blanchard, S. S. Brems, T. Buey, V. De Caprio, M. Carbillet, M. Carle, E. Cascone, A. Cheetham, R. Claudi, A. Costille, A. Delboulbé, K. Dohlen, D. Fantinel, P. Feautrier, T. Fusco, E. Giro, L. Gluck, C. Gry, N. Hubin, E. Hugot, M. Jaquet, D. Le Mignant, M. Llored, F. Madec, Y. Magnard, P. Martinez, D. Maurel, M. Meyer, O. Möller-Nilsson, T. Moulin, L. Mugnier, A. Origné, A. Pavlov, D. Perret, C. Petit, J. Pragt, P. Puget, P. Rabou, J. Ramos, F. Rigal, S. Rochat, R. Roelfsema, G. Rousset, A. Roux, B. Salasnich, J.-F. Sauvage, A. Sevin, C. Soenke, E. Stadler, M. Suarez, M. Turatto, and L. Weber. Discovery of a Planetary-mass Companion Within the Gap of the Transition Disk Around PDS 70. *Astronomy & Astrophysics*, 617:A44, September 2018. ISSN 0004-6361, 1432-0746. doi: 10.1051/0004-6361/201832957. URL https://www.aanda.org/10.1051/0004-6361/201832957.

Josef Koller, Hui Li, and Douglas N. C. Lin. Vortices in the Co-orbital Region of an Embedded Protoplanet. *The Astrophysical Journal*, 596(1):L91–L94, October 2003. ISSN 0004-637X, 1538-4357. doi: 10.1086/379032. URL https://iopscience.iop.org/article/10.1086/379032.

S. Krijt, C. W. Ormel, C. Dominik, and A. G. G. M. Tielens. A panoptic model for planetesimal formation and pebble delivery. *Astronomy & Astrophysics*, 586:A20, February 2016. ISSN 0004-6361, 1432-0746. doi: 10.1051/0004-6361/201527533. URL http://www.aanda.org/10.1051/0004-6361/201527533.

Mark R Krumholz, Michael J Ireland, and Kaitlin M Kratter. Dynamics of Small Grains in Transitional Discs. *Monthly Notices of the Royal Astronomical Society*, 498(2):3023–3042, September 2020. ISSN 0035-8711, 1365-2966. doi: 10.1093/mnras/staa2546. URL https://academic.oup.com/mnras/article/498/2/3023/5895357.

G. Laibe, J.-F. Gonzalez, L. Fouchet, and S. T. Maddison. SPH simulations of grain growth in protoplanetary disks. *Astronomy & Astrophysics*, 487(1):265–270, August 2008. ISSN 0004-6361, 1432-0746. doi: 10.1051/0004-6361:200809522. URL http://www.aanda.org/10.1051/0004-6361:200809522.

H. Li, S. H. Lubow, S. Li, and D. N. C. Lin. Type I Planet Migration in Nearly Laminar Disks. *The Astrophysical Journal*, 690(1):L52–L55, January 2009. ISSN 0004-637X, 1538-4357. doi: 10.1088/0004-637X/690/1/L52. URL `https://iopscience.iop.org/article/10.1088/0004-637X/690/1/L52`.

Hui Li, Shengtai Li, Josef Koller, Burton B. Wendroff, Richard Liska, Chris M. Orban, Edison P. T. Liang, and Douglas N. C. Lin. Potential Vorticity Evolution of a Protoplanetary Disk with an Embedded Protoplanet. *The Astrophysical Journal*, 624(2):1003–1009, May 2005. ISSN 0004-637X, 1538-4357. doi: 10.1086/429367. URL `https://iopscience.iop.org/article/10.1086/429367`.

D. N. C. Lin and J. C. B. Papaloizou. On the Tidal Interaction Between Protostellar Disks and Companions. In *Protostars and Planets III*. January 1993. URL `http://articles.adsabs.harvard.edu/pdf/1993prpl.conf..749L`.

Min-Kai Lin and John C. B. Papaloizou. Type III Migration in a Low-viscosity Disc. *Monthly Notices of the Royal Astronomical Society*, 405(3):1473–1490, April 2010. ISSN 00358711, 13652966. doi: 10.1111/j.1365-2966.2010.16560.x. URL `https://academic.oup.com/mnras/article-lookup/doi/10.1111/j.1365-2966.2010.16560.x`.

Feng Long, Paola Pinilla, Gregory J. Herczeg, Daniel Harsono, Giovanni Dipierro, Ilaria Pascucci, Nathan Hendler, Marco Tazzari, Enrico Ragusa, Colette Salyk, Suzan Edwards, Giuseppe Lodato, Gerrit van de Plas, Doug Johnstone, Yao Liu, Yann Boehler, Sylvie Cabrit, Carlo F. Manara, Francois Menard, Gijs D. Mulders, Brunella Nisini, William J. Fischer, Elisabetta Rigliaco, Andrea Banzatti, Henning Avenhaus, and Michael Gully-Santiago. Gaps and Rings in an ALMA Survey of Disks in the Taurus Star-forming Region. *The Astrophysical Journal*, 869(1):17, December 2018. ISSN 1538-4357. doi: 10.3847/1538-4357/aae8e1. URL `https://iopscience.iop.org/article/10.3847/1538-4357/aae8e1`.

Francesco Lovascio and Sijme-Jan Paardekooper. Dynamics of Dusty Vortices – I. Extensions and Limitations of the Terminal Velocity Approximation. *Monthly Notices of the Royal Astronomical Society*, 488(4):5290–5299, October 2019. ISSN 0035-8711, 1365-2966. doi: 10.1093/mnras/stz2035. URL `https://academic.oup.com/mnras/article/488/4/5290/5541075`.

J. S. Mathis, W. Rumpl, and K. H. Nordsieck. The size distribution of interstellar grains. *The Astrophysical Journal*, 217:425, October 1977. ISSN 0004-637X, 1538-4357. doi: 10.1086/155591. URL http://adsabs.harvard.edu/doi/10.1086/155591.

Michel Mayor and Didier Queloz. A Jupiter-mass companion to a solar-type star. *Nature*, 378:355–359, November 1995. ISSN 0028-0836. doi: 10.1038/378355a0. URL https://ui.adsabs.harvard.edu/abs/1995Natur.378..355M. ADS Bibcode: 1995Natur.378..355M.

James Muzerolle, Lori E. Allen, S. Thomas Megeath, Jesús Hernández, and Robert A. Gutermuth. A Spitzer Census of Transitional Protoplanetary Disks with au-Scale Inner Holes. *The Astrophysical Journal*, 708(2):1107–1118, January 2010. ISSN 0004-637X, 1538-4357. doi: 10.1088/0004-637X/708/2/1107. URL https://iopscience.iop.org/article/10.1088/0004-637X/708/2/1107.

Richard P. Nelson, Oliver Gressel, and Orkan M. Umurhan. Linear and Non-linear Evolution of the Vertical Shear Instability in Accretion Discs. *Monthly Notices of the Royal Astronomical Society*, 435(3):2610–2632, November 2013. ISSN 1365-2966, 0035-8711. doi: 10.1093/mnras/stt1475. URL http://academic.oup.com/mnras/article/435/3/2610/1031890/Linear-and-nonlinear-evolution-of-the-vertical.

Brodie J Norfolk, Sarah T Maddison, Christophe Pinte, Nienke van der Marel, Richard A Booth, Logan Francis, Jean-François Gonzalez, François Ménard, Chris M Wright, Gerrit van der Plas, and Himanshi Garg. Dust Traps and the Formation of Cavities in Transition Discs: A Millimetre to Sub-Millimetre Comparison Survey. *Monthly Notices of the Royal Astronomical Society*, 502(4):5779–5796, March 2021. ISSN 0035-8711, 1365-2966. doi: 10.1093/mnras/stab313. URL https://academic.oup.com/mnras/article/502/4/5779/6131844.

Satoshi Okuzumi, Hidekazu Tanaka, Hiroshi Kobayashi, and Koji Wada. Rapid Coagulation of Porous Dust Aggregates Outside the Snow Line: A Pathway to Successful Icy Planetesimal Formation. *The Astrophysical Journal*, 752(2):106, June 2012. ISSN 0004-637X, 1538-4357. doi: 10.1088/0004-637X/752/2/106. URL https://iopscience.iop.org/article/10.1088/0004-637X/752/2/106.

Satoshi Okuzumi, Munetake Momose, Sin-iti Sirono, Hiroshi Kobayashi, and Hidekazu Tanaka. Sintering-Induced Dust Ring Formation in Protoplanetary Disks: Application to the HL Tau Disk. *The Astrophysical Journal*, 821(2): 82, April 2016. ISSN 1538-4357. doi: 10.3847/0004-637X/821/2/82. URL `https://iopscience.iop.org/article/10.3847/0004-637X/821/2/82`.

Isamu K. Onishi and Minoru Sekiya. Planetesimal formation by an axisymmetric radial bump of the column density of the gas in a protoplanetary disk. *Earth, Planets and Space*, 69(1):50, December 2017. ISSN 1880-5981. doi: 10.1186/s40623-017-0637-z. URL `https://earth-planets-space.springeropen.com/articles/10.1186/s40623-017-0637-z`.

James E Owen and Juna A Kollmeier. Radiation Pressure Clear-out of Dusty Photoevaporating Discs. *Monthly Notices of the Royal Astronomical Society*, 487(3): 3702–3714, August 2019. ISSN 0035-8711, 1365-2966. doi: 10.1093/mnras/stz1591. URL `https://academic.oup.com/mnras/article/487/3/3702/5514005`.

S.-J. Paardekooper and G. Mellema. Planets Opening Dust Gaps in Gas Disks. *Astronomy & Astrophysics*, 425(1):L9–L12, October 2004. ISSN 0004-6361, 1432-0746. doi: 10.1051/0004-6361:200400053. URL `http://www.aanda.org/10.1051/0004-6361:200400053`.

Sijme-Jan Paardekooper, Ruobing Dong, Paul Duffell, Jeffrey Fung, Frederic S. Masset, Gordon Ogilvie, and Hidekazu Tanaka. Planet-Disk Interactions and Orbital Evolution. *arXiv:2203.09595 [astro-ph]*, March 2022. URL `http://arxiv.org/abs/2203.09595`. arXiv: 2203.09595.

Giovanni Picogna, Barbara Ercolano, James E Owen, and Michael L Weber. The Dispersal of Protoplanetary Discs – I. a New Generation of X-Ray Photoevaporation Models. *Monthly Notices of the Royal Astronomical Society*, 487(1): 691–701, July 2019. ISSN 0035-8711, 1365-2966. doi: 10.1093/mnras/stz1166. URL `https://academic.oup.com/mnras/article/487/1/691/5482089`.

Jaime E. Pineda, Doris Arzoumanian, Philippe André, Rachel K. Friesen, Annie Zavagno, Seamus D. Clarke, Tsuyoshi Inoue, Che-Yu Chen, Yueh-Ning Lee, Juan D. Soler, and Michael Kuffmeier. From Bubbles and Filaments to Cores and Disks: Gas Gathering and Growth of Structure Leading to the Formation of Stellar Systems, May 2022. URL http://arxiv.org/abs/2205.03935. arXiv:2205.03935 [astro-ph].

B. Portilla-Revelo, I. Kamp, Ch. Rab, E. F. van Dishoeck, M. Keppler, M. Min, and G. A. Muro-Arena. Self-consistent modelling of the dust component in protoplanetary and circumplanetary disks: the case of PDS 70. *Astronomy & Astrophysics*, 658:A89, February 2022. ISSN 0004-6361, 1432-0746. doi: 10.1051/0004-6361/202141764. URL https://www.aanda.org/10.1051/0004-6361/202141764.

Daniel J. Price and Guillaume Laibe. A Fast and Explicit Algorithm for Simulating the Dynamics of Small Dust Grains with Smoothed Particle Hydrodynamics. *Monthly Notices of the Royal Astronomical Society*, 451(1): 813–826, July 2015. ISSN 1365-2966, 0035-8711. doi: 10.1093/mnras/stv996. URL http://academic.oup.com/mnras/article/451/1/813/1380873/A-fast-and-explicit-algorithm-for-simulating-the.

Djoeke Schoonenberg, Chris W. Ormel, and Sebastiaan Krijt. A Lagrangian model for dust evolution in protoplanetary disks: formation of wet and dry planetesimals at different stellar masses. *Astronomy & Astrophysics*, 620:A134, December 2018. ISSN 0004-6361, 1432-0746. doi: 10.1051/0004-6361/201834047. URL https://www.aanda.org/10.1051/0004-6361/201834047.

N. I. Shakura and R. A. Sunyaev. Reprint of 1973A&A....24..337S. Black Holes in Binary Systems. Observational Appearance. *Astronomy & Astrophysics*, 500:33–51, June 1973. URL https://ui.adsabs.harvard.edu/abs/1973A&A....24..337S.

Jacob B. Simon, Philip J. Armitage, Rixin Li, and Andrew N. Youdin. The Mass and Size Distribution of Planetesimals Formed by the Streaming Instability. I. the Role of Self-Gravity. *The Astrophysical Journal*, 822(1):55, May 2016. ISSN 1538-4357. doi: 10.3847/0004-637X/822/1/55. URL https://iopscience.iop.org/article/10.3847/0004-637X/822/1/55.

Taku Takeuchi and Pawel Artymowicz. Dust Migration and Morphology in Optically Thin Circumstellar Gas Disks. *The Astrophysical Journal*, 557(2):990–1006, August 2001. ISSN 0004-637X, 1538-4357. doi: 10.1086/322252. URL https://iopscience.iop.org/article/10.1086/322252.

Taku Takeuchi and D. N. C. Lin. Radial Flow of Dust Particles in Accretion Disks. *The Astrophysical Journal*, 581(2):1344–1355, December 2002. ISSN 0004-637X, 1538-4357. doi: 10.1086/344437. URL https://iopscience.iop.org/article/10.1086/344437.

Taku Takeuchi and D. N. C. Lin. Surface Outflow in Optically Thick Dust Disks by Radiation Pressure. *The Astrophysical Journal*, 593(1):524–533, August 2003. ISSN 0004-637X, 1538-4357. doi: 10.1086/376496. URL https://iopscience.iop.org/article/10.1086/376496.

Tetsuo Taki, Masaki Fujimoto, and Shigeru Ida. Dust and gas density evolution at a radial pressure bump in protoplanetary disks. *Astronomy & Astrophysics*, 591: A86, July 2016. ISSN 0004-6361, 1432-0746. doi: 10.1051/0004-6361/201527732. URL http://www.aanda.org/10.1051/0004-6361/201527732.

Ya-Wen Tang, Stephane Guilloteau, Anne Dutrey, Takayuki Muto, Bo-Ting Shen, Pin-Gao Gu, Shu-ichiro Inutsuka, Munetake Momose, Vincent Pietu, Misato Fukagawa, Edwige Chapillon, Paul T. P. Ho, Emmanuel di Folco, Stuartt Corder, Nagayoshi Ohashi, and Jun Hashimoto. Planet Formation in AB Aurigae: Imaging of the Inner Gaseous Spirals Observed inside the Dust Cavity. *The Astrophysical Journal*, 840(1):32, May 2017. ISSN 1538-4357. doi: 10.3847/1538-4357/aa6af7. URL https://iopscience.iop.org/article/10.3847/1538-4357/aa6af7.

Ryosuke T. Tominaga, Sanemichi Z. Takahashi, and Shu-ichiro Inutsuka. Revised Description of Dust Diffusion and a New Instability Creating Multiple Rings in Protoplanetary Disks. *The Astrophysical Journal*, 881(1):53, August 2019. ISSN 1538-4357. doi: 10.3847/1538-4357/ab25ea. URL https://iopscience.iop.org/article/10.3847/1538-4357/ab25ea.

Ryosuke T. Tominaga, Shu-ichiro Inutsuka, and Hiroshi Kobayashi. Coagulation Instability in Protoplanetary Disks: A Novel Mechanism Connecting Collisional Growth and Hydrodynamical Clumping of Dust Particles. *The Astrophysical Journal*, 923(1):34, December 2021. ISSN 0004-637X, 1538-4357. doi: 10.3847/1538-4357/ac173a. URL https://iopscience.iop.org/article/10.3847/1538-4357/ac173a.

Nienke van der Marel. Transition disks: the observational revolution from SEDs to imaging, October 2022. URL http://arxiv.org/abs/2210.05539. arXiv:2210.05539 [astro-ph].

Nienke van der Marel, Jonathan P. Williams, M. Ansdell, Carlo F. Manara, Anna Miotello, Marco Tazzari, Leonardo Testi, Michiel Hogerheijde, Simon Bruderer, Sierk E. van Terwisga, and Ewine F. van Dishoeck. New Insights into the Nature of Transition Disks from a Complete Disk Survey of the Lupus Star-forming Region. *The Astrophysical Journal*, 854(2):177, February 2018. ISSN 1538-4357. doi: 10.3847/1538-4357/aaaa6b. URL `https://iopscience.iop.org/article/10.3847/1538-4357/aaaa6b`.

Nienke van der Marel, Ruobing Dong, James di Francesco, Jonathan P. Williams, and John Tobin. Protoplanetary Disk Rings and Gaps across Ages and Luminosities. *The Astrophysical Journal*, 872(1):112, February 2019. ISSN 1538-4357. doi: 10.3847/1538-4357/aafd31. URL `https://iopscience.iop.org/article/10.3847/1538-4357/aafd31`.

Philipp Weber, Sebastián Pérez, Pablo Benítez-Llambay, Oliver Gressel, Simon Casassus, and Leonardo Krapp. Predicting the Observational Signature of Migrating Neptune-sized Planets in Low-viscosity Disks. *The Astrophysical Journal*, 884 (2):178, October 2019. ISSN 1538-4357. doi: 10.3847/1538-4357/ab412f. URL `https://iopscience.iop.org/article/10.3847/1538-4357/ab412f`.

S. J. Weidenschilling. Aerodynamics of Solid Bodies in the Solar Nebula. *Monthly Notices of the Royal Astronomical Society*, 180(2):57–70, September 1977a. ISSN 0035-8711, 1365-2966. doi: 10.1093/mnras/180.2.57. URL `https://academic.oup.com/mnras/article-lookup/doi/10.1093/mnras/180.2.57`.

S. J. Weidenschilling. The Distribution of Mass in the Planetary System and Solar Nebula. *Astrophysics and Space Science*, 51:153–158, 1977b. doi: 10.1007/BF00642464. URL `http://articles.adsabs.harvard.edu/pdf/1977Ap%26SS..51..153W`.

A. Youdin and A. Johansen. Protoplanetary Disk Turbulence Driven by the Streaming Instability: Linear Evolution and Numerical Methods. *The Astrophysical Journal*, 662(1):613–626, June 2007. ISSN 0004-637X, 1538-4357. doi: 10.1086/516729. URL `https://iopscience.iop.org/article/10.1086/516729`.

Andrew N. Youdin. On the Formation of Planetesimals Via Secular Gravitational Instabilities with Turbulent Stirring. *The Astrophysical Journal*, 731(2):99, April

2011. ISSN 0004-637X, 1538-4357. doi: 10.1088/0004-637X/731/2/99. URL https://iopscience.iop.org/article/10.1088/0004-637X/731/2/99.

Andrew N. Youdin and Jeremy Goodman. Streaming Instabilities in Protoplanetary Disks. *The Astrophysical Journal*, 620(1):459–469, February 2005. ISSN 0004-637X, 1538-4357. doi: 10.1086/426895. URL https://iopscience.iop.org/article/10.1086/426895.

Andrew N. Youdin and Yoram Lithwick. Particle Stirring in Turbulent Gas Disks: Including Orbital Oscillations. *Icarus*, 192(2):588–604, December 2007. ISSN 00191035. doi: 10.1016/j.icarus.2007.07.012. URL https://linkinghub.elsevier.com/retrieve/pii/S0019103507003181.

Ke Zhang, Geoffrey A. Blake, and Edwin A. Bergin. Evidence of Fast Pebble Growth Near Condensation Fronts in the HL Tau Protoplanetary Disk. *The Astrophysical Journal*, 806(1):L7, June 2015. ISSN 2041-8213. doi: 10.1088/2041-8205/806/1/L7. URL https://iopscience.iop.org/article/10.1088/2041-8205/806/1/L7.

Shangjia Zhang, Zhaohuan Zhu, Jane Huang, Viviana V. Guzmán, Sean M. Andrews, Tilman Birnstiel, Cornelis P. Dullemond, John M. Carpenter, Andrea Isella, Laura M. Pérez, Myriam Benisty, David J. Wilner, Clément Baruteau, Xue-Ning Bai, and Luca Ricci. The Disk Substructures at High Angular Resolution Project (DSHARP). VII. The Planet–Disk Interactions Interpretation. *The Astrophysical Journal*, 869(2):L47, December 2018. ISSN 2041-8213. doi: 10.3847/2041-8213/aaf744. URL https://iopscience.iop.org/article/10.3847/2041-8213/aaf744.